



BEAD LOCALIZATION AND GEOMETRY MONITORING USING PASSIVE
VISION FOR WIRE ARC ADDITIVE MANUFACTURING SYSTEM

Marcus Vinícius de Oliveira Couto

Dissertação de Mestrado apresentada ao Programa de Pós-graduação em Engenharia Elétrica, COPPE, da Universidade Federal do Rio de Janeiro, como parte dos requisitos necessários à obtenção do título de Mestre em Engenharia Elétrica.

Orientadores: Ramon Romankevicius Costa
Antonio Candea Leite

Rio de Janeiro
Maio de 2022

BEAD LOCALIZATION AND GEOMETRY MONITORING USING PASSIVE
VISION FOR WIRE ARC ADDITIVE MANUFACTURING SYSTEM

Marcus Vinícius de Oliveira Couto

DISSERTAÇÃO SUBMETIDA AO CORPO DOCENTE DO INSTITUTO
ALBERTO LUIZ COIMBRA DE PÓS-GRADUAÇÃO E PESQUISA DE
ENGENHARIA DA UNIVERSIDADE FEDERAL DO RIO DE JANEIRO COMO
PARTE DOS REQUISITOS NECESSÁRIOS PARA A OBTENÇÃO DO GRAU
DE MESTRE EM CIÊNCIAS EM ENGENHARIA ELÉTRICA.

Orientadores: Ramon Romankevicius Costa
Antonio Candea Leite

Aprovada por: Prof. Ramon Romankevicius Costa
Prof. Antonio Candea Leite
Prof. Fernando Cesar Lizarralde
Prof. João da Cruz Payão Filho
Prof. Guilherme Caribé de Carvalho

RIO DE JANEIRO, RJ – BRASIL
MAIO DE 2022

Couto, Marcus Vinícius de Oliveira

Bead Localization and Geometry Monitoring Using Passive Vision For Wire Arc Additive Manufacturing System/Marcus Vinícius de Oliveira Couto. – Rio de Janeiro: UFRJ/COPPE, 2022.

XX, 127 p.: il.; 29, 7cm.

Orientadores: Ramon Romankevicius Costa

Antonio Candea Leite

Dissertação (mestrado) – UFRJ/COPPE/Programa de Engenharia Elétrica, 2022.

Referências Bibliográficas: p. 120 – 127.

1. Wire and arc additive manufacturing. 2. Bead width monitoring. 3. Bead mapping. 4. Computer Vision in WAAM. 5. Passive vision. I. Costa, Ramon Romankevicius *et al.* II. Universidade Federal do Rio de Janeiro, COPPE, Programa de Engenharia Elétrica. III. Título.

*Dedico este trabalho a minha
família, em especial a minha
mãe e meu pai que sempre me
ajudaram não importa a
situação. Amo vocês.*

Agradecimentos

Primeiramente gostaria de agradecer ao meu Deus que sempre cuida de mim de maneira silenciosa e plena. Em seguida gostaria de agradecer a minha família por todo o suporte e apoio nos momentos difíceis que pensei em desistir, em especial a minha mãe, pai, irmã e esposa, que sempre estão presentes nos dias difíceis. Também a todos os amigos feitos durante essa caminhada do mestrado que serão levados para o resto da vida. Obrigado também aos orientadores pelo suporte, dedicação e paciência, e aos professores que tanto me ensinaram durante esse mestrado.

Resumo da Dissertação apresentada à COPPE/UFRJ como parte dos requisitos necessários para a obtenção do grau de Mestre em Ciências (M.Sc.)

LOCALIZAÇÃO DO CORDÃO E MONITORAMENTO DA GEOMETRIA
USANDO VISÃO PASSIVA PARA UM SISTEMA DE MANUFATURA
ADITIVA POR ARCO E ARAME

Marcus Vinícius de Oliveira Couto

Maio/2022

Orientadores: Ramon Romankevicius Costa

Antonio Candea Leite

Programa: Engenharia Elétrica

Apresenta-se nesta dissertação de mestrado o monitoramento das características geométricas (largura e linha central) de cordões depositados durante a impressão 3D com o uso de câmeras passivas monoculares para manufatura aditiva por arame e arco elétrico (WAAM).

O desenvolvimento e integração de sistemas de manufatura aditiva (MA), como WAAM, é um tema de crescente interesse na indústria devido à sua vasta capacidade de produzir peças com geometria complexa com prazos curtos. No geral, a maioria do sistema funciona no formato de reprodução (offline), por exemplo, com seus parâmetros configurados offline, antes de iniciar a impressão da peça.

Para permitir a estimação das características desejadas são utilizados, segmentação com limite adaptativo, algoritmo de Canny para detecção de bordas, transformada de Hough para identificação de linhas, e filtragem para atenuar o ruído do processo. Uma proposta de estimação da posição do cordão também é feita através da utilização do filtro Kalman estendido (EKF) para atenuar a incerteza da medição da posição do cordão depositado.

Os experimentos foram realizadas em cenários de cordão único e múltiplo, sendo essas medições relevantes para WAAM pois ajudam a garantir a qualidade de cada camada e conseqüentemente a qualidade da peça produzida. A solução proposta é implementada experimentalmente em um sistema robótico composto por uma tocha de soldagem, um braço robótico, uma fonte de alimentação, um alimentador de arame e uma câmera monocular passiva.

Abstract of Dissertation presented to COPPE/UFRJ as a partial fulfillment of the requirements for the degree of Master of Science (M.Sc.)

BEAD LOCALIZATION AND GEOMETRY MONITORING USING PASSIVE VISION FOR WIRE ARC ADDITIVE MANUFACTURING SYSTEM

Marcus Vinícius de Oliveira Couto

May/2022

Advisors: Ramon Romankevicius Costa
Antonio Candea Leite

Department: Electrical Engineering

This dissertation addresses the online estimation of the geometry characteristics (width and centerline) of deposited beads while 3D printing with the usage of passive monocular cameras for wire and arc additive manufacturing .

The development and integration of additive manufacturing system, such as WAAM, is a topic of growing interest in the industry due to its vast capability to produce part with complex geometry with reduced lead times. Overall most system works at playback format, e.g. with its parameters being configured offline prior to start the printing.

To enable the estimation of the desired characteristics an adaptive threshold is used for segmentation, a Canny algorithm for edge detection, a Hough-line transform for line identification, and a filtering step to attenuate process noise. A proposal to estimate the bead placement is also performed with the usage of an extended Kalman filter , which uses the unicycle dynamic to predict the deposition trajectory in a system using plasma deposition (PAW).

The experiments were performed in both single and multi-bead scenarios, which are relevant to WAAM because it helps ensuring the quality of each layer and consequently the quality of the part produced. The proposed vision based solution is experimentally implemented in a WAAM robotic system composed of a welding torch, a robotic arm, a power source, a wire feeder, and a passive monocular camera.

Contents

List of Figures	xi
List of Tables	xvii
List of Symbols	xviii
List of Abbreviations	xix
1 Introduction	1
1.1 Motivation	2
1.2 Objective	3
1.3 Methodology	3
2 Additive Manufacturing System	6
2.1 Wire arc additive manufacturing	8
2.1.1 Steps used during WAAM	11
2.2 Path planning	12
2.3 WAAM-fabricated components common defects	14
2.3.1 Residual stress	15
2.3.2 Porosity	15
2.3.3 Delamination	16
2.3.4 Quality assurance	16
2.4 Direct and indirect deposition parameters	17
2.4.1 Torch travel speed	18
2.4.2 Travel speed influence on metal deposition	18
2.4.3 Travel speed reference	19
2.5 Vision-based sensing	20
2.5.1 Vision-based sensor	21
2.5.2 Active and passive vision sensors application	22
2.5.3 Noises present in the vision system during the deposition	22

3	Bead Geometry and Layer Design	24
3.1	Single-bead model	25
3.2	Multi-bead model	29
3.2.1	Surface layer quality	30
3.2.2	Overlapping model	31
3.3	Wire feeding impact on layer quality	32
4	Robotic, Controls and Computer Vision	38
4.1	Robot manipulator kinematics	38
4.1.1	Rotation matrix	39
4.1.2	Direct kinematic	39
4.1.3	Inverse kinematic	40
4.2	Computer vision	41
4.2.1	Camera model	42
4.2.2	Spatial filtering for vision sensors	45
4.2.3	Correlation and convolution	46
4.2.4	Smoothing linear filters	47
4.2.5	Sharpening spatial filters	50
4.2.6	Image Segmentation	52
4.2.7	Edge Detection	53
4.2.8	Line Identification	56
4.3	Gaussian Filters	58
4.3.1	Kalman Filter	59
4.3.2	Extended Kalman Filter	61
5	Bead Geometry Estimation and Localization Algorithms	63
5.1	Bead geometry measuring algorithm	64
5.1.1	Multi-Bead width measuring	67
5.1.2	Bead placement estimation during the deposition	67
5.1.3	Measurement filtering	69
5.1.4	Centerline estimation for WAAM with independent wire feeding system	71
6	Experiment and Simulation Setup	77
6.1	First experiment setup	77
6.2	Second experiment setup	80
6.2.1	Bead mapping	82
6.2.2	Bead samples	82
6.3	Third experiment setup	84
6.4	Simulation setup	84

7	Results and Discussion	89
7.1	First experiment	89
7.1.1	Width measurement of single-bead deposition	89
7.2	Second experiment	92
7.2.1	Segmentation analysis	93
7.2.2	Single-bead geometry measurement and estimation	93
7.2.3	Multi-bead width measurement	93
7.3	Third deposition experiment result	95
7.4	Simulation experiment result	104
7.4.1	Linear trajectory deposition	105
7.4.2	Circular trajectory deposition	107
7.4.3	Simulation discussion	108
8	Conclusion	116
8.1	Passive vision monitoring system	117
8.2	Simulated bead placement estimation	117
8.3	Future work	117
	References	120

List of Figures

1.1	WAAM system with a Kuka KR90 robot arm, welding torch, Kuka KP2 positioning table, Fronius power source, and wire feeder.	4
1.2	Deposition setup proposed for the Matlab simulation. Camera 1 assembled in a top-view configuration to get the bead width and centerline and camera 2 assembled in a lateral-view configuration to get the wire feeder deviation angle.	5
2.1	Generic stages of additive manufacturing steps [38].	7
2.2	Papers contributions published in technical journals within the WAAM theme. Retrieved from SCOPUS at 05/03/2022.	8
2.3	WAAM treemap contributions divided in their big areas of development. Retrieved from Web of Science at 05/03/2022.	9
2.4	Examples of parts printed with WAAM, industrial gas turbine blade (left) and titanium tank (right). Retrieved from https://waam3d.com/parts , at 04/10/2021.	9
2.5	World's first metal 3D printed bridge [35].	10
2.6	Process schematic: (a) GMAW, (b) GTAW and (c) PAW. Adapted from DING <i>et al.</i> [24].	12
2.7	Side view deposition of a wall with GMAW.	12
2.8	Block diagram for WAAM stages, adapted from DING <i>et al.</i> [27].	13
2.9	Correlation between defects presented in WAAM using steel. Adapted from WU <i>et al.</i> [65].	15
2.10	Input and output variables. Adapted from [48].	18
2.11	Torch travel speed and other indirect deposition parameters. Adapted from NAIDU <i>et al.</i> [48].	19
2.12	Torch side-view with some direct deposition parameters. Adapted from NAIDU <i>et al.</i> [48].	19
2.13	Relation between torch speed and weld bead characteristics, where the higher the TS the lesser is the penetration and the penetration width. Adapted from NAIDU <i>et al.</i> [48].	20
2.14	Captured frames during the monitoring and their different noises [17].	23

3.1	Cross-section profile of the single bead [17].	26
3.2	Single-bead cross-section model for the proposed models. Adapted from XIONG <i>et al.</i> [68].	27
3.3	Generic multi-bead example [17].	30
3.4	Multi-bead deposition example in WAAM [17].	30
3.5	Flat overlapping model (FOM) for multi-bead deposition, adapted from XIONG <i>et al.</i> [68].	31
3.6	Tangent overlapping model (TOM) for multi-bead deposition, adapted from DING <i>et al.</i> [22].	31
3.7	Multi-bead experiment with a 5 layers deposition used to verify the surface quality with tangent and flat overlapping models [22].	32
3.8	Influence of the overlapping area on the layers surface quality; (a) $d \geq w$, when there is no overlapping, (b) $d < w$, when the overlapping area is smaller than the total valley area, (c) $d = d^*$, when the overlapping area is equal to the valley area resulting in a theoretically flat surface, and (d) $d < d^*$, when the overlapping area is bigger than the valley area [17].	33
3.9	Wire feeding configuration (e.g. PAW) (a) and parameters (b) for front feeding assembly [37].	33
3.10	Effect on single beads position start and finishing varying its feeding angle (a) and height (b) [37].	34
3.11	High-speed images for the bridge (a) and globular (b) transfer modes, where in (a) $\Delta h = 0$ and in (b) $\Delta h = 0.5$. The bead surface quality for each transfer mode is also affected at each transfer mode [37].	35
3.12	The three types of wire feed in relation to the deposition direction [25].	35
3.13	Wire feed deviation issue example when monitored with a single camera [76].	36
3.14	Equipment and camera setup to print [76].	36
3.15	Wire deflection measuring with passive camera with the camera image view (a), deflection example (b and c), and the characteristics (nozzle normal line and wire centerline) used to measure the deviation (d) [76].	37
4.1	6-DOF robot printing a glass fiber composites and the homogeneous transformation representation from its base to the end-effector. Retrieved and adapted from https://www.compositesworld.com/articles/video-six-axis-robotic-arm-3d-printing-fiberglass-composites-03/25/2022	40
4.2	Stages used in the vision-based algorithm [17].	41

4.3	Image formation geometry for thin convex lens and a pin-hole. Adapted from [16]	42
4.4	Central-projection camera model, with the image plane located at the lens positive optical length f in front of the camera origin [16].	43
4.5	Point identified in reference to the camera and the world coordinate system. Adapted from CORKE [16].	44
4.6	Camera projection matrix with the intrinsic and extrinsic parameters for digital images.	45
4.7	Captured frames during the monitoring and their different noises [17].	46
4.8	A 3×3 kernel operator T applied to an image f in the spatial domain. Where the output image g is the result of T correlated in f . Adapted from GONZALEZ e WOODS [39].	47
4.9	Two kernels used in the smoothing process are represented. The left kernel result needs to be divided by 9 and the right by 18, which is the sum of all the kernel position data.	48
4.10	Impact of the kernel size at the output image (from left to right): (i) original image; (ii) output image after an smoothing operation with a 9×9 kernel; (iii) output image after an smoothing operation with a 35×35 kernel. Adapted from GONZALEZ e WOODS [39].	49
4.11	An example of a 3×3 kernel size.	49
4.12	Kernels used for the Laplacian operation over a function $f(x, y)$ (image). Where: (a) Kernel operator user to implement the expression 4.24; (b) Kernel user to implement the Laplacian operator, however now the diagonal therms are taken into account.	51
4.13	First-order derivative operators. Where (a) and (b) are the Roberts cross gradient operator, and (c) and (d) the Sobel operator.	52
4.14	Image segmentation example. Where (a) represent the raw image acquired and (b) the binary image with the desired features highlighted. [72].	53
4.15	Image capture after threshold	54
4.16	Edge detection operators comparison [47].	55
4.17	Line and point representation at xy -plane and ab -plane. Adapted from [39].	57
4.18	Line and point representation at xy -plane and $\rho\theta$ -plane. Adapted from [39].	57
4.19	Example of the Hough transform algorithm. Adapted from [16].	58

4.20	A random variable graph representation, where 68.3% of all values are inside the covariance range. Retrieved from https://www.mathworks.com/videos/understanding-kalman-filters-part-3-optimal-state-estimator-1490710645421.html at 03/25/2022.	59
4.21	A car state estimate example after one time step. Adapted from https://www.mathworks.com/videos/understanding-kalman-filters-part-3-optimal-state-estimator-1490710645421.html , retrieved at 03/25/2022.	61
5.1	Captured frames during the monitoring and their different noises [17].	63
5.2	Stages used in the vision-based algorithm [17].	64
5.3	Removing undesired lines.	66
5.4	Bead width and centerline computed by the algorithm.	66
5.5	Multi-bead cross-section profile in WAAM, where d is the overlapping distance between the beads centerlines, W_1 is the width measurement pattern for the first bead deposited and W_2 the width measurement pattern for the subsequent deposited beads, and $bead_k$ represents a quantity k of beads deposited [17].	68
5.6	Multi-bead deposition and vision monitoring setup. Camera, torch and wire amplified with their coordinate systems [17].	68
5.7	Filtering steps of the bead geometry estimation and localization algorithm.	70
5.8	Wire stick-out orientation using a passive vision sensor. Adapted from ZHAN <i>et al.</i> [76].	72
5.9	The Deposition setup proposed for the simulation. Camera 1 assembled in a top-view configuration to get the bead width and centerline and camera 2 assembled in a lateral-view configuration to get the wire feeder deviation angle.	72
5.10	Noisy wire angle deflection reading. Adapted from ZHAN <i>et al.</i> [76].	73
5.11	The block diagram of the pure pursuit algorithm with the unicycle dynamics. Adapted from CORKE [16].	75
5.12	Topside view of the system simulation with the unicycle representation above the bead.	75
6.1	First WAAM setup configuration with Motoman HP20 robot arm, welding torch, camera, and NX100 controller [49].	78
6.2	Gray-scale camera from Xiris used during metal deposition.	78
6.3	Single-bead specimens of the first experiment.	79
6.4	WAAM system with a Kuka KR90 robot arm, welding torch, Kuka KP2 positioning table, Fronius power source, and wire feeder.	80

6.5	Xiris XVC-1000 camera and the welding torch assembly used in the second deposition setup.	81
6.6	Schematic of the multi-bead deposition and vision monitoring setup. The camera, torch and wire are amplified with their coordinate systems.	82
6.7	Samples of the second single-bead experiment with constant and varying wire feed speed (Table 6.3).	83
6.8	Five bead layer sample of the second experiment. The deposition of all bead are performed in the same direction.	83
6.9	The sensors setup used in the third experiment.	85
6.10	Single-bead and multi-bead specimens, where the passes of the multi-bead specimens have different length.	86
6.11	Third deposition experiment five layer pad.	87
6.12	Side view of the deposition system simulation with the stick-out, distance from torch to the substrate and the wire feeder angle highlighted.	87
6.13	3D schematic of the Kuka KR90 2700 used in the simulation.	88
7.1	Median and Gaussian filters results in WAAM. Where low and high light scenarios are analyzed for both filters [18].	90
7.2	Edges of the bead (a) detected inside the region of interest using Laplacian (b), Sobel (c), Schar (d), and Canny (e) edge detection algorithms [18].	90
7.3	Video of deposition using CMT with the region of interest [18].	91
7.4	Bead width estimation of the first experiment with the usage of a mean filter [18].	91
7.5	Bead width measurement with low-pass band and moving average filtering [49].	92
7.6	Single bead width measured manually, where (a) and (b) are respectively the first and second position measured of the single-bead [49].	92
7.7	Width monitoring plot using different strategies.	94
7.8	Constant WFS, Sample A [17].	95
7.9	Varying WFS, sample B [17].	96
7.10	Varying WFS, sample C [17].	97
7.11	Varying WFS, sample D [17].	98
7.12	Multi-bead width monitoring at current layer [17].	98
7.13	Frames captured during the layer 5 deposition of the pad.	99
7.14	Bead width estimation for the multi-bead deposition using HDR camera.	100
7.15	Width estimation for every bead of bead layer 5 using HDR camera. .	101

7.16	Bead ghost present at the IR image even after the end of the deposition.	102
7.17	Specific frames captures from the multi-bead 4th pass.	102
7.18	Specific frames captures from the pad last layer.	102
7.19	Bead width estimation for the multi-bead deposition using the IR camera.	103
7.20	Width estimation for every bead of pad (layer 5) using the IR camera.	104
7.21	Trajectory performed by the robot arm during the multi-bead experiment.	105
7.22	Individual beads centerline placement estimation for the linear . . .	106
7.23	Manipulability computed for the linear trajectory.	107
7.24	Manipulability computed for the circular trajectory.	107
7.25	Real and estimated wire feeding angle along the linear deposition trajectory for a varying wire feeding angle.	108
7.26	Bead planned and performed path for a varying wire feed angle. The red circle represents the trajectory start and the green x represents the trajectory end.	109
7.27	Bead deviation along the linear trajectory for a varying wire feed angle.	109
7.28	Estimated, predicted and measured bead centerline localization along the trajectory for a varying wire feed angle.	110
7.29	Estimated and real centerline localization of the bead along the trajectory for a varying wire feed angle.	111
7.30	Real and estimated wire feeding angle along the deposition (a) for a varying wire angle and a circular trajectory. (b) and (c) are zoomed areas of the original angle estimation chart.	112
7.31	Bead planned and performed path for a varying wire feed angle and a circular trajectory. The red circle represents the trajectory start and the green x represents the trajectory end.	113
7.32	Bead deviation along the trajectory for a varying wire feed angle, and a circular trajectory.	113
7.33	Estimated, predicted and measured bead centerline localization along the trajectory for a varying wire feed angle, and a circular trajectory.	114
7.34	Estimated and real centerline localization of the bead along the trajectory for a varying wire feed angle, and a circular trajectory. . .	115
8.1	Topside view of the system with the deviation caused by a low quality wire.	118
8.2	Topside view zoomed of the control proposal for the bead placement and wire feeding while printing.	119

List of Tables

2.1	Comparison of WAAM techniques with their particular energy source and features. Adapted from WU <i>et al.</i> [65].	11
2.2	Path generation method with examples. Adapted from DING <i>et al.</i> [23].	14
2.3	References used for the TS used in WAAM.	20
3.1	Equations of common bead profile models [22].	29
5.1	Camera main parameters used in the camera perspective model. . . .	72
6.1	Process parameters of the first print experiment.	79
6.2	Chemical composition of the wire filler and the substrate.	79
6.3	Travel speed and wire feed speed used for the second single-bead experiment.	83
6.4	NIT Tachyon 16 IR camera main specification	84
6.5	Third experiment deposition information.	85
7.1	Measurements performed in the first and second halves of the plots. .	93
7.2	Bead width estimation values for the multi-bead deposition using Xiris HDR Camera.	96
7.3	Bead width estimation values for the layer 5 of the pad deposited using Xiris HDR camera.	97
7.4	Bead width estimation values for the multi-bead deposition using NIT IR camera.	100
7.5	Bead width estimation values for the layer 5 of the pad deposited using NIT IR camera.	103

List of Symbols

A_m	cross-section profile area, p. 28
Δh	distance variation from wire tip to the molten pool surface, p. 34
■	convolution operation, p. 47
\hat{V}	measurement covariance matrix, p. 76
\hat{V}	state transition covariance matrix, p. 76
□	correlation operation, p. 47
d	step-over distance, p. 26
d^*	overlapping optimal distance, p. 32
t_s	travel speed, p. 26, 28
w_d	wire diameter, p. 26, 28
w_s	wire feed speed, p. 26, 28
c	bead centerline, p. 31
d	step-over distance, p. 31
w	single bead width, p. 31

List of Abbreviations

AM	additive manufacturing, p. vii, 1, 6
CAD	computer aided design, p. 7
CCD	charge coupled device, p. 22
CMOS	complementary metal-oxide semiconductor, p. 22
CMT	cold metal transfer, p. 3, 10
CPU	central process unit, p. 89
DDP	direct deposition parameter, p. 17
DOF	degree of freedom, p. 38, 77
DOF	degrees of freedom, p. 69
EKF	extended Kalman filter, p. 61
EKF	extended Kalman filter, p. vii, 71
FOM	flat overlapping model, p. 31
GMAW	gas metal arc welding, p. 3, 10, 11
GTAW	gas tungsten arc welding, p. 10
HDR	high dynamic range, p. 4
IDP	indirect deposition parameter, p. 12, 17
IR	infrared, p. 4
MAM	metal additive manufacturing, p. 6
MA	manufatura aditiva, p. vi
MIMO	multiple-input and multiple-output, p. 17

MLE	maximum likelihood estimation, p. 75
NIT	new infrared technologies, p. 84
OEM	original equipment manufacturer, p. 6
O&G	oil and gas, p. 14
PAW	plasma arc welding, p. 10
ROI	region of interest, p. 89
ROS	robot operating system, p. 38, 77, 81
ROV	robot operated vehicle, p. 1
STL	standard tessellation language, p. 7
TOM	tangent overlapping model, p. 31
TS	travel speed, p. 18, 19
WAAM	wire arc additive manufacturing, p. vii, 1, 11, 14, 79
WFSTSR	wire feed speed and travel speed ratio, p. 28
WFS	wire feed speed, p. 26
WYSIWYB	what you see is what you build, p. 8

Chapter 1

Introduction

Robots and automation plants have more than ever become part of the manufacturing environments. They are used to improve the quality, production and also make the work environment safer for humans, where their use and reliability have already been proven, for example to weld and paint in the automobile industry. Welding, painting and coating are one of the more common applications of robots in industry due to their repeatability and accuracy. Small parts assembly are also largely done by robots. Their use to improve the quality, productivity and safety has already been proven. It can be said that in industry one of the major benefits of automation and robotic systems are to improve the safety of the workers. By reducing or even avoiding the necessity of humans in hazardous operations, e.g. in Oil & Gas segment, where the ROVs are used to inspect and intervene in subsea underwater operations.

It is possible to relate some Additive Manufacturing (AM) objectives with other already established technologies. It makes the work environment safer, increase revenue and also decrease the lead-time of parts to the end customer. AM can also increase the part design possibility, decrease the warehouse raw material stock, and be an advance in the manufacturing process by achieving the safety, quality, delivery and costs reduction requirements. Regarding the technology development and maturity stage, it is not yet ready for mass production part delivery or as an on-the-shelf product. There are many challenges yet to be overcome to make the technology feasible and spread it on different types of industry segments.

The junction of a wire feedstock with an electric arc as heat source is referred as Wire Arc Additive Manufacturing (WAAM) . It uses standard off-the-shelf hardware, like welding power source, torch, wire feeding system, robot arm and others common welding equipment [64]. In particular, WAAM has got the attention of industry due its high capability of producing large parts with moderate complexity having a relative high deposition material rate, capability of decrease material waste and consequently environmental friendly characteristics [65]. However, some challenges

rises when using wire as a feedstock, due to the high heat input. Deformation caused by residual stresses can occur and relative poor accuracy and surface finish also is a problem due its “layer by layer” build up characteristic [24].

Inspection is also an important stage of manufacturing, it helps defect detection, which increases the reliability of the product. However, the task of quality evaluation is not trivial and when defects, such as discontinuities, cracks, porosity, and others, need to be quantified and coded in terms of computer operation becomes even harder [15]. Generally to ensure the quality of the part printed, the inspection is performed with gauges and touching measurement tools, normally carried out by trained and qualified personnel. Visual inspection is the most used for external inspection. In welding it is used to check external damage, delamination and corrosion in the surface for example. One of the limitations in vision inspection is the lack of a clear acceptance rule which it not very objective in some cases [13].

This work focus on the development of a reliable vision monitoring system, which is performed with passive vision sensors, where a software capable of gathering information about the weld bead in real-time is developed. The characteristic to be estimated by the monitoring system is the bead width. The weld bead width mapping can be used to improve the quality of the final part, by ensuring the designed overlapping was successful through the deposition trajectory. In order to make reliable measurements, the algorithm should be capable of handling the uncertainties and noises in AM using electric arc for material deposition. Online monitoring during deposition, also creates a possibility for developing a defect detection system by monitoring in real time the width variation rate and also a control algorithm capable of compensating errors due to process inaccuracies [20]. Therefore, the contribution of the current work is focused in development of a reliable monitoring system capable of be used with HDR cameras without the necessity of additional algorithm or measurement from the process, also the bead placement estimation performed creates an opportunity of developing a smart WAAM system, capable of closed loop control and defect detection as mentioned

1.1 Motivation

During the research about WAAM and its overall implementation in industry, it was possible to notice the advantages of its use nowadays and also its limitations. A reliable online measurement of the deposition characteristics can be used in different scenarios to improve the technology, lowering the necessity of interventions and manual measurements. As sensing by touching measurements instruments is not a good option due to the process characteristics, measurement is recommended through the usage of lasers and cameras.

The problem of extracting features when using these sensors arises due to the noise ratio embedded in the process and its nonlinear characteristic, mainly in process like GMAW-based such as CMT due its short-circuiting characteristic. To achieve an online and reliable monitoring system in this scenario is a challenge and requires continuous improvements. The surface quality also suffers from the impact of having the bead width and its placement through the deposition out of the designed characteristic.

Due to these factors, a vision-based monitor system is developed using passive-vision sensors, since it acquires a high amount of valuable data and can be implemented successfully with the available technology. Vision is also an intuitive and well understood sensing method by users since today is broadly applied to monitor, map, measure, and in daily use for photography with the popularity of smartphones. In additive manufacturing, its development is very important due to its high data transfer capability, smaller size and lower cost when compared with other measuring equipment.

The possibility of ensure the quality of the part produced is relevant for the industry, and to implement the usage of WAAM e.g. in the O&G industry. Therefore, the development of the current algorithm capable of monitoring the bead characteristics without the necessity of specific hardware and additional information from the system is relevant as today the process lacks a commercial software for the measurement of such information.

1.2 Objective

The objective of this work is to create vision-based algorithm capable of monitoring the bead characteristics during the deposition process. The algorithm must be able to reliably perform real-time estimation of the bead width in the single-bead or multi-bead scenarios, as well as the positioning of the bead centerline.

1.3 Methodology

To reach the objectives, a set of experiments are proposed to test and select the adequate image smoothing filters, edge detectors, and segmentation method. The collected data will be used to access the performance of the proposed filtering algorithms. Therefore, the following experiments are proposed:

1. Single-bead deposition.
2. Single-bead deposition with varying travel speed and a first multi-bead monitor test.

3. Multi-bead deposition composed of a single layer and a pad of five deposited layers.

The monitoring is performed with a single HDR camera for the first two experiments and with two cameras, one HDR and one IR, for the last deposition experiment. The deposition setup is composed by the passive vision cameras, a 6-DOF robot arm, and a CMT deposition system. An example of the system used at the first deposition is shown at Figure 1.1.

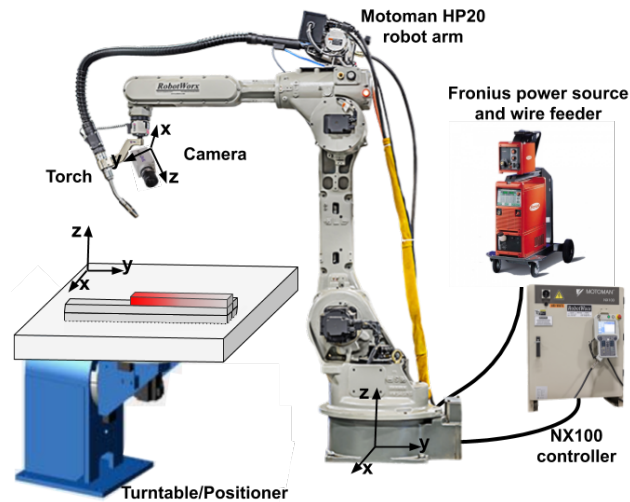


Figure 1.1: WAAM system with a Kuka KR90 robot arm, welding torch, Kuka KP2 positioning table, Fronius power source, and wire feeder.

A simulation with Matlab for independent wire processes like PAW with two cameras (Figure 1.2) is developed to estimate the bead centerline. The first camera is located in a top-side view configuration where it focus on the bead formation, while the second one is in a front-view configuration to capture the wire feed deviation in real-time. The second camera is specially used to predict the bead placement since it monitors the wire feeding deviation along the deposition trajectory.

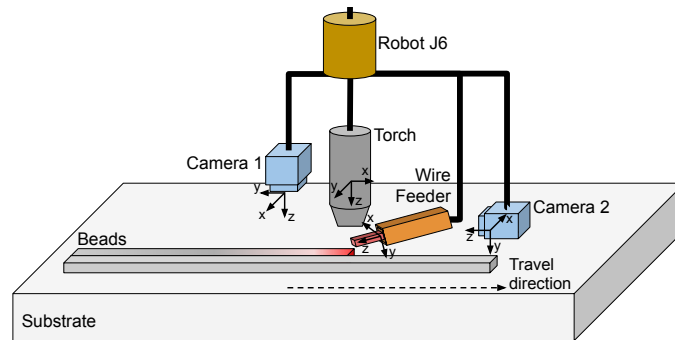


Figure 1.2: Deposition setup proposed for the Matlab simulation. Camera 1 assembled in a top-view configuration to get the bead width and centerline and camera 2 assembled in a lateral-view configuration to get the wire feeder deviation angle.

Chapter 2

Additive Manufacturing System

Additive manufacturing (AM) is the process of producing 3D parts from a CAD (Computer-Aided Design) without the need of specific process tooling to manufacture a part with distinct geometry and internal characteristics [38]. In some references, 3D printing is also used as a synonym for Additive Manufacturing [65]. The technology was originally developed to manufacture polymeric, paper laminates and waxes materials. It caught the attention in recent years of many industry segments due its benefits, such as, a reduced material costs and a higher part design freedom. Basically, it consists of a process in which a material is deposited gradually, being build up layer-by-layer [58]. Additive Manufacturing consists of a combined motion and heat system with a chosen feedstock that is used to build up parts through material deposition [64].

The technology gives Original Equipment Manufactures (OEM) , from different industry segments an opportunity for reaching new costumers, reducing costs and attending environmental goals by raising sustainability. The biggest strength of the technology lies in traditional manufacturing process limitations, enabling a new approach to engineering part design and manufacturing when requested as possible new solutions. Overall, it enables the production of complex structures while maintaining stability in lighter designs [58].

AM has helped small companies and individual personnel to develop customized parts and easier prototyping, mainly focusing on small parts. One of the interests is its development for large parts build up. It also has the focus on minimizing the cost and time spent to manufacture prototypes, optimize profits and results [34]. However, producing large size parts increases problems like surface roughness and lower accuracy. For traditional MAM systems, some additional process steps are used to guarantee the correct material properties of the end part, for example, heat treatment and machining. Using robot manipulators with AM, helps to work "outside the box" opening new possibilities for the process [20]. Increasing the process flexibility and the possibility of producing large structures.

The part produced with AM is printed in layers with a predefined height. In the planning stage, the deposition parameters are designed to achieve geometric accuracy, desired deposition rate, and satisfactory mechanical properties. A generic additive manufacturing system can be separated in at least eight main stages: (i) CAD design; (ii) STL conversion; (iii) file transfer to machine; (iv) machine setup; (v) build up; (vi) remove; (vii) post-processing; (viii) application; as shown in Figure 2.1 [38].

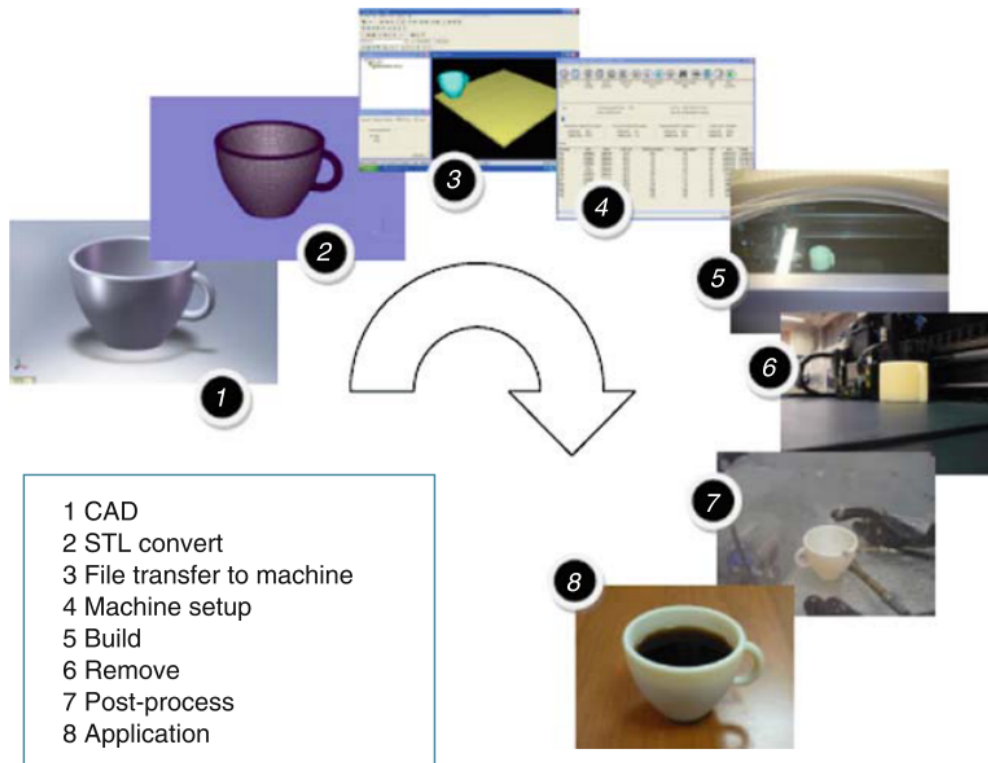


Figure 2.1: Generic stages of additive manufacturing steps [38].

These stages have specific definitions with “CAD” being the stage which the part is modeled using a dedicated software (Solidworks, Fusion360, Inventor or others) and a 3D solid is created, “STL convert” converts previously stage file output to STL format, “File transfer to machine” transfers the STL file to the AM hardware and than manipulated as necessary, “Machine setup” the deposition parameters and energy sources are configured, “Build” is done most automatically with some monitoring to ensure no errors, “Remove” the part is removed from the build platform, “Postprocessing” additional material is removed by manual cleaning or machining and manual manipulation or part produced, and in “Application” part is ready for use but in some cases it can also need additional treatments such as painting, washing, heat treatment [38].

Additive manufacturing has been described as a revolutionary technology, with the possibility of making current manufacturing technologies obsolete if developed

to its ultimate conclusion. It has a advantage of speeding up, from the concept step to manufacturing a part. The seamless characteristics of the part produced is also an advantage, reducing the steps required during manufacturing and delivering the concept of what you see is what you build (WYSIWYB). Also has the potential to simplify the manufacturing and to keep the workshop environment much cleaner, and versatile when compared to traditional manufacturing facilities [38].

2.1 Wire arc additive manufacturing

Recently, wire arc additive manufacturing (WAAM) has got the attention of manufacturers from different industry segments due to its potential capability to produce parts with distinct geometry without the necessity of specific tools. It also benefit industry since it allows rapid, decentralized, and flexible manufacturing as well as serial production. WAAM is the junction of wire feedstock with an electric arc as a heat source, all guided by a robotic system to enable the buildup of a designed part [64]. A research restricting WAAM as the keyword in two science research databases (SCOPUS and Web of Science) has shown the growing interest of the academy community as described in Figure 2.2. Which reinforces the relevance of the proposed theme.

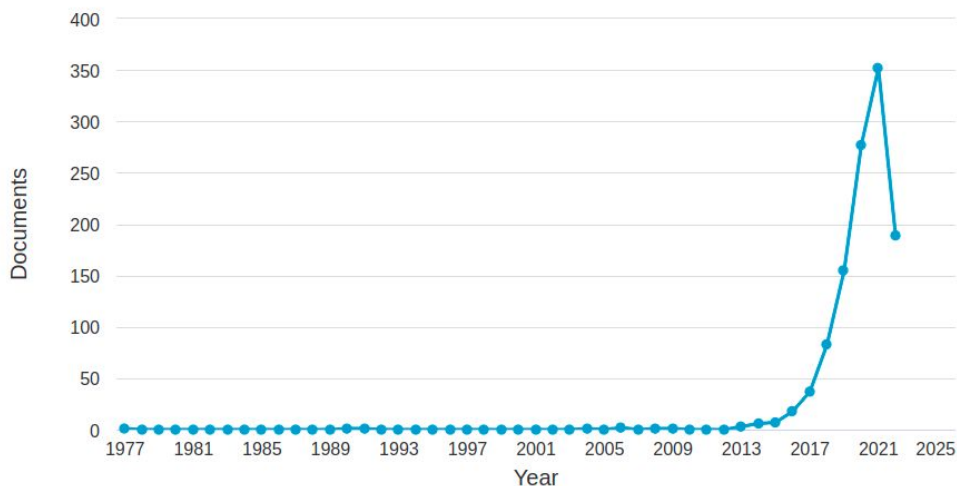


Figure 2.2: Papers contributions published in technical journals within the WAAM theme. Retrieved from SCOPUS at 05/03/2022.

It is also important to highlight the multidisciplinary characteristics of the technology, contemplating materials, metallurgy, robotics, automation, and other disciplines for its development as detailed in Figure 2.3.

In particular, WAAM has the capability to produce large and complex parts with high deposition rate, little material waste, and consequently, friendly environmental characteristics [65]. However, some challenges arise when using metal wire as

feedstock. Due to the high heat input required to print the part and the metallurgical characteristics of the alloy, deformation can occur during the cooling stage and cause residual stresses, increasing the risk of defects. A good example of study that represent numerically the heat transfer in WAAM is performed by FRAGA *et al.* [34], where the model considers exchange with the environment by radiation and convection. Poor geometric accuracy and surface finishing of the part are also problems during its layer by layer buildup characteristic [24]. Examples of parts produced with WAAM are shown in Figure 2.4 and Figure 2.5.



Figure 2.3: WAAM treemap contributions divided in their big areas of development. Retrieved from Web of Science at 05/03/2022.

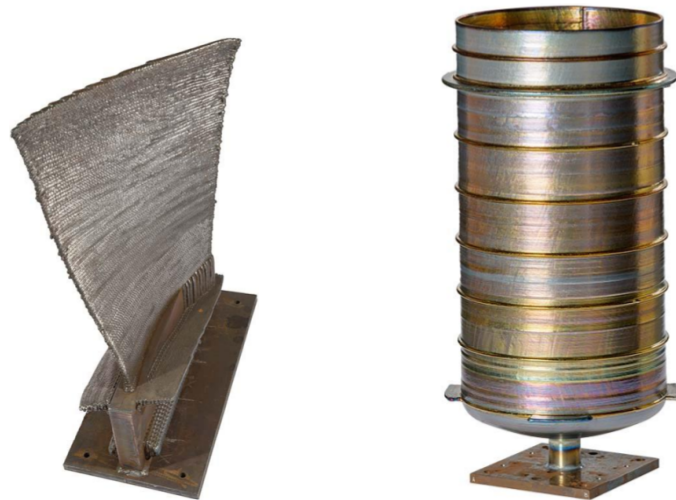


Figure 2.4: Examples of parts printed with WAAM, industrial gas turbine blade (left) and titanium tank (right). Retrieved from <https://waam3d.com/parts>, at 04/10/2021.

Wire arc additive manufacturing works by depositing melted metal layer by layer, it can use different types of power source for melting the wire. The most common



Figure 2.5: World's first metal 3D printed bridge [35].

welding technology that are applied in WAAM are gas metal arc welding (GMAW), gas tungsten arc welding (GTAW), and plasma arc welding (PAW) [28, 50, 65]. The Table 2.1 describes possible WAAM systems with a set of power sources and its main features.

The GMAW process operates with metallic alloy wire that is both the electrode and the buildup material. And in WILLIAMS *et al.* [64] it is stated that GMAW is commonly the process of choice to the fact that "the wire is the consumable electrode, and its coaxiality with the welding torch result in easier tool path". The same group of researchers supports the usage of CMT, developed by Fronius, due to its controlled dip transfer which provides lower heat input deposit, great stability, and nearly to without spatter. By analyzing the table 2.1 and the previous information, it is possible to conclude that CMT is a reliable option for WAAM. Since it has good

Table 2.1: Comparison of WAAM techniques with their particular energy source and features. Adapted from WU *et al.* [65].

WAAM	Energy Source	Features
GTAW-based	GTAW	Non-consumable electrode; Separate wire feed process; Typical deposition rate: 1-2kg/hour; Wire and torch rotation are needed;
GMAW-based	GMAW	Consumable wire electrode; Typical deposition rate 3-4 kg/hour; Poor arc stability, spatter;
	CMT	Reciprocating consumable wire electrode; Typical deposition rate: 2-3 kg/hour; Low heat input process with zero spatter; High process tolerance;
	Tandem GMAW	Two consumable wires electrodes; Typical deposition: 6-8 kg/hour; Easy mixing to control composition for intermetallic materials manufacturing;
PAW-based	PAW	Non-consumable electrode; Separate wire feed process; Typical deposition rate 2-4 kg/hour; Wire and torch rotation are needed;

deposition rate in comparison with other heat input process while also maintaining a good level of stability in the deposition process. If compared to regular GMAW is also has the advantage of a lower heat input, reducing residual stress and distortion in the produced part.

A schematic of the three main process used in WAAM is show in Figure 2.6. In GMAW the arc is formed between the consumable electrode and the workpiece, on the other processes, GTAW and PAW, the arc is formed using a non-consumable tungsten electrode, with the feedstock being supplied separately. Between the last two processes the biggest difference is the high temperate zone of the arc being narrower and the two gas flows (shielding and plasma gas) in the PAW [24].

A side view example of a wall being deposited is shown in Figure 2.7, which describes a three layers build-up using GMAW as the power source for melting the wire. The image color gradient “red to gray” is used to shown a simplified version of the thermal dissipation considering only the last layer single bead. For GTAW or PAW process the wire would be fed independently of the torch.

2.1.1 Steps used during WAAM

The basic steps to produce a part with WAAM are shown in Figure 2.8, are: (i) design and adapt the part to be printed inside a CAD software for the desired

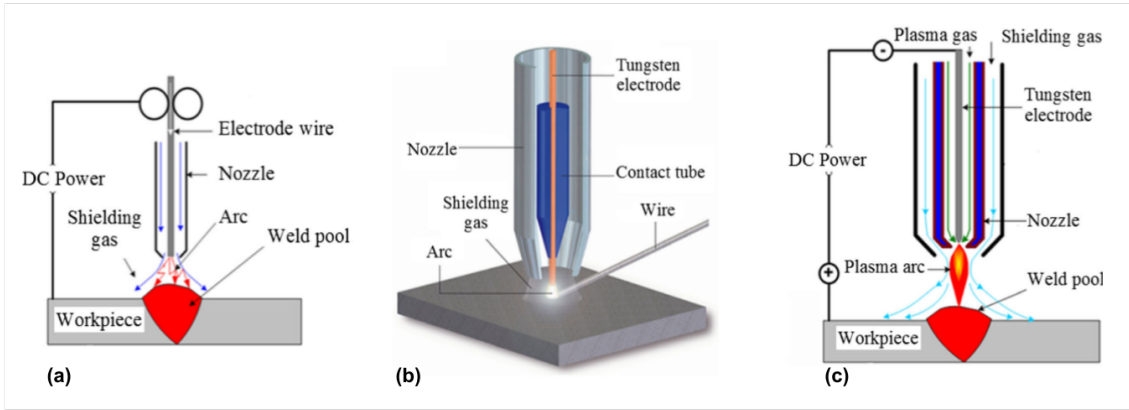


Figure 2.6: Process schematic: (a) GMAW, (b) GTAW and (c) PAW. Adapted from DING *et al.* [24].

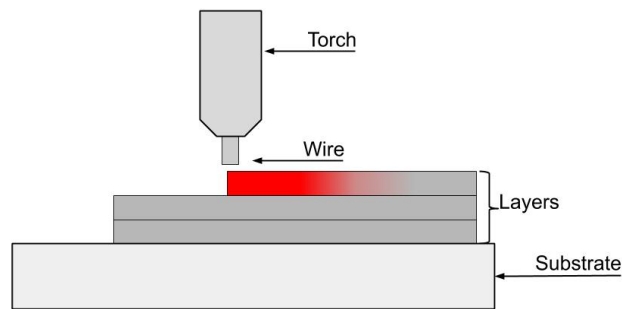


Figure 2.7: Side view deposition of a wall with GMAW.

manufacturing process requirements, in this case WAAM; (i) Define the layer height and proceed to the slicing step with dedicated software, which slices the 3D part into a set of 2.5D data, since it contains height information; (ii) Define the path through which the torch will be guided by the robotic system; (iii) specify the desired bead geometry during the print; (iv) define the indirect deposition parameters (IDP) to achieve the desired characteristics; (v) setup the deposition parameter to the power source and send the trajectory to the robot; (vi) build-up the part; (vii) Execute the post-processing step as required to achieve the designed surface finish or geometric accuracy [27].

2.2 Path planning

Path planning is an important step in a part production, and it is performed right after the slicing step. Many path patterns have been developed for additive manufacturing and are also used for WAAM, however, not all of them are suitable for WAAM due to some physical requirements and limitations. The path performed during the print influence the occurrence of distortion and residual stress, so, choosing a adequate path for the manufacturing process improves the quality of

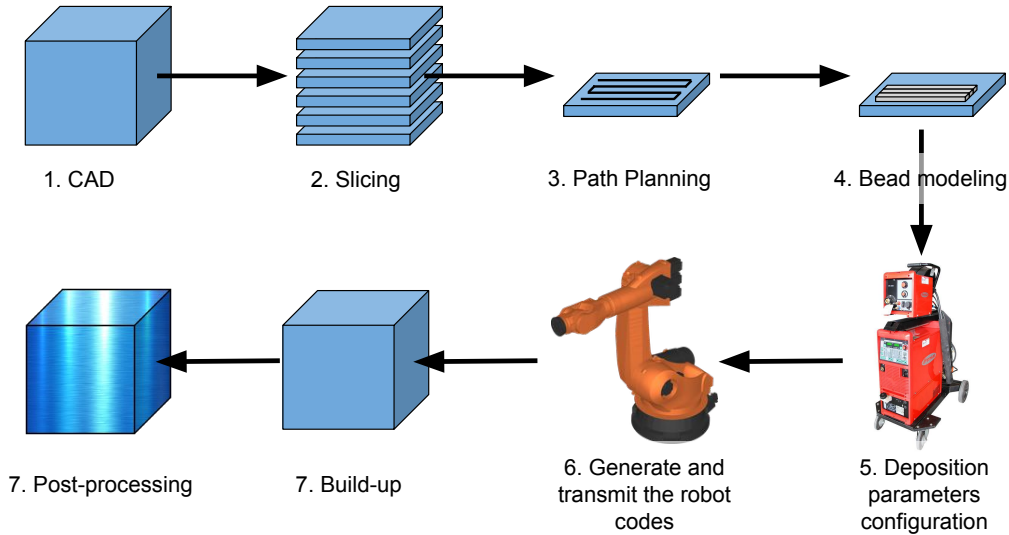


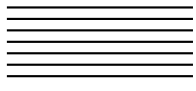
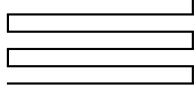
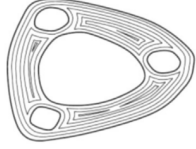



Figure 2.8: Block diagram for WAAM stages, adapted from DING *et al.* [27].

the part [26, 65]. An optimum path planning aims for a smooth layer surface, void-free deposits and satisfactory thermal dissipation, and needs to respect a defined distance between adjacent pass (step-over distance) that is directly related to the width of the bead being deposited. Another concern is to avoid abrupt changes in the path direction, as it tends to generate localized errors [26].

When selecting a path pattern it is important to consider minimum electric arc extinguishing points. Complex paths and intersection should be avoided as possible. The tool-path is defined as a continuous deposition of material with a single start and stop. Some path generation methods used in additive manufacturing are described in Table 2.2, being also used to print parts in WAAM.

Thinking in the limitations embedded with the usage of wire as feedstock some path patterns might be preferred or not recommended for WAAM. For example, raster pattern have a set of discontinuities, requiring many start and stop points in the deposition and deposit material in the same direction which can lead to a poor build quality. Zigzag is derived from raster strategy and is the most popular method used in AM systems. It is a continuous path and can increase the productivity by reducing transition motions from start to end, however, it has an accuracy error in the printed part outline. Zigzag can also present heat accumulation in certain regions, as frequently changes its direction path. Contour changes the direction frequently, by following the boundary curves of the path, however, it also present some potential gaps while printing depending of the geometry and features in the sliced layer. All these path patterns must cover the layer respecting the distance specified between adjacent passes [21, 23, 26].

Table 2.2: Path generation method with examples. Adapted from DING *et al.* [23].

Path generation method	Example	Reference
Raster		[30]
Zigzag		[51, 53]
Contour		[32, 43, 73]
Spiral		[54, 61]
Continuous		[3, 21, 31, 63]
Hybrid		[42, 77]

2.3 WAAM-fabricated components common defects

WAAM has a lot of research areas being developed to enable its commercial distribution as an off-the-shelf technology. For application of these parts in critical conditions, such as O&G offshore facilities, some defects must be investigated. Porosity, residual stress, void and cracking are some of the defects that must be avoided during part production for hazardous conditions. These defects can occur due to non optimum trajectory design, poor deposition parameter setup, deformation associated with heat accumulation, bad wire quality, contamination and other machine malfunctions [65].

These types of failures can also happen with other manufacturing processes. However, WAAM has an important characteristic, the possibility of monitoring the deposition characteristics during the entire manufacturing. In WAAM, a part is manufactured by depositing material layer by layer and this is an opportunity of improvement when compared to the traditional manufacturing processes. With the

possibility of monitoring the process with non-touching sensors and extract valuable information, improvements regarding failure mitigation can be achieved. Figure 2.9 describes a vulnerability ratio between printing with steel and each possible defect.

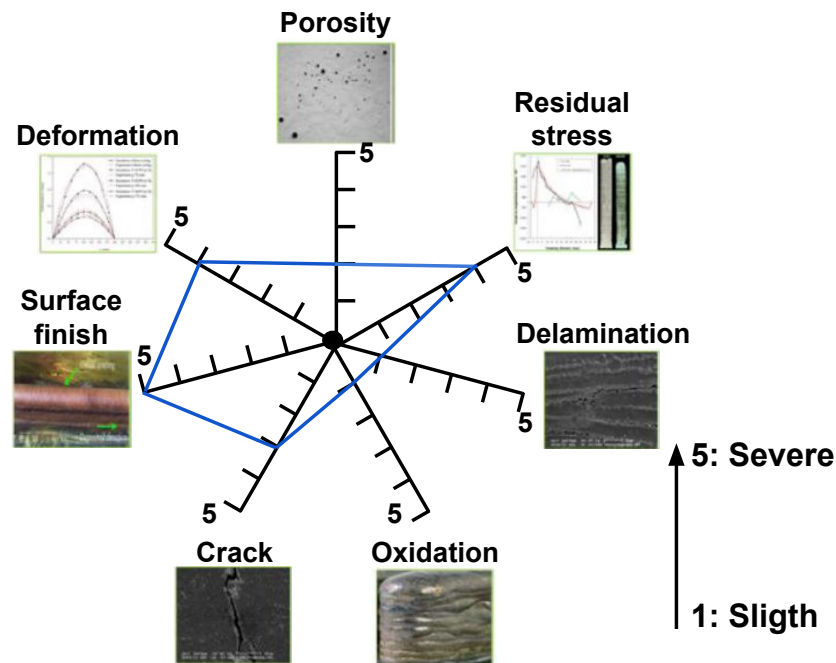


Figure 2.9: Correlation between defects presented in WAAM using steel. Adapted from WU *et al.* [65].

2.3.1 Residual stress

The part mechanical failure, in this case distortion, is mostly caused by residual stresses inherited from wire arc additive manufacturing. Avoiding it completely is not possible, therefore ways to deal with this problem must be developed and studied for the produced geometry. The residual stress caused by the process as already mentioned leads to distortion, loss of geometric tolerance, surface delamination and fractures during the deposition. Controlling and handling with residual stress is a key aspect of the process [65].

Residual stress is the internal tension that remains in the part after all external forces are removed. This characteristic is caused by the thermal expansion and shrinkage during the deposition process and a high heat input, causing several types of distortion, which is a big problem for large thin wall parts [28, 65].

2.3.2 Porosity

It is another common defect present in WAAM, and must be minimized to keep adequate mechanical properties of a printed part. Porosity may be caused by several

factors, such as, contamination in the wire or on the surface where the material is deposited, gases trapped inside the solid, poor path planning, unstable deposition process, and insufficient fusion or spatter ejection in complex deposition path that might create gaps or voids in defined regions (when torch velocity vector orientation changes fast). Some methods can be adopted to minimize the occurrence of porosity, like [65]:

1. Suitable deposition process to the material being used;
2. High quality gas supply system;
3. A clean wire and substrate surface before fabrication;
4. High quality feedstock;
5. Optimized bead shapes;
6. Monitor and control the thermal profile;
7. Treatments after deposition, such as rolling.

2.3.3 Delamination

Delamination happens due to insufficient or incomplete melting between adjacent layers deposited. Its appearance in the part produced is related to the thermal signature during printing and also the characteristics of the material being deposited. This defect is mainly visible, which can be detected by vision inspection, vision sensor or thermal reading during manufacturing. It is not possible to correct this defect with post-process techniques, however, preheating of the substrate might prevent its occurrence and need to be considered [65].

2.3.4 Quality assurance

Currently, most of the part quality assessment relies completely on human evaluation based on specifications established in industrial standards. Inspection requires training and process knowledge, which demands considerable time, increasing the costs and impacting the lead-time. Usually, inspection is performed with manual tools, such as gauge, scale and others. Vision inspection is commonly used for detecting external defect after the print. Many experiments based on vision are performed in lab environment successfully; however, they need further testing in the industry to ensure process safety and efficiency [13]. One application of vision-based sensing is a detection system to analyze the surface of each deposited pass in 3D printing and to track the joint groove in welding [74].

The characteristic's monitoring of the deposited material is also important and plays an important role in the development of the technology to enable its application widely in the industry. [33] developed a system for tracking the bead width in PAW deposition using passive vision with a camera in a top-view layout. This process has a higher signal-to-noise ratio when compared with GMAW, and the possibility of acquiring more valuable information from the image, like the wire feeding angle. [52] used a single high-refresh-rate camera to measure the weld bead height and width, obtaining satisfactory results. The weld bead width was estimated indirectly from the measurement of the molten pool width. However, in this case, the width measurement assumes symmetry in the bead profile. [71] also used passive vision for seam tracking in GMAW to ensure the correct position of the torch. Passive vision is widely used during welding and material deposition.

A set of factors contribute to the fabrication of high quality parts and minimize the occurrence of defects, like: *(i)* To monitor and compensate possible deviations in trajectory and/or parameters during the print [76]; *(ii)* Post-process options, like the rolling [14], the heat treatment, and others; *(iii)* feedstock optimization with high quality wires; *(iv)* adequate process selection and parameter design. All these factors contribute to minimize the occurrence of defects during fabrication.

2.4 Direct and indirect deposition parameters

Deposition parameters can be classified in two specific classes, direct deposition parameters (DDP) and indirect deposition parameters (IDP) , refereed in NAIDU *et al.* [48] as welding parameters and adapted in this work to deposition parameters. DDP are related to the characteristics of the material deposited, such as bead geometry, reinforcement, fusion zone geometry, mechanical properties of the metal deposited, and others, they are called deposition characteristics is this document. IDP are the configurations used to result a desired characteristic, some of them are the current, voltage, travel speed, and others. In Figure2.10 it is described the input/output variables for the deposition process.

For example, the objective of the planning stage is to choose a set of IDP that result in the desired DDP for the metal being deposited, ideally resulting in a part without defect and with satisfactory mechanical properties. In Figure2.10 it is demonstrated the welding or deposition as a multi-input and multi-output (MIMO) multivariable system.

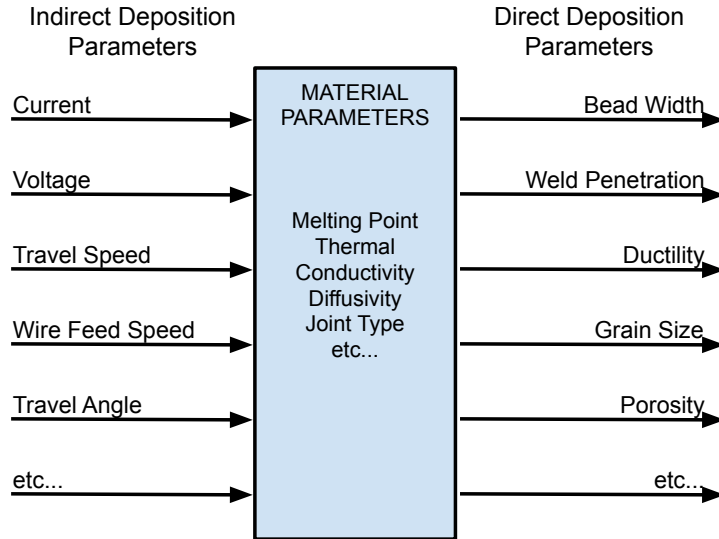


Figure 2.10: Input and output variables. Adapted from [48].

2.4.1 Torch travel speed

Travel speed (TS) is an independent deposition parameter that depends on the robot trajectory (path and time restrictions) since it is determined by the deposition process. TS is computed as the torch linear velocity tangent to the deposition path, as shown in Equation 2.1. In WAAM it is important that the travel speed is kept constant to avoid variation in the geometry being deposited.

$$TS = \sqrt{V_x^2 + V_y^2} \quad (2.1)$$

Figures 2.11 and 2.12 describe some of the parameters that must be specified before a deposition with GMAW. The Travel speed, contact tube to work distance, and the shielding gas flow rate are some of the parameters defined in the planning stage and executed by the deposition system during the deposition.

In GMAW the wire is fed through the torch with a shielding gas to protect the electric arc area during printing, these aspects are represented in Figure 2.12. In PAW and GTAW, the wire is fed independently of the torch and due to this factor some additional challenges arise, e.g. the feeding angle deviation caused by a low quality wire [76].

2.4.2 Travel speed influence on metal deposition

As specified by NAIDU *et al.* [48], TS influences some of the desired bead characteristics and must be kept constant during the printing to avoid variation in the bead geometry. TS also has direct influence in some DDPs, for example, in the penetration and bead width. So as TS increases, the aforementioned

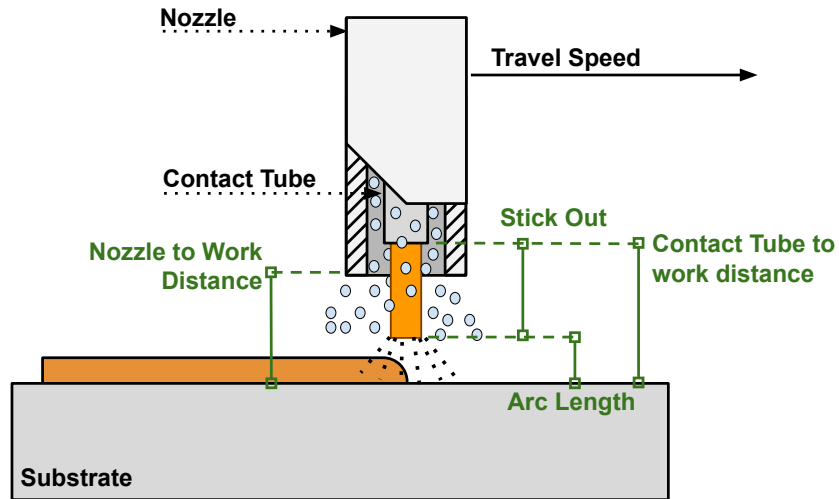


Figure 2.11: Torch travel speed and other indirect deposition parameters. Adapted from NAIDU *et al.* [48].

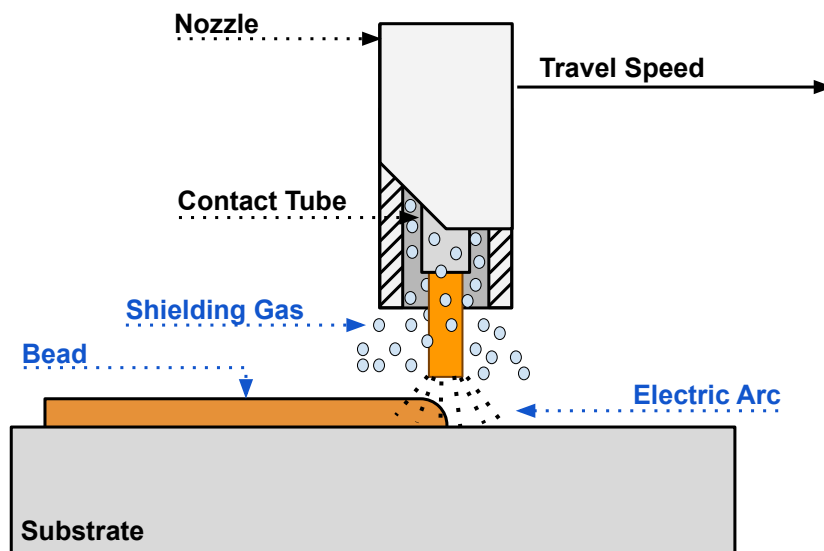


Figure 2.12: Torch side-view with some direct deposition parameters. Adapted from NAIDU *et al.* [48].

DDPs decreases. A simple relation of the torch travel speed and some deposition characteristics, also called direct deposition parameters in this work, is shown at Figure 2.13.

2.4.3 Travel speed reference

Travel speed (TS) is an important parameter that must be take into account when planning the deposition of a part, since it has impact the penetration, and also the bead geometry (height and width). The authors cited in Table 2.3 mainly used the

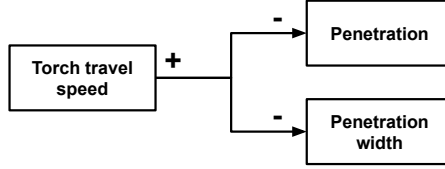


Figure 2.13: Relation between torch speed and weld bead characteristics, where the higher the TS the lesser is the penetration and the penetration width. Adapted from NAIDU *et al.* [48].

travel speed within a range of 1.66 mm s^{-1} and 8.33 mm s^{-1} for their experiments. In the current work the deposition and also the proposed simulation of the trajectory performed by the robot arm and the bead placement use a travel speed varying between 1.66 to 16 mm s^{-1} .

Table 2.3: References used for the TS used in WAAM.

Authors	WILLIAMS <i>et al.</i> [64]	RIOS <i>et al.</i> [55]	BANDARI <i>et al.</i> [2]
Travel speed	3.33 → 8.33	2.00 6.00	7.66
Units	mm s^{-1}	mm s^{-1}	mm s^{-1}

The optimal travel speed values in most cases are achieved through experiments, which also vary accordingly to the type of material being used during welding or printing operations. To the robot motion simulation, it is used a tool travel speed range varying from 1.66 to 16 mm s^{-1} .

2.5 Vision-based sensing

In welding and WAAM, vision is used to acquire information of the molten pool and the weld bead, and can be used for tracking, guiding and feed back control. Vision-based sensors are divided in two categories, passive and active sensors, which are classified according to the image light source used [10, 66]. A reliable monitoring system is a key aspect of quality assurance during an additive manufacturing process.

By analyzing the buildup characteristics of the deposition, it is possible to assume that if the buildup was finished as planned, then the probability of defects in the final manufactured part is minimized. Moreover, mapping the bead geometry, mainly the bead width and its centerline position along the reference trajectory, can also help the inspection stage. Deposited areas where the geometry is not in accordance with the specification have greater chance of presenting defects and can be tracked during the inspection.

Online measurement of the characteristics is important to enable closed loop control of the deposition parameters during the 3D printing process. This can

increase the productivity, lower the manufacturing costs and improve the reliability of the manufactured components. Vision-based sensors are a good option to this application due to its non-contact measurement capabilities.

The acquisition of the process characteristics in WAAM can be performed through sound and vision. It is preferable to use good sensors, that have a higher signal-to-noise ratio [36]. In some cases multi-sensor are also used in the manufacturing process to improve the accurate of the measurement [8]. Measuring the same signal with more than one sensor is a good option since it enables better implementation of filters, decreasing the impact of the noise in the measurement.

2.5.1 Vision-based sensor

Vision-based sensors also provide a large quantity of information to work with, they are used to gather information of the molten pool, the bead and other welding or deposition characteristics. Their non-contact capability is also important in welding and WAAM due the nature of the processes. These information are used for tracking, guidance and also feedback data to a controller. Vision sensing can be divided in two types, passive and active sensing, and are mainly classified in according to how light source is being supplied [11, 66]. The image retrieved always have noise [78] and need to be filtered to enable a constant and correct feature extraction.

Active vision sensing

Active vision sensing requires an internal light source, for example, a laser or other assistance light for the process to be monitored. In welding, active vision is used to restrain the arc's light interference; however, it is expensive to be applied in common welding process [11].

Passive vision sensing

On the other hand, passive vision works without the assistance of a light source, using only the energy provided externally, in this case by the arc itself. Passive vision is considered a practical way of monitoring weld pool characteristics and it is also cheaper than active vision, being preferred for monitoring and control welding processes. It provides enough information and can overcome some problems of laser tracking systems, like the look-ahead detection [66, 70, 71].

However, the usage of passive vision has the disadvantage that the vision system becomes more susceptible to process noise, since it uses external energy to acquire data. So, the implementation of filters to wipe off disturbances in the acquired data (image) is required, e.g. CMT results in a highly noisy image of the deposition due to its systematic open and close arc characteristics.

2.5.2 Active and passive vision sensors application

Some examples of active and passive vision systems are the laser sensors and cameras. Laser sensor are easier to utilize, they are focused on point recognition, and have some advantages due its laser light intensity that is little affected by the electric arc light. Because of this characteristic is a good option in high noisy environment such as arc welding [75]. Some of the characteristics of a laser sensor is: (1) in some wave lengths it has a higher light intensity when compared to the electric arc light; enables a clear observation of the phenomenons while printing; (2) no time delay; (3) robust to be used in highly noisy environments [75]. However some of the disadvantages of the active vision-base sensors are: (1) high cost; (2) usage complexity; (3) large volume [62].

On the other side, charge coupled device (CCD) cameras are capable of supplying abundant information but their image have more noise. E.g. image splash, dust, electric arc light variation and others characteristics affects more these cameras and are considered noise [12, 72]. The most common vision sensors used for monitoring bead and molten pool characteristics are: (1) laser beam-based equipment (e.g. profilometer); CCD and CMOS cameras; and thermal cameras.

To extract the desired features and measure the characteristics of the process, some steps are commonly used: (1) color space conversion; (2) smooth filtering; (3) segmentation; (4) edge detection; (5) line detection [9].

The implementation of cheaper sensors in WAAM are also relevant to make the technology more accessible. An example of a low cost vision sensor is implemented on LUO *et al.* [44], an off-the-shelf digital camera with HDR capability was used to collect information during arc welding. It replaces a $120dB$ dynamic range dedicated HDR camera with multi-exposure support common used during these types of monitoring. These digital cameras are a lot cheaper than those build specific for capturing images during welding. However, more noise reduction algorithms needs to be used to obtain a high quality image.

2.5.3 Noises present in the vision system during the deposition

WAAM is performed in a very complex environment, with many types of noise present during the process. Generating a necessity to process and filter the information acquired. Some of those noises are: (i) Non-uniformity of the surface (oxidation, marks, dust, etc); (ii) the arc itself; (iii) Types of material and its unique characteristics; (iv) mechanical vibration; and many others. The environment, platform, cable lines, jigs, changing in light and others that can also be considered as noise, which make the acquisition of data a challenge. When designing processing

algorithms these details must be taken into account [12].

The amount of noise present in the image is one of the factors that must be studied during the development of the vision-based algorithm. Some of those noises can have a big impact in image quality and are hard to be treated without losing sharpness that is very important to the measuring process. As mentioned before, the material that is being deposited is also considered noise depending of the vision sensor used. For example, with 3D scanners a polished surface can be a problem because of the reflection rate it has, generation of many noises and loss of data. Figure 2.14 shows examples of noise in WAAM, as fumes, arc radiation, light variation, and spatter.

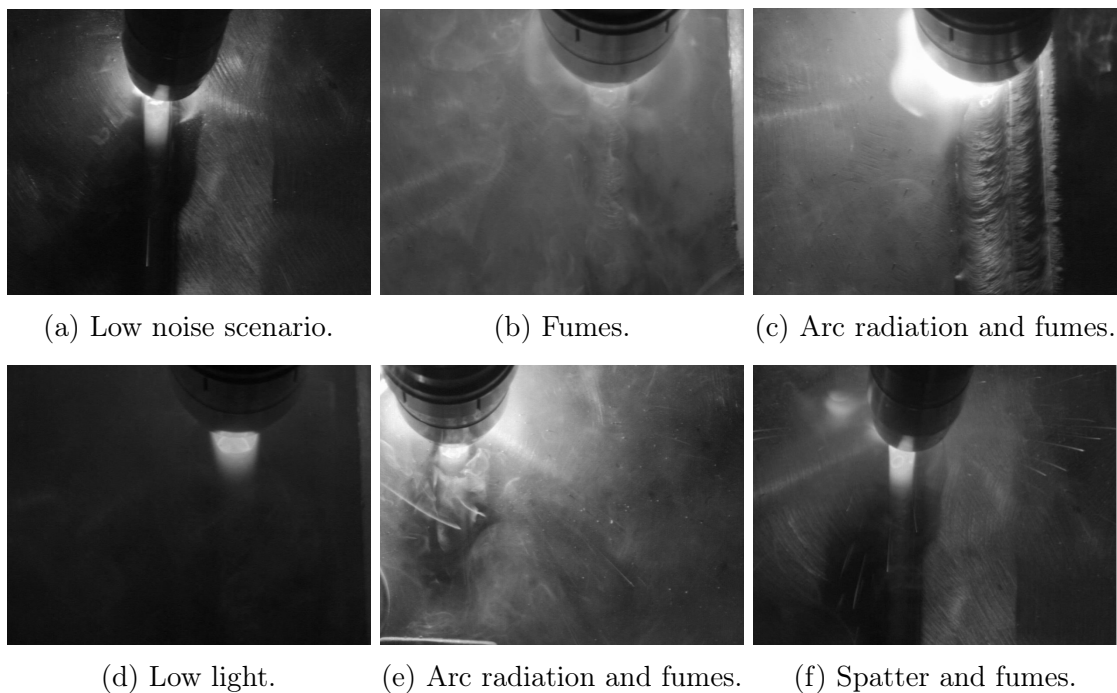


Figure 2.14: Captured frames during the monitoring and their different noises [17].

Chapter 3

Bead Geometry and Layer Design

In WAAM, it is crucial to find a relationship between the deposition parameters and the single bead geometry. Some approaches are based on different mathematical models to represent the bead geometry and correlate it with the input parameters. Simple continuous functions are used to model the bead cross-section profile in WAAM systems, for example, parabolas, sinusoids and circular arcs, but more advanced ones can also be used such as b-spline, logistic and Gaussian functions. Overall, it has been concluded that the bead profile is largely dependent on the wire feed speed (WFS) and the travel speed (TS) [5, 22].

The knowledge of the bead geometry model is very important for an intelligent additive manufacturing system. It can be used to develop feedback control algorithms, improve surface quality and perform cost management during the build-up. The development of a simple model for the bead geometry during deposition have its benefits, e.g.: *(i)* make easier to understand the behavior and to troubleshoot problem of the proposed model; *(ii)* a simpler control algorithm to be implemented during the buildup process.

The focus of this chapter is to identify a single-bead and multi-bead model. They can be used for simulating, testing and other applications like: *(i)* measuring comparison; *(ii)* filter development; *(iii)* calibration and testing of sensors; *(iv)* to achieve indirect deposition parameters. To have Multi-bead overlapping model is also very important due to its direct relation to the surface quality, part precision, and also in the presence of discontinuities or defects.

In WAAM a layer is build by moving the torch in a predefined path planing trajectory [59]. The goal is to fill the path with deposited material creating a 2.5D structure. It is called 2.5D because the path executed by the torch will generate a layer with a height. Since the current layer will always be deposited over the previous layer, it is easy to picture the importance of the surface quality of each layer in respect to the final layer surface quality since a low surface quality propagates between layers.

As stated before, to have a plain surface is important at the end of each layer, the flatter the surface the better it is for WAAM. High roughness, waviness, and poor finishing during layers deposition can cause the following problems and unwanted necessities in the printed part [29, 38]:

- More machining time;
- Increase of waste material;
- Low efficiency;
- Internal voids between layers.

Therefore quality management during additive manufacturing is very important. Some parameters to monitor and control are the bead width and the overlapping distance of the adjacent beads, the control of this distance decreases the chance of defect and improve quality and precision of final product minimizing the probability of a low surface finish.

3.1 Single-bead model

Single-bead model knowledge and its relation to the chosen IDP is essential for understanding the overall influence of these parameters with the geometry of the bead. One of the key aspects of developing WAAM technique is becoming capable of knowing which parameter directly influence on the deposition rate and the desired bead geometry. A schematic of the bead profile can be seen in Figure 3.1 with its main geometric characteristics (width, height and penetration) considered during parameter design phase. The monitoring of these characteristics is very important for an intelligent WAAM system. For example, with the usage of a suitable camera facing directly the substrate and fixed parallel to the torch, it is possible to extract the width along the material deposition. Other cameras assembly configuration also enable the extraction of features and measurements of others characteristics during the deposition.

Acquiring information about the bead width being deposited can be considered one of the most important variables of the bead geometry, since its undesired variations during buildup directly influences the quality of the layer. A constant bead width results in lesser waste of material and in a better deposition fitness and finish [19].

AIYITI *et al.* [1], stated that the cross-section profile of the bead is mainly dependent of WFS (Wire Feed Speed), travel speed and others parameters. He used

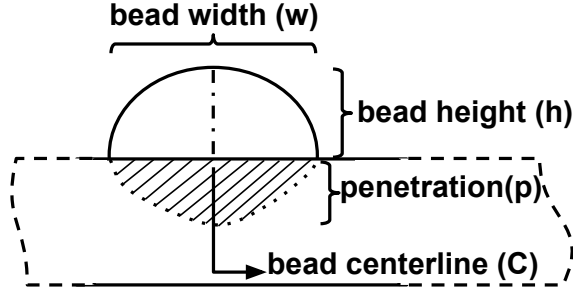


Figure 3.1: Cross-section profile of the single bead [17].

lambda (λ) to represent the relation between width(w) and height(h), calling it the thickness relation (Equation 3.1):

$$\lambda = \frac{w}{h} \quad (3.1)$$

With that relation, he established the bead cross-section profile with lambda values. For values of λ above 2, the cross-section will have an arc profile. However, it will be demonstrated that a parabola profile shows better fitting to the real bead profile for the parameter configuration usually used in WAAM.

In SURYAKUMAR *et al.* [59], the parameters are grouped according with its interdependence relation for hybrid layer manufacturing. That is, when a parameter vary another changes in cascade to maintain the arc stability. Within this characteristics the considered IDP that causes changes in the bead are:

- Wire diameter (w_d)
- Wire feed speed (WFS) (w_s)
- Torch speed or travel speed (t_s)
- The distance between neighbor beads (step-over distance) (d)

The model used for single bead is a symmetric parabola of the form $y = a + cx^2$, the terms a and c are represented as the welding bead height(h) and width(w), as follows:

$$a = h \quad \text{and} \quad c = -\frac{4h}{w^2}$$

Geometric model of the parabola:

$$y = h \left[1 - \left(\frac{2}{w} x \right)^2 \right] \quad (3.2)$$

The previous expression in terms of the deposition process parameters is described by 3.3, where v_w is the wire feed speed and v_t the torch speed.

$$y = h \left[1 - \left(\frac{16 h v_t}{3 \pi v_w d_w^2} x \right)^2 \right] \quad (3.3)$$

The bead formation by wire melting are affected by several physical phenomena. Although w and h are only affected by the welding parameters, it would be necessary to take into account several variables like gravity, viscosity, surface tension, electromagnetism and others to model their relation. So using equation 3.3 is more useful and satisfies many possible implementation with a simpler but reliable model [59]. Overall, it has been concluded that the bead profile is largely dependent of the wire feed rate and the travel speed [22].

The focus of XIONG *et al.* [68] is to fit the bead profile according to three models: A parabola, a circular arc and a cosine function with its curves passing through the point $B(w/2, 0)$ and $C(0, h)$ as detailed in Figure 3.2. The following assumptions are considered:

1. Symmetry of cross-section profile.
2. Deposition with the same parameter set has uniform cross-section.
3. Section profile of single-beads remaining unchanged at multi-bead application.

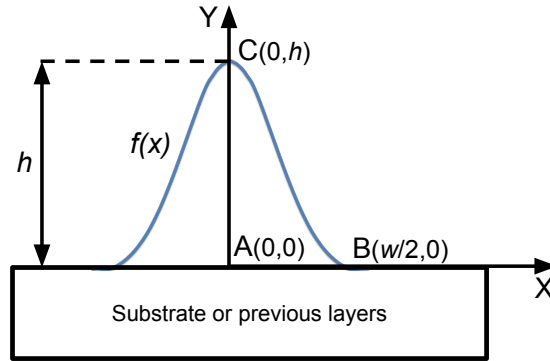


Figure 3.2: Single-bead cross-section model for the proposed models. Adapted from XIONG *et al.* [68].

A relation between each model and welding or deposition parameters is attempted obtaining the right prediction model to be used during deposition. Where the following curves of the formulation passes through points $B(w/2, 0)$ and $C(0, h)$ [68].

- Parabola model expression:

$$y = -\frac{4h}{w^2} x^2 + h \quad (3.4)$$

Profile area:

$$A_p = \int_{-\frac{w}{2}}^{\frac{w}{2}} h \cos\left(\frac{\pi x}{w}\right) dx = \frac{2 w h}{3} \quad (3.5)$$

- Cosine model expression:

$$y = h \cos(\pi x/w) \quad (3.6)$$

Profile area:

$$A_c = \int_{-\frac{w}{2}}^{\frac{w}{2}} h \cos\left(\frac{\pi x}{w}\right) dx = \frac{2 w h}{\pi} \quad (3.7)$$

- Arc model expression:

$$R = \frac{(h^2 + w^2/4)}{2h} \quad (3.8)$$

$$y = \sqrt{R^2 - x^2} + h - R \quad (3.9)$$

Profile area:

$$\begin{aligned} A_a &= \int_{-\frac{w}{2}}^{\frac{w}{2}} (\sqrt{R^2 - x^2} + h - R) dx \quad (3.10) \\ &= R^2 \arcsin \frac{w}{2R} + \frac{w \sqrt{R^2 - w^2/4}}{2} + w(h - R) \end{aligned}$$

Equation 3.11 express the cross-section profile based on the deposition parameters, when a 100% efficiency is considered, that is no material loss during the deposition process. Where w_s is the wire feed speed, w_d is the diameter of the wire and t_s is the travel speed.

$$A_m = \pi \frac{w_s w_d^2}{4 t_s} \quad (3.11)$$

The accuracy of the model proposed is analyzed using the Equation 3.12, that is used to calculate the difference between the cross-section area of the prediction bead model and the actual bead. Where, the first element is the area predicted by the model and the second is the real area of the bead cross-section.

$$ER_n = \frac{|A_{predicted(n)} - A_{measured(n)}|}{A_{actual(n)}} \times 100\% \quad (3.12)$$

The experiment index in the equation is represented by the letter **n**. Since the bead cross-section geometry is largely influenced by the magnitude of the wire feed speed to travel speed ratio (WFSTR), it is used to choose which prediction model is more adequate for a given 3D print scenario. Unfortunately, the models achieved still have a consider error and for high surface quality requirements it do not fit its purpose.

DING *et al.* [22], also used three popular mathematic functions, just like the

previous proposed model by XIONG *et al.* [68]. The authors focused in decreasing the error to achieve a more accurate prediction model, which in some cases the error are as high as 15 – 20 % in the previous works. The expressions used are detailed at Table 3.1, where the a , b , and c parameters must be identified through experimental measurements.

Table 3.1: Equations of common bead profile models [22].

Model	Bead height(h)	Bead width(w)	Bead area
Parabola	c	$2\sqrt{-\frac{c}{a}}$	$A_p = \frac{4c}{3}\sqrt{\frac{-c}{a}}$
Cosine	a	$\frac{\pi}{b}$	$A_c = \frac{2a}{b}$
Arc	$a - b$	$2\sqrt{a^2 - b^2}$	$A_a = \arccos \frac{-b}{a} - b\sqrt{a^2 - b^2}$

The relation between the wire feed speed and the travel speed is represented by the variable lambda (λ). The wire feed speed is kept constant and a variation range from (200 – 550) mm/min is set for the travel speed. This is linked with the best profile model based on relative error analysis, and laser scanner with a 0.02 mm accuracy is used to measure the specimens profiles [22]. The Lambda parameter is also used as input to be decide which model is the best fit for a specific job.

In the experiments performed by DING *et al.* [22], the area error is less than 4% when comparing the prediction to the actual for all proposed model. The material loss is not considered and the same assumptions as the ones from XIONG *et al.* [68] are taken. The parabola model present a lower error when compared with the others and better fit the beads deposited. Therefore, the ideal model can be used for a multi-bead study.

The cross-section bead profile can be seen in Fig.3.1 with its main characteristics, wherein by using a suitable camera assembled in a specific configuration, e.g. facing the substrate is only possible to extract the width and the centerline while printing.

3.2 Multi-bead model

WAAM build-up a part by depositing multiple adjacent single-beads forming a layer. Therefore, the relation between these single beads is important and directly influences the quality of the surface and the part produced. The intersection area resulted from the deposition of single beads is called overlapping area and has a important role in surface quality and smoothness. A generic model of multi-bead is described at Figure 3.3, where some important characteristics are highlighted, the distance between adjacent beads centerline also known as step-over distance.

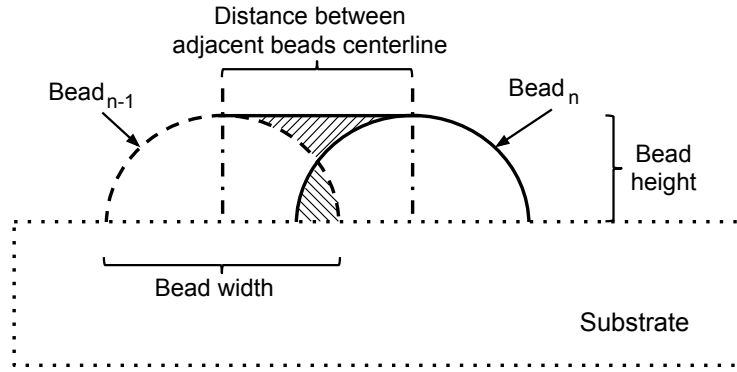


Figure 3.3: Generic multi-bead example [17].

According with XIONG *et al.* [68], some studies performed by e.g. AIYITI *et al.* [1], CHAN *et al.* [6], and CAO *et al.* [5] propose a multi-bead model which details the overlapping distance, however they are not fit due to the lack of the verification step. This model is used to define the overlapping distance between adjacent beads.

3.2.1 Surface layer quality

It is possible to see in Figure 3.4 the deposition of adjacent beads forming a layer. Usually, to produce the final part, many layers need to be stacked. So, the current layer will always be deposited on the surface of the previous. This emphasizes the necessity to monitor the deposition characteristics that affects the layer surface quality.

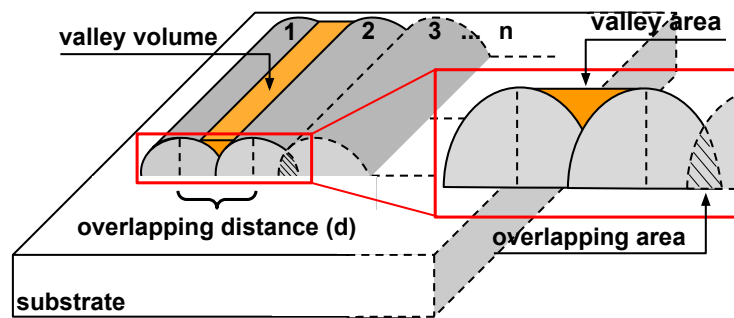


Figure 3.4: Multi-bead deposition example in WAAM [17].

Surface quality can be considered how smooth and flat is the surface of each layer. In multi-sided beads scenario (Fig.3.4), the cross-section overlapped area between adjacent single passes has great influence on the surface quality and dimension accuracy [68].

3.2.2 Overlapping model

Two overlapping models have been used to show the interaction of beads and ensure a better surface quality in a multi-bead deposition process: the flat overlapping model (FOM) [68] and tangent overlapping model (TOM) [22]. A comparison between both models for a stack of five layers is performed by DING *et al.* [22]. Both models propose an optimal distance between the centerline of each adjacent bead, also named overlapping distance (d), based on a linear relation between d and w .

The overlapping model plays an important role on the surface quality, the overlapping between adjacent beads begins when the step-over distance (d) becomes smaller than w . Step-over distance is also called overlapping distance, as this distance decreases the overlapping area grows reaching an ideal distance, the interval used to analyze is from w to $w/2$. The flat and the tangent overlapping model (TOM and FOM) propose an optimum value for the distance between the centerline (c) of adjacent beads. These models are described in Figure 3.5 and Figure 3.6, in both cases, d is specified to make the overlapping area between both beads be equal to the valley area.

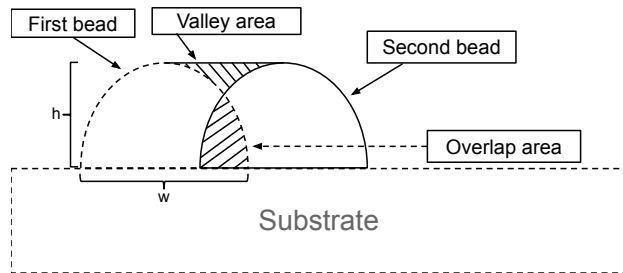


Figure 3.5: Flat overlapping model (FOM) for multi-bead deposition, adapted from XIONG *et al.* [68].

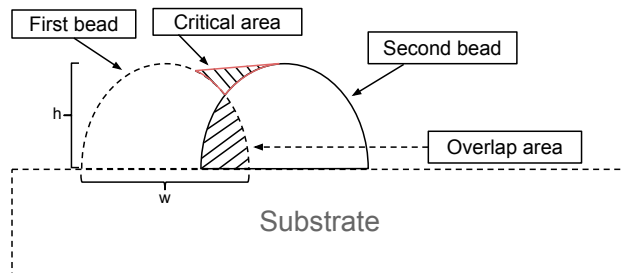


Figure 3.6: Tangent overlapping model (TOM) for multi-bead deposition, adapted from DING *et al.* [22].

XIONG *et al.* [68] conducted a study about the influence of the overlapping distance (d) on the surface quality, and concluded that a flat layer surface is achieved when valley area is equal to the overlapping area, with the usage of an ideal step-over distance. The authors propose that the optimal distance between adjacent

beads have a direct relation with the bead width (w) and is ruled by the linear equation: $d = 0.667w$. DING *et al.* [22] also propose an optimum step-over distance ($d = 0.738w$) and compared the result of the layer surface using both models. In Figure 3.7, the result of the comparison is described. When compared to the TOM result (Figure 3.7b), the FOM presents a lower geometric accuracy but achieved a lower waviness.

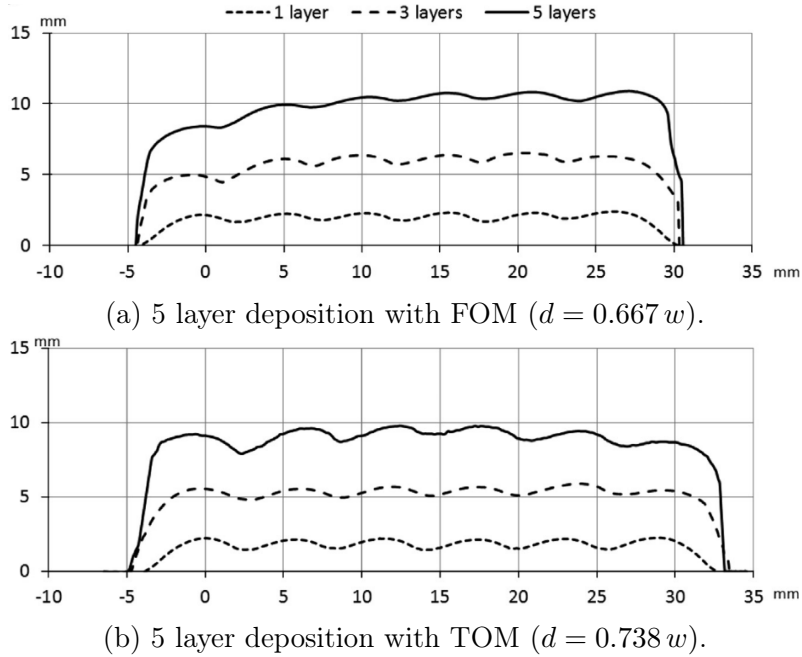


Figure 3.7: Multi-bead experiment with a 5 layers deposition used to verify the surface quality with tangent and flat overlapping models [22].

It is possible to see in Figure 3.8 how the step-over distance influence the quality of the surface as well as the geometry accuracy of the part. So, the overlapped area must be equal to the area of the valley for achieving adequate results. In Figure 3.8.c it is shown the ideal layer finish based on the optimum distance (d^*) between the bead centers proposed by FOM and TOM models.

It is possible to conclude that the bead width tracking is very important for high-quality additive manufacturing system, due to the fact that its layer surface finish is directly related to the ideal overlapping distance which is directly related to the bead width. Therefore, to measure this characteristic improves the capability of ensuring the quality and accuracy of the deposition process.

3.3 Wire feeding impact on layer quality

For WAAM, the wire feeding pose (position and orientation) has a critical role to manufacture a part with a stable deposition process and high layer surface quality. This is specially important for independent wire feed system which the wire is fed

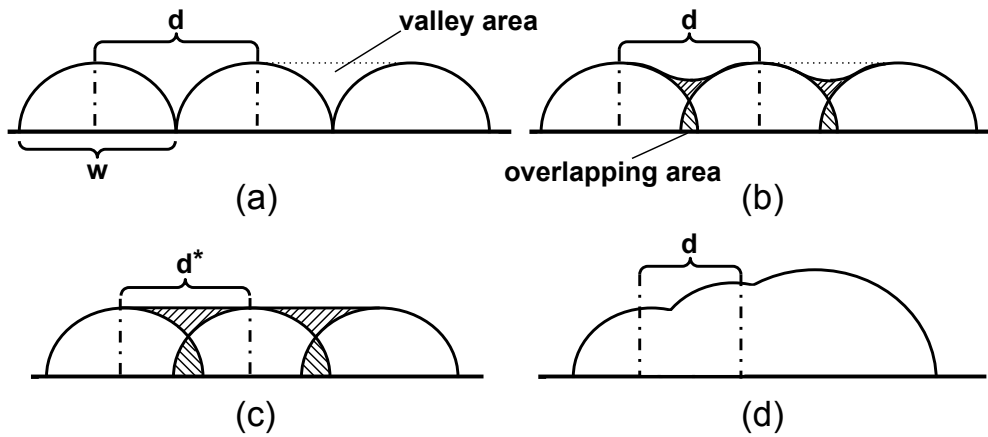


Figure 3.8: Influence of the overlapping area on the layers surface quality; (a) $d \geq w$, when there is no overlapping, (b) $d < w$, when the overlapping area is smaller than the total valley area, (c) $d = d^*$, when the overlapping area is equal to the valley area resulting in a theoretically flat surface, and (d) $d < d^*$, when the overlapping area is bigger than the valley area [17].

from the rear, side, or front of the molten pool, like GTAW and PAW [76]. Design a wire feeding strategy is one of the possibilities to minimize the occurrence of defects during manufacturing using these processes. However, the feeding position is usually kept in a unchanged configuration with fixed angle and position [37].

GENG *et al.* [37] performed a study about the influence of the wire tip distance (height) to the electrode and the wire feeding angle with GTAW show the impact in the material deposition starting point and surface quality with the wire configured in a front feed of the travel direction. The assembly is described in Figure 3.9a and the parameters considered in Figure 3.9b.

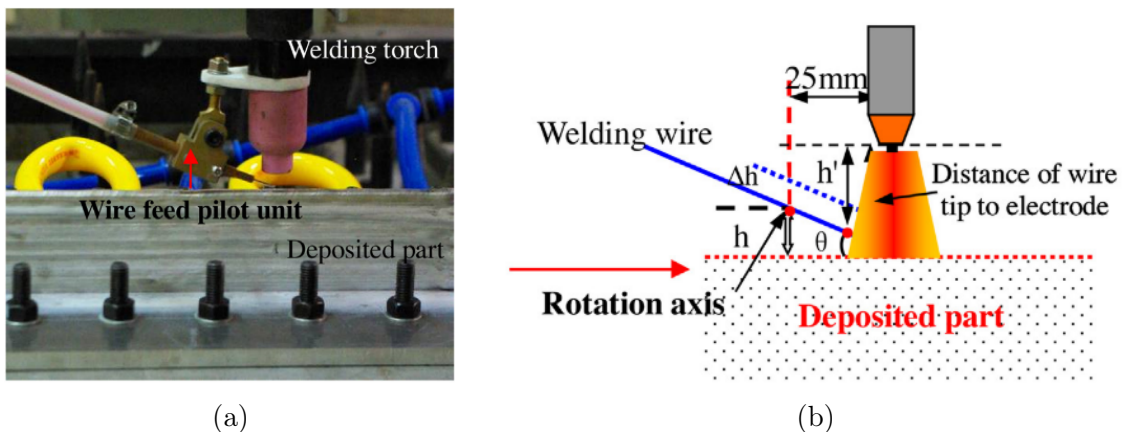


Figure 3.9: Wire feeding configuration (e.g. PAW) (a) and parameters (b) for front feeding assembly [37].

The experiment is divided in two steps: (1) the influence of the angle variation in deposition start position; (2) the influence of the distance (height) of the wire tip to electrode in the deposition start position. The result is described in Figure 3.10,

where an influence in the deposition start point is noticed by varying the wire feeding angle (Figure 3.10a) and also in the feeding height using a fixed feeding angle of 15deg (Figure 3.10b). The influence in the height distance variation Δh also changes the transfer mode, which impacts the surface quality of the bead deposited as shown in Figure 3.11.

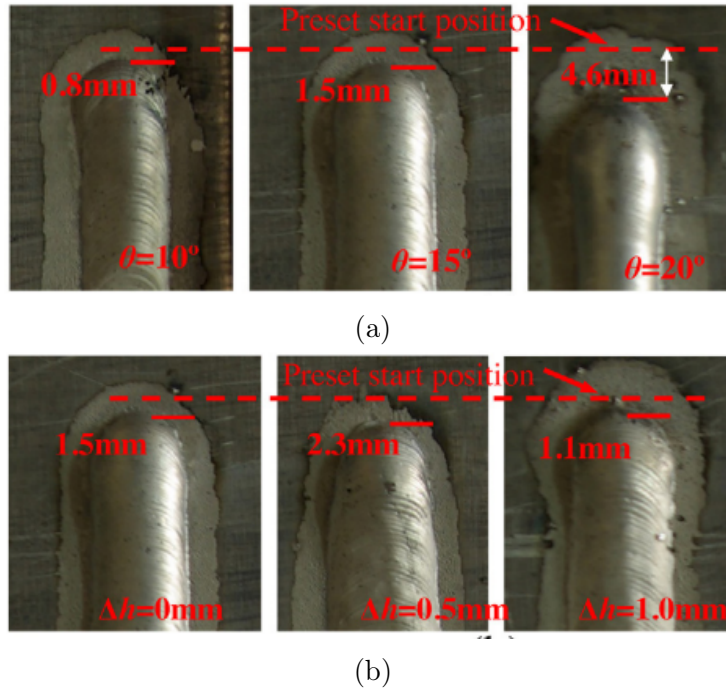


Figure 3.10: Effect on single beads position start and finishing varying its feeding angle (a) and height (b) [37].

When using a lower feeding angle and a higher Δh (distance variation of wire tip to molten pool surface), a tendency to decrease the deposition start point error is noted. However, keeping these parameters respectively lower or higher as possible also influence the layer quality (Figure 3.10). WU *et al.* [67] also varies the wire feeding angle from 50° to 70° to analyze its effect in the layer quality for WAAM with GTAW. In the experiment, an adequate result is obtained when feeding the wire with a angle of 60°. The usage of angles lower than 50° or higher than 70° result in a lower layer quality.

One of the aspects that also influence the layer quality is the wire feed orientation. There are mainly three option for feeding the wire: (i) front feeding; (ii) side feeding; (iii) and rear feeding (Figure 3.12). The optimal orientation to achieve a good surface quality has shown to be material dependent. Therefore, an optimal wire feeding position and orientation to print with a chosen material can be achieved through experiments [25].

In its manufacturing the wire is affected by tension stress, due this characteristics it may present certain curvature in its free state. This curvature can lead to

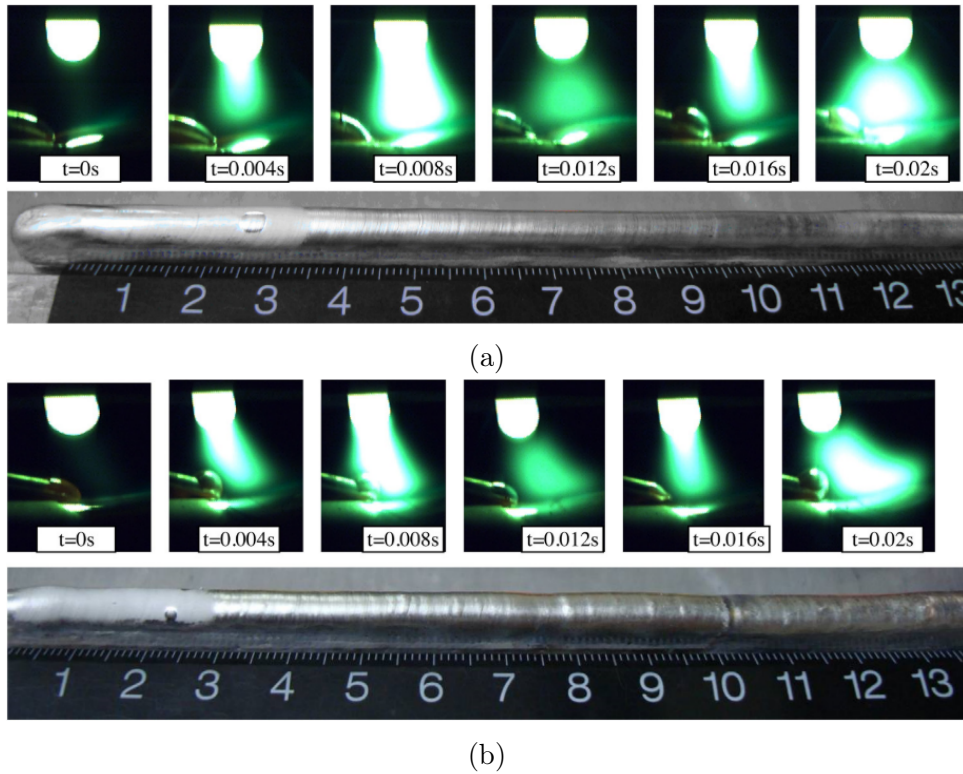


Figure 3.11: High-speed images for the bridge (a) and globular (b) transfer modes, where in (a) $\Delta h = 0$ and in (b) $\Delta h = 0.5$. The bead surface quality for each transfer mode is also affected at each transfer mode [37].

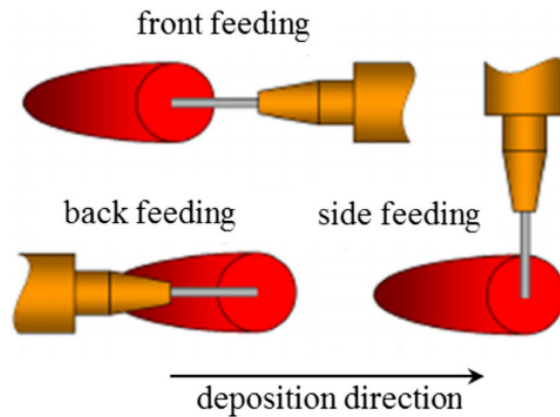


Figure 3.12: The three types of wire feed in relation to the deposition direction [25].

poor deposition quality, since a deviation in the wire tip can be perceived during deposition (Figure 3.13). A vision-based monitor system is developed to measure the wire tip position deviation [76]. The wire feeding is assembled in a front feeding configuration (Figure 3.12).

The experiment shows the possibility of measuring online the wire deviation in WAAM. The deviation angle is measured using the wire centerline and a normal line to the wire feeder nozzle. These characteristics are described in the following figure.

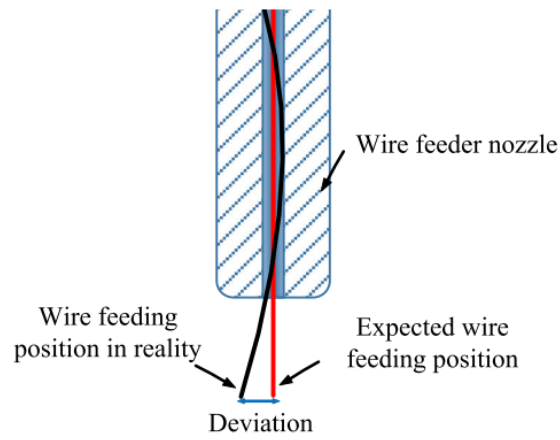


Figure 3.13: Wire feed deviation issue example when monitored with a single camera [76].

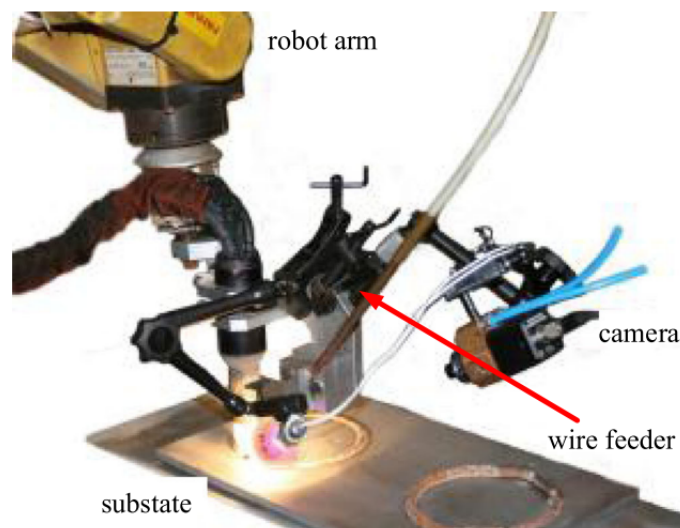


Figure 3.14: Equipment and camera setup to print [76].

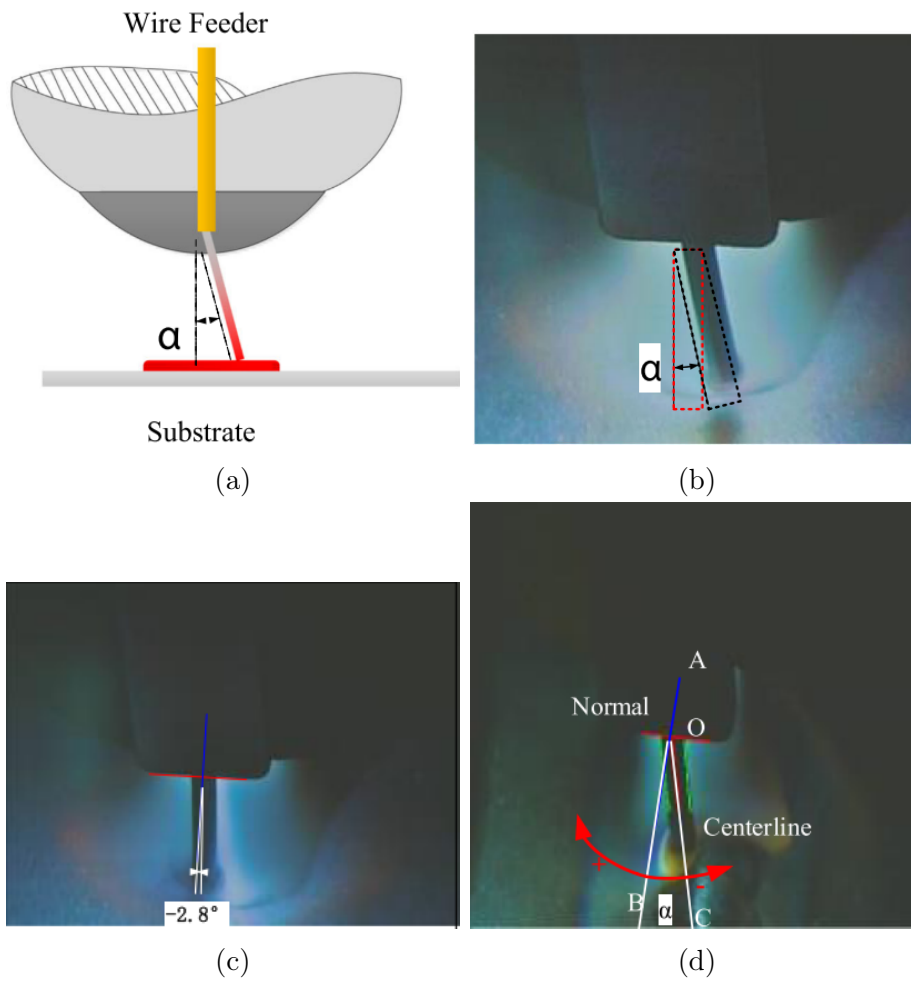


Figure 3.15: Wire deflection measuring with passive camera with the camera image view (a), deflection example (b and c), and the characteristics (nozzle normal line and wire centerline) used to measure the deviation (d) [76].

Chapter 4

Robotic, Controls and Computer Vision

This chapter introduces some of the robotics, controls and computer vision concepts used in the algorithm development and in the simulations performed inside Matlab, both with the focus on a proposed WAAM system. The passive vision sensors are used in this work to extract valuable information from the process during the print process, which are treated and then transmitted in a local network through the ROS framework. Therefore, to attenuate the noise and estimate the bead width and centerline position while depositing it is necessary to use the computed vision and robotics concepts introduced.

4.1 Robot manipulator kinematics

To print a part, the robotic WAAM cell usually has as one of its components a 6-DOF manipulator to guide the torch and reach all available operational space configuration. A robot arm (manipulator) is represented as a chain of rigid bodies (links) and joints (prismatic or revolute). Where one end of the system is the base and at the other the end-effector. It performs the deposition process with a set of planned position $p_e = [x \ y \ z]^T$ and orientation (pose) in respect to a chosen reference frame. To compute the required joint angles to fulfill a task in the operational space and also the pose of the end-effector for a joint angle set, the direct and inverse kinematics equations are used. In this work the orientation is represented as a set of three angles $\phi = [\varphi \ \vartheta \ \psi]^T$ named roll, pitch, and yaw and is named minimal representation. The pose of the end-effector 4.1 is described as a 6x1 dimension vector representation, where the first three are the end-effector position and the last 3 its orientation [57].

$$x_e = \begin{bmatrix} p_e \\ \phi \end{bmatrix} \quad (4.1)$$

4.1.1 Rotation matrix

A convenient way to express the orientation of a rigid body is to use three orthonormal unit vectors with respect to a reference frame. Let O be the reference frame and \mathbf{x} , \mathbf{y} , \mathbf{z} its frame axes unit vectors, the orientation of a rigid body frame O' in respect to O is expressed by 4.2, with x' , y' , z' being the rigid body frame unit vectors.

$$\begin{aligned} \mathbf{x}' &= x'_x \mathbf{x} + x'_y \mathbf{y} + x'_z \mathbf{z} \\ \mathbf{y}' &= y'_x \mathbf{x} + y'_y \mathbf{y} + y'_z \mathbf{z} \\ \mathbf{z}' &= z'_x \mathbf{x} + z'_y \mathbf{y} + z'_z \mathbf{z} \end{aligned} \quad (4.2)$$

A compact notation is used to represent the unit vectors 4.2, when combined into a 3x3 matrix, it is called a rotation matrix and represented as shown in Equation 4.3 [57].

$$\mathbf{R} = \begin{bmatrix} \mathbf{x}' & \mathbf{y}' & \mathbf{z}' \end{bmatrix} = \begin{bmatrix} x'_x & y'_x & z'_x \\ x'_y & y'_y & z'_y \\ z'_x & z'_y & z'_z \end{bmatrix} \quad (4.3)$$

The rotation matrix have the following properties: (i) The column vectors are mutually orthogonal; (ii) \mathbf{R} is a orthogonal matrix $R^T R = I_3$, where I_3 is the representation of the identity matrix; (iii) R^{-1} is equal to the transpose R^T ; (iv) The determinant is equal to 1 or -1 when represented in a right-handed or left-handed frame respectively.

4.1.2 Direct kinematic

Direct kinematics is the task of mapping from the manipulator joint configuration to the end-effector pose X_e , and inverse kinematics is the opposite, mapping from the end-effector pose to the robot arm joint configuration. To perform the part build-up through a predefined path, the robot arm is configured with a set of joint angles to reach each desired pose at the operational space. The direct kinematics from the robot arm base to the end-effector can be represented with the minimal representation 4.1 or with a homogeneous transformation matrix 4.4 [57]. Where R_{be} is the end-effector orientation represented by a rotation matrix and p_{be} is the position represented in relation to its base.

$$T_{be} = \begin{bmatrix} R_{be} & p_{be} \\ 0_{1 \times 3} & 1 \end{bmatrix} \quad (4.4)$$

Therefore with the knowledge of all robot arm joint angles and the tool used, the transformation from the base to the end-effector provides the position and orientation of the tool used during a task requested to the robot. These steps are graphically described in Figure 4.1, the red, green, and blue orthogonal vector in the base and end-effector frames represent x, y, and z.

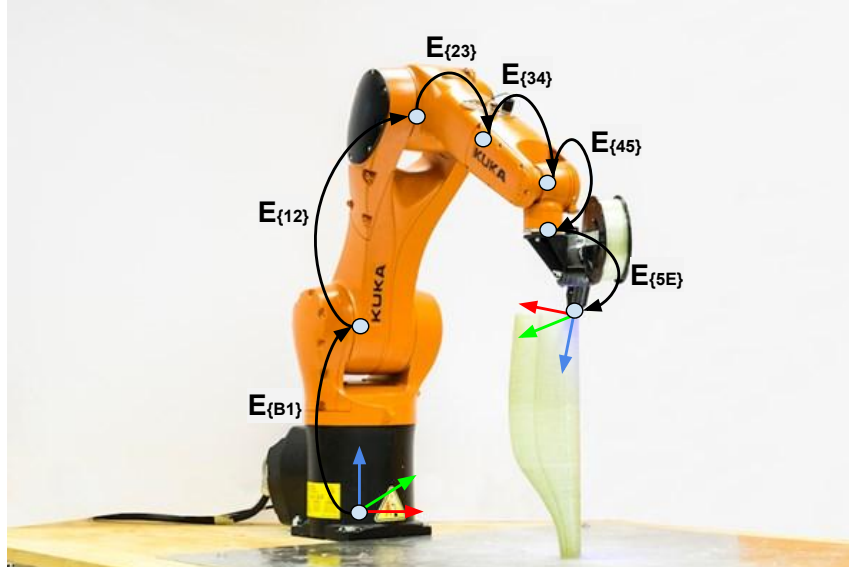


Figure 4.1: 6-DOF robot printing a glass fiber composites and the homogeneous transformation representation from its base to the end-effector. Retrieved and adapted from <https://www.compositesworld.com/articles/video-six-axis-robotic-arm-3d-printing-fiberglass-composites-03/25/2022>

4.1.3 Inverse kinematic

The inverse kinematics problem consists in determining the required joint angles to a given end-effector pose. This application is fundamental for instance in WAAM, where the deposition path and parameters like the travel speed are defined at the operational space using the minimal representation, which contains the desired position and orientation of the end-effector. So, the inverse kinematic equation 4.5 is used to calculate the required joint angles q for each the end-effector Cartesian pose x_e [16, 57].

$$q = K^{-1}(x_e) \quad (4.5)$$

4.2 Computer vision

Vision-based sensors are broadly used in WAAM because of their non-touching capability of monitoring the process, and also due to the possibility to estimate the process characteristics when using a proper sensor and vision-based algorithms as already presented in section 2. This information can be used to improve and ensure the quality of the part produced, to monitor possible discontinuities during the print, to provide feedback data to a controller, and other possible applications. Also, the spatial filters presented are used to attenuate the noise present during a deposition process with WAAM, and the feature detection algorithm to extract the desired information from the image which will be used for the bead position and width estimation. Figure 4.2 details the steps used from the image acquisition to the measurement of the desired characteristics of the process.

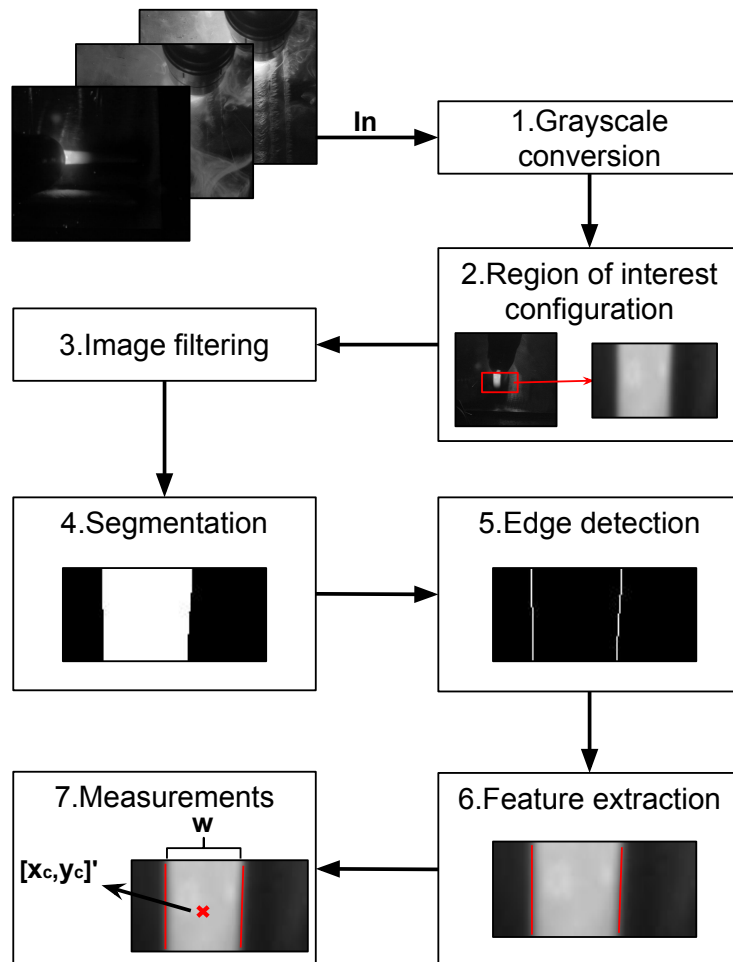


Figure 4.2: Stages used in the vision-based algorithm [17].

4.2.1 Camera model

The process of image formation in an eye or in a camera, involves a projection operation from the 3D world onto a 2D surface. Therefore, one dimension (depth) is lost in the projection operation, and it is not possible to from an image whether the object closer in the image is larger or smaller than another farther in the image without a reliable and know reference in the image for example. This transformation from 3D to 2D is known as perspective projection, and it is detailed in this section. In the current work the camera model used is the pin-hole. One the important characteristic of the pin-hole camera is that is has no focus adjustment, therefore, all information observed in its field of view are considered in focus irrespective of distance [16].

Perspective projection

A small hole in a surface acts similar to a convex lens to form an image. The fundamental geometry of the image formation for thin lens is described in Figure 4.3

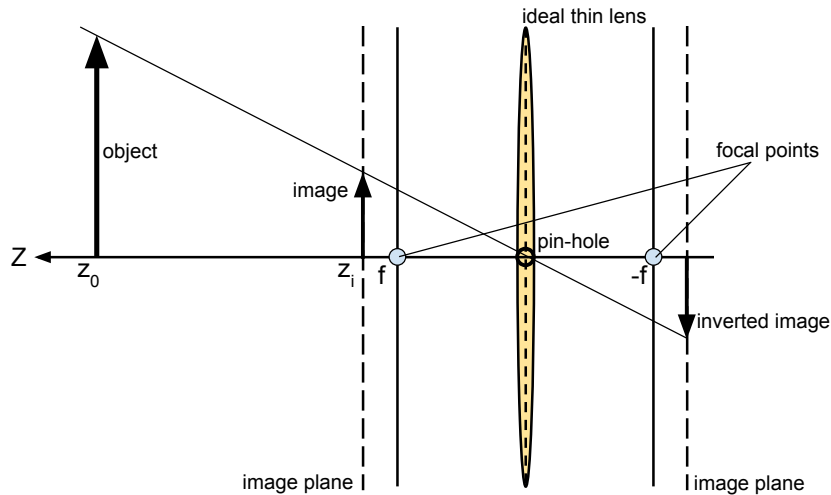


Figure 4.3: Image formation geometry for thin convex lens and a pin-hole. Adapted from [16]

The positive Z -axis is aligned with the camera optical axis. Where the z -coordinate of the object and its image is given by their distance to the camera lens center, this relation is given by Equation 4.6. Where, z_0 is the distance from the lens to the object, z_i is the distance to the image, and f is the focal length of the lens.

$$\frac{1}{z_0} + \frac{1}{z_i} = \frac{1}{f} \quad (4.6)$$

In computer vision it is common to use the central perspective imaging model.

The rays converge on the origin of the camera frame C and a non-inverted image is projected onto the image plane located at $z = f$ as shown in Figure 4.4. A point at the world coordinate $P = (X, Y, Z)$ is projected to the image point $p = (x, y)$ by 4.7. Where both coordinates are represented as *Euclidean* coordinates.

$$x = f \frac{X}{Z}, \quad y = f \frac{Y}{Z} \quad (4.7)$$

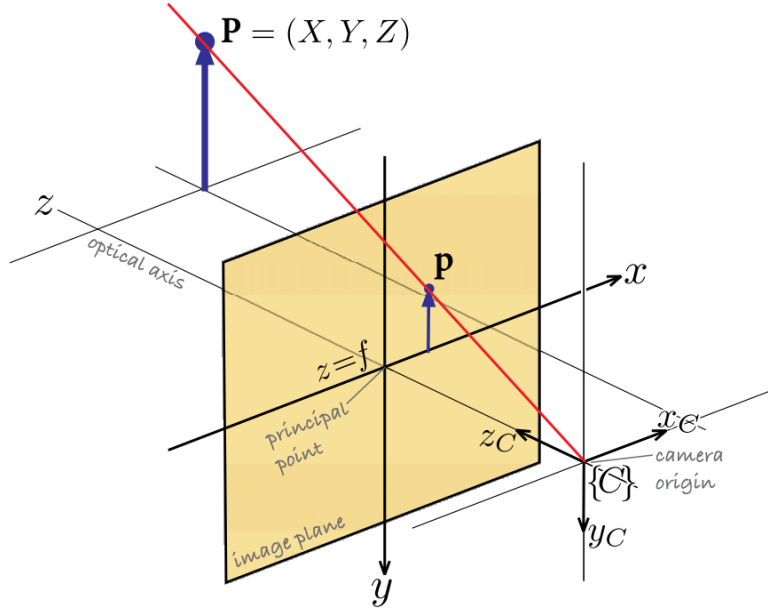


Figure 4.4: Central-projection camera model, with the image plane located at the lens positive optical length f in front of the camera origin [16].

Perspective camera model

To perform the transformations, the point coordinate must be represented in the homogeneous form $\tilde{p} = (\tilde{x}, \tilde{y}, \tilde{z})$. Where,

$$\tilde{x} = fX, \quad \tilde{y} = fY, \quad \tilde{z} = Z \quad (4.8)$$

or in the matrix compact form:

$$\tilde{p} = \begin{bmatrix} f & 0 & 0 \\ 0 & f & 0 \\ 0 & 0 & 1 \end{bmatrix} \begin{bmatrix} X \\ Y \\ Z \end{bmatrix} \quad (4.9)$$

The non-homogeneous coordinate $p = (x, y) = (u, v)$ are given by 4.10.

$$x = \frac{\tilde{x}}{\tilde{z}}, \quad y = \frac{\tilde{y}}{\tilde{z}} \quad (4.10)$$

If the world coordinate is written in homogeneous form, $\tilde{P} = (X, Y, Z, 1)$, then the perspective projection can be described in a linear form as 4.11.

$$\tilde{p} = \begin{bmatrix} f & 0 & 0 & 0 \\ 0 & f & 0 & 0 \\ 0 & 0 & 1 & 0 \end{bmatrix} \tilde{P}_C \Rightarrow \tilde{p} = C \tilde{P}_C \quad (4.11)$$

Where C is the camera matrix, and the term \tilde{P}_C represents the point in homogeneous form in reference to the camera frame, and \tilde{p} is the point representation (u, v) at the image plane. Therefore, when the camera pose is not equal to the inertial coordinate system, an inverse homogeneous transform must be used to discover the point reference to the new camera pose, as described in 4.12 [16]. An example of is shown at Figure 4.5.

$$\tilde{P}_C = T_C^{-1} P \quad (4.12)$$

Therefore, the point representation at the image plane \tilde{p} in homogeneous representation is given by 4.13, and in the image plane it is represented as 4.10.

$$\tilde{p} = C T_C^{-1} P \quad (4.13)$$

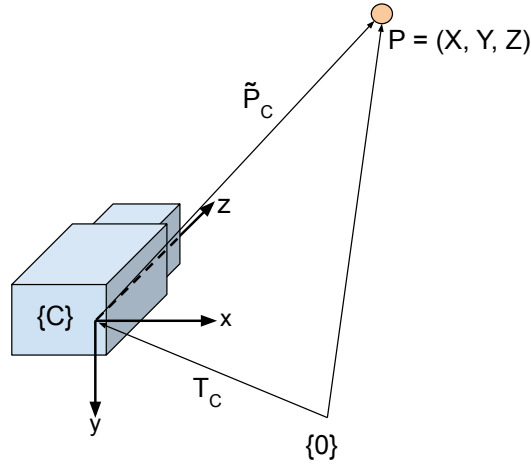


Figure 4.5: Point identified in reference to the camera and the world coordinate system. Adapted from CORKE [16].

Since the projection operator does not allow inverse, to find the inertial coordinate of a point based on its coordinates at the image plane it is not possible. Additional information must be known to perform the inverse operation, they are: (i) The distance of the camera to the observed point; (ii) The camera pose. The conversion is performed by the steps described in the Equation 4.14 to 4.15 where all the points are computed in the homogeneous coordinate ($\tilde{p} = [\tilde{x} \ \tilde{y} \ \tilde{z}]^T$), Figure 4.5

is also used as reference. With the distance from the camera to the point known, the point of the image plane is represented in homogeneous form at the camera reference frame as P_C . And then, the point representation to the inertial frame is computed using the homogeneous representation of the camera pose T_C and P_C .

$$P_C = C^{-1} \tilde{p} \quad (4.14)$$

$$P = T_C P_C \quad (4.15)$$

Discrete image plane and the camera matrix

In a digital camera, the image plane is represented by a $W \times H$ grid pixels, and the pixel coordinate are a 2D vector (u, v) of non-negative integers and its origin is at the top left, check Figure 4.8.

The camera projection matrix in its general form for a digital camera is represented at Figure 4.6, and the camera parameter matrix is composed by the intrinsic parameters which are innate characteristics of the camera and the sensor. Where ρ_w and ρ_h are the pixel width and height, f the focal length, u_0 and v_0 are the principal points, and the extrinsic parameters the representation of the camera case with a minimum of 6 parameters [16].

$$\tilde{p} = \underbrace{\begin{bmatrix} f/\rho_w & 0 & u_0 \\ 0 & f/\rho_h & v_0 \\ 0 & 0 & 1 \end{bmatrix}}_{\text{intrinsic}} \underbrace{\begin{bmatrix} 1 & 0 & 0 & 0 \\ 0 & 1 & 0 & 0 \\ 0 & 0 & 1 & 0 \end{bmatrix}}_{\text{extrinsic}} T_C^{-1} P$$

Figure 4.6: Camera projection matrix with the intrinsic and extrinsic parameters for digital images.

4.2.2 Spatial filtering for vision sensors

Usually, after acquiring data through a passive vision-based monitoring system, the first action performed in order to reduce the noise to extract the desired features is the filtering step. Figure 4.7 describes these noises when a deposition in WAAM is performed using CMT. Since they are intrinsic of the chosen deposition process, physical and digital filtering solutions must be developed to improve the quality of the data acquired during the monitoring. Therefore, the current work is also focused in testing and developing digital filters applied to this application.

Spatial domain filters operates directly on the pixel of an image, and generally are computationally efficient and require less processing resources to implement.

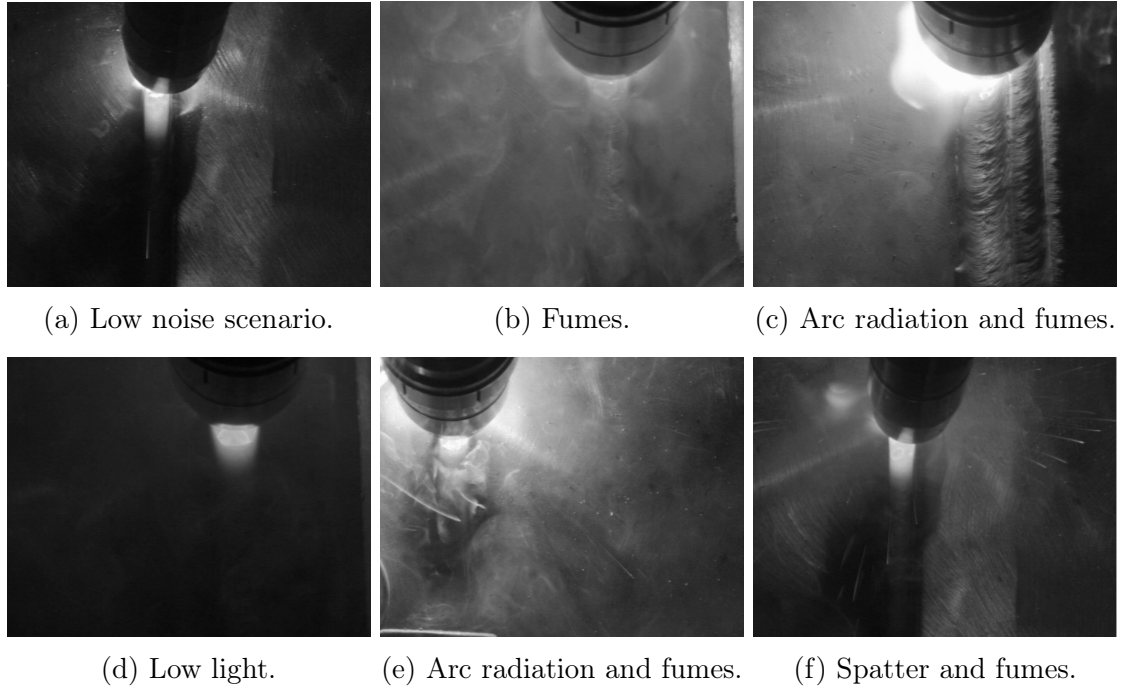


Figure 4.7: Captured frames during the monitoring and their different noises [17].

They can be denoted by the expression,

$$g(x, y) = T[f(x, y)] \quad (4.16)$$

where $f(x)$ is the input image, $g(x, y)$ is the output image, and T is an operator applied over a neighborhood of a point (x, y) . The operator can be applied in a single image or to a set of images for noise reduction. They are considered also versatile filters, since they can be used for nonlinear filtering, something that sometimes are not possible to do with frequency domain filters. Figure 4.8 describes the operation with a 3×3 kernel operator T , which will be referred as kernel during the text, at a target image f . The output image g has the same dimension and the input image f , where the filtering result of each position (x, y) will have the same coordinate in the new image generated. It is important to highlight that the size of the kernel operator changes for each application, and its optimal dimension must be achieved through testing.

4.2.3 Correlation and convolution

There are two concepts used when performing linear spatial filtering, one is correlation and the other is convolution. Correlation is the process of moving a filter kernel over the whole image and computing its transform for each pixel, as briefly detailed before. Convolution uses the same mechanics, however, with the filter rotated by 180° .

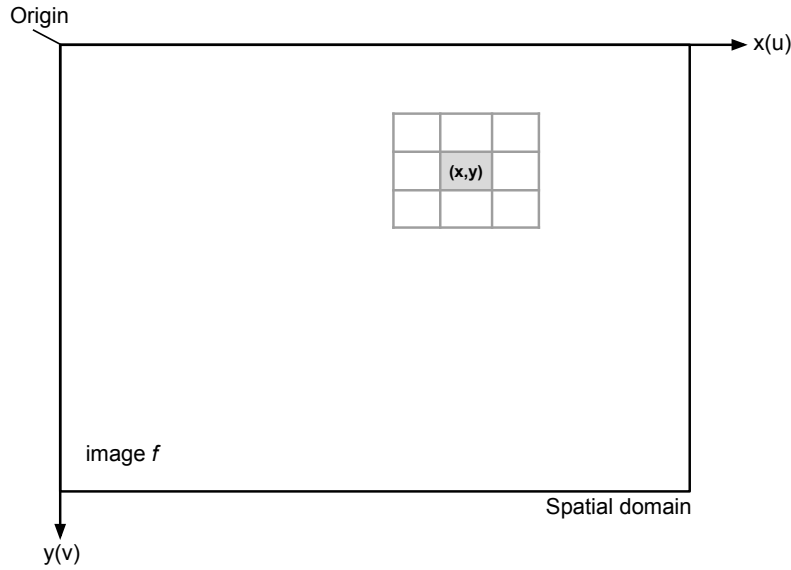


Figure 4.8: A 3×3 kernel operator T applied to an image f in the spatial domain. Where the output image g is the result of T correlated in f . Adapted from GONZALEZ e WOODS [39].

Two important points must be noted about correlation: (i) it is a displacement function; (ii) correlating a filter w with a function that contains all 0s and a single 1 results in a copy of w , but rotate by 180° . A fundamental property of convolution is that when performed into a function it results in a copy of the function. Therefore, as the filter is pre-rotated and the same operation from correlation is performed, it is possible to obtain the desired result. The procedures of correlation and convolution of a filter $w(x, y)$ of size $m \times n$ in a given image $f(x, y)$ are summarized by the expressions 4.17 and 4.18 respectively.

$$w(x, y) \square f(x, y) = \sum_{s=-a}^a \sum_{t=-b}^b w(s, t) f(x + s, y + t) \quad (4.17)$$

$$w(x, y) \blacksquare f(x, y) = \sum_{s=-a}^a \sum_{t=-b}^b w(s, t) f(x - s, y - t) \quad (4.18)$$

Where $a = (m - 1)/2$ and $b = (n - 1)/2$, and it is assumed that m and n are odd integers.

4.2.4 Smoothing linear filters

One of the first steps present in the vision-based algorithm, is the step of reducing the noise of a acquired data. This is performed through the usage of smoothing

filters, that are used for blurring and for noise reduction. The noise reduction can be accomplished by blurring the image with linear filters and nonlinear filters. The idea of these filters is to replace the value of each pixel, e.g. for the average of a neighborhood defined by a chosen kernel, which reduce "sharp" intensity transition in an image, since random noises typically are present in these intensity sharp transitions. One downside of the smoothing filters, is that is can affect some desired features of the image, like edges, they consist of sharp intensity transitions. Therefore, its kernel dimension must be considered to avoid affecting the quality of the desired features. Two examples of smoothing filters kernels are shown in Figure 4.9, where the first calculates the mean of a region attributing the same weight to all pixels and the second have a higher weight to some pixels given their higher importance. The basic strategy of weighting the center pixel as the highest is to attempt to reduce the blurring effect. The general implementation of for filtering an $M \times N$ image with weighted averaging filter of size $m \times n$ is given by the expression 4.19 [39].

$$g(x, y) = \frac{\sum_{s=-a}^a \sum_{t=-b}^b w(s, t) f(x + s, y + t)}{\sum_{s=-a}^a \sum_{t=-b}^b w(s, t)} \quad (4.19)$$

The size of the kernel used directly impact the sharpness of the output image g , therefore, it must be carefully defined to avoid losing the desired features in the data. An example of how the dimension of the smooth filter kernel impact the output image is detailed in Figure 4.10.

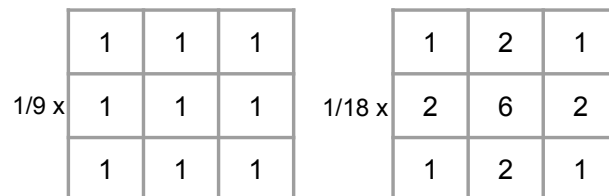


Figure 4.9: Two kernels used in the smoothing process are represented. The left kernel result needs to be divided by 9 and the right by 18, which is the sum of all the kernel position data.

Order-Statistic (nonlinear) filters

Order-statistic filters are nonlinear spatial filters, their response is based on ranking the pixels of an image by encompassing a filter, and then replacing the value of the centered pixel with the one determined by the operation. The best-know filter in this category is the median filter.

The Median Filter is considered a non-linear filter, the output is the computation of every entry median considering a defined area or quantity of values around the

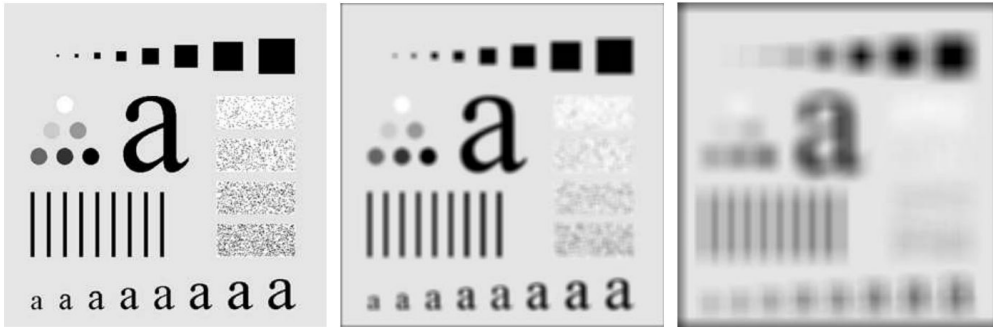


Figure 4.10: Impact of the kernel size at the output image (from left to right): (i) original image; (ii) output image after an smoothing operation with a 9x9 kernel; (iii) output image after an smoothing operation with a 35x35 kernel. Adapted from GONZALEZ e WOODS [39].

chosen entry. Extreme data that can be related to impulse noises wont appear in the output result of a median filter, being a good choice for treating noises in images. It is particularly effective against the presence of impulse noise, also called salt-and-pepper noise. The principal function of median filters is to force points with distinct intensity level to be more like their neighbors, based on the median value of the result of each pixel operated by a kernel. Careful analysis must carried out before the using median filter, e.g. if the image acquired already has low quality, the result of the median filter wont be satisfactory since it can degrade even more the quality of the data [7, 39].

Gaussian spatial filter

To generate the output filtered image it is necessary to apply a defined kernel of $m \times n$ dimension. Keep in mind that the value of each pixel in the output image depends on the kernel dimension and on the weight w_n value of each cell. An example of a given kernel is given at Figure 4.11, in Gaussian spatial filters the weight values of the kernel positions x and y is be governed by a Gaussian function represented at Equation 4.20 where σ is the standard deviation, and the x and y the the kernel cell coordinate. To generate these values we assume the center as the coordinate origin.

$$h(x, y) = e^{-\frac{x^2+y^2}{2\sigma^2}} \quad (4.20)$$

w_1	w_2	w_3
w_4	w_5	w_6
w_7	w_8	w_9

Figure 4.11: An example of a 3x3 kernel size.

Average spatial filter

The average spatial filter is one of the most simple filter used to blur the output image to remove undesired noise. Its implementation is straight forward and the result of each pixel is governed by the Equation 4.21.

$$R = \frac{1}{n} \sum_{i=1}^n z_i \quad (4.21)$$

where n is the dimension of a square kernel matrix, and z_i the value of each cell. A good example of a kernel used in the average filter is shown in Figure 4.9 [39].

A comparison of smoothing filters for a WAAM cell using CMT is performed by COUTO *et al.* [18]. The image acquisition is performed using a Xiris HDR welding camera for a single bead deposition. The experiment and its results is described at section 6.1.

4.2.5 Sharpening spatial filters

The main objective of a sharpening spatial filter, is to highlight the transition in intensity of an image. Since averaging can be an analogue to integration, the sharpening operation can be taken by spatial differentiation. The derivative of a digital function is defined in terms of the difference between the pixel value of a certain region. There are two ways to identify it: (i) using first derivative; (ii) using second derivative. A basic definition of the first-order derivative of an one dimensional function is given by Equation 4.22 [39].

$$\frac{\partial f}{\partial x} = f(x + 1) - f(x) \quad (4.22)$$

Since the image function is composed of the axes x and y , the partial derivative is performed along these two axes. Equation 4.23 represents the second-order derivative of an one dimensional function, also applied for the second order image gradient for both x and y direction [39].

$$\frac{\partial^2 f}{\partial x^2} = f(x + 1) + f(x - 1) - 2f(x) \quad (4.23)$$

Second order derivative for image sharpening - the Laplacian

The implementation of a second-order derivative into a 2-D image, is performed by the definition of a discrete formulation of the second-order derivative 4.23 and then use a filter kernel based on this formulation. Therefore, for a good implementation, isotropic filters are used. Their response are independent of the direction of the discontinuities in the image to which the filter is applied. A simple isotropic

derivative operator is the Laplacian define at Equation 4.24, which, for a function (image) $f(x, y)$ of two variables.

$$\nabla^2 f = \frac{\partial^2 f}{\partial x^2} + \frac{\partial^2 f}{\partial y^2}. \quad (4.24)$$

The expression of this equation in the x direction is obtained by 4.2.5, and by 4.2.5 for the y direction.

$$\frac{\partial^2 f}{\partial x^2} = f(x + 1, y) + f(x - 1, y) - 2f(x, y),$$

$$\frac{\partial^2 f}{\partial y^2} = f(x, y + 1) + f(x, y - 1) - 2f(x, y),$$

The implementation of the Laplace filter expression 4.24 is enabled by the use of the kernel shown in Figure 4.12a. Its application of the image highlights intensity discontinuities since it is a derivative operator.

0	1	0	1	1	1
1	-4	1	1	-8	1
0	1	0	1	1	1
(a)			(b)		

Figure 4.12: Kernels used for the Laplacian operation over a function $f(x, y)$ (image). Where: (a) Kernel operator user to implement the expression 4.24; (b) Kernel user to implement the Laplacian operator, however now the diagonal terms are taken into account.

First-order derivatives for image sharpening

The first-order derivative application on a given image is performed using the gradient. For a function $f(x, y)$, the gradient at a correspond (x, y) coordinate is defined by 4.25. It has the important geometrical property that it points in the direction of the greatest change of the image at the location (x, y) [39].

$$\nabla f = grad(f) = \begin{bmatrix} g_x \\ g_y \end{bmatrix} = \begin{bmatrix} \frac{\partial f}{\partial x} \\ \frac{\partial f}{\partial y} \end{bmatrix} \quad (4.25)$$

The magnitude $M(x, y)$ (length) of the vector ∇f is denoted by 4.26, it value at (x, y) is denoted as the rate of change in the direction of the gradient vector.

$$M(x, y) = \text{mag}(\nabla f) = \sqrt{g_x^2 + g_y^2} \quad (4.26)$$

An example of kernels used for the first-order derivative is presented in Figure 4.13. The gradient operator is used frequently for industry inspection, to aid humans in the failure analysis routines, and also more common, for preprocessing step in automated processing, such as WAAM [39].

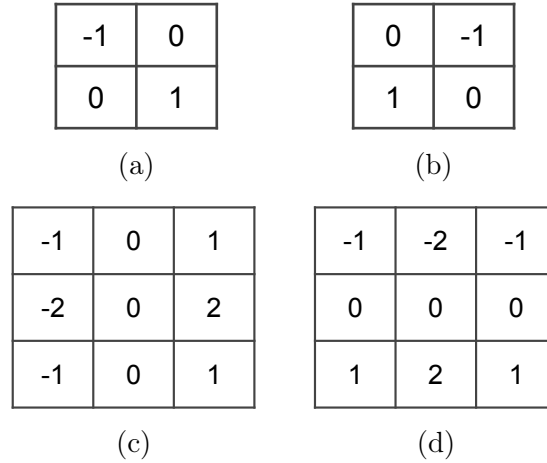


Figure 4.13: First-order derivative operators. Where (a) and (b) are the Roberts cross gradient operator, and (c) and (d) the Sobel operator.

These filters are used to highlight important details of an object (borders), and in many cases when a specific object or known characteristics is aimed it is performed after the segmentation step to avoid the process of unnecessary noise.

4.2.6 Image Segmentation

The importance of image segmentation is related to the possibility of extracting useful information easier. The most common way of doing it is with a gray level image and a threshold. E.g. in welding it has the goal to differentiate the weld seam and it's surroundings and help further data analysis [72].

The step of segmenting the image in two well defined color is also be considered as filtering in some papers of the literature, at this work it will be treated as an image treatment step. As mentioned, the importance to use it is to simplify the image, remove extra noises, and unnecessary features. In some scenarios it is used right after applying the smoothing filters, which is the case of the present work. Segmentation can sometimes also be called binarization, it helps edge and bead geometry process detection. On XUE *et al.* [72], the raw images are represented by a function $f(x, y)$ and an appropriate threshold T is selected for the segmentation process. The new image $g(x, y)$ is created accordingly with the Expression 4.27.

$$g(x, y) = \begin{cases} 1 & f(x, y) > T \\ 0 & f(x, y) \leq T \end{cases} \quad (4.27)$$

Figure 4.14 gives an example of a raw image acquired with a HDR camera and the segmentation result after using a fixed threshold. On MA *et al.* [45], the image segmentation also used the same characteristics as the cited above. A threshold was also used to separate the target information from the non-desired information, the author used $k = 255$ as threshold due the arc intensity.

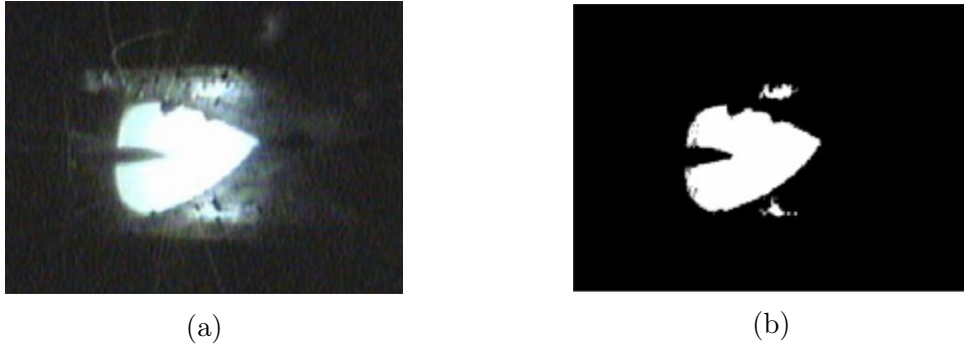


Figure 4.14: Image segmentation example. Where (a) represent the raw image acquired and (b) the binary image with the desired features highlighted. [72].

Several research on image segmentation was done on aluminum joints welding using GTAW. On GMAW, there are limited published works on ferrous materials, the detection and segmentation on steel work pieces has a higher degree of complexity due to almost everything being made of steel. This characteristics makes the image segmentation algorithm implementation more difficult [44].

4.2.7 Edge Detection

Edge detection is a very important part of image processing step during arc welding due to the further necessity of a machine to recognize the seam dimension, it enhances the contour of a image to make the identification of borders, joint and other characteristics easier by the machine [41]. A good edge detection algorithm mitigate errors and prevent manufacturing failures during metal deposition.

Edge pixels are the ones that have their intensity changing abruptly, and edges are the set of these edge pixels. Edge detectors are local image processing methods designed to detect the edge pixels [39]. The process is mainly performed after a gray scale conversion. Some modified algorithms are also used to search and diminish problems or noises embedded in the process. In J. e SB. [41] a modified algorithm is proposed, it's objective is to enhance the edge contour before running the edge algorithm to avoid detection failures.

The tool of choice to find the edges strength and the direction of an image f , is the gradient 4.25, which has a important geometrical property, it points to the greatest rate of change of f at an analyzed (x, y) location. The magnitude length vector 4.26 is the value of the rate of change in the direction of the gradient vector. The direction of the gradient vector is than given by Equation 4.28, and is measured with respect to the x-axis. The direction of the edge at an image f arbitrary point (x, y) is orthogonal to the direction of the gradient vector α at the same point.

$$\alpha(x, y) = \tan^{-1} \left[\frac{g_y}{g_x} \right] \quad (4.28)$$

The presence of noises like jigs, cable lines, platform, light changes, and others, makes the edge detection process a challenge [12]. In according to XUE *et al.* [72], using edge detection is the key for extracting valuable information. Most of the algorithms are based on gray scale images and the most used are the differential ones. The differential algorithm takes into account the first or second derivative to post process and refine the output. Inside this class, Canny operator and Laplacian operator are improved algorithms and are commonly used.

On MA *et al.* [47] a comparison between some operators are performed. The Prewitt, Roberts, Kirsch and Canny operators are compared for their edge detection performance. The original image used for the edges operator can be seen in Figure 4.15, the output image from the edge detection operator are displayed at Figure 4.16 where the Canny operator as shown in Figure 4.16d presented the best detection, Canny is also one of the most popular algorithms for edge detection and broadly used [56]. A similar work is performed on COUTO *et al.* [18], where a comparison of the Laplacian, Sobel, Schar and Canny edge operators for single-bead deposition with a CMT WAAM cell. The Canny operator also presented the best result for the edge detection in this work. The experiment results are detailed in section 6.1.

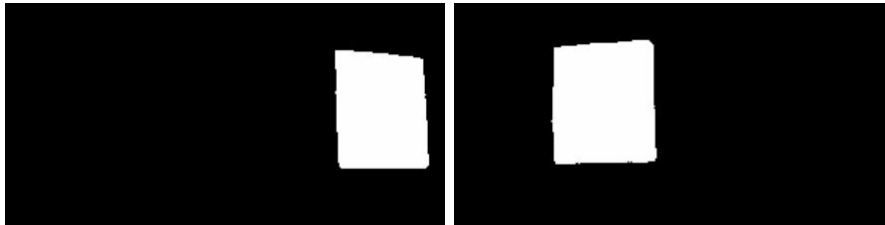


Figure 4.15: Image capture after threshold

Since edge detection is one of the most important steps of a vision-based algorithm, its application must be well designed, and the possible variations (material, deposition process) that might happen during the manufacturing must be considered to make possible the usage of post-processing algorithms responsible

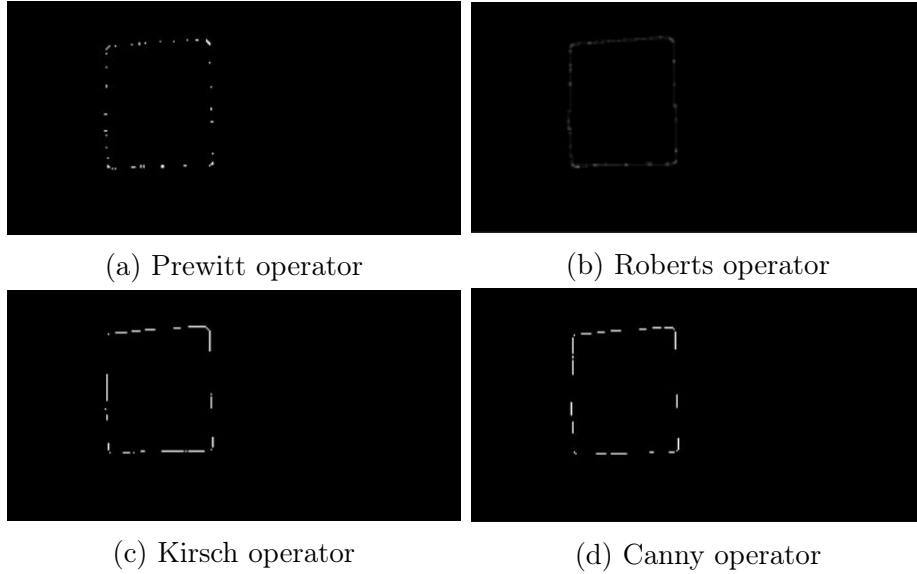


Figure 4.16: Edge detection operators comparison [47].

to extract the desired features while printing, e.g. the lines, the geometry, and the object identifications.

Canny edge operator

Since Canny operator is used in the present work, it receives a special attention. Canny edge detector algorithm in general is superior to the edge detector mentioned thus far. Its approach is based on three basic objectives: *(i)* Low error rate *(ii)* Edge points should be well localized; *(iii)* Single edge point response.

To implement the optimal edge detector, the first derivative of a Gaussian is used. To implement this, a Gaussian smooth filter is applied to the input image, and then is followed by computing the gradient magnitude and direction. Edges using the gradient are generally thick due to the first derivative characteristics when applied to compute the intensity change in an image f . Therefore the next step of Canny algorithm is to thin those edges which is performed by the nonmaxima suppression [39].

The nonmaxima suppression specifies a number of discrete orientations of the edge normal (gradient vector). For example for a 3×3 region it is possible to define four orientations for an edge passing through the center point of the region (horizontal, vertical and both diagonals). And by examining the pixel values in a local neighborhood normal to the edge direction, that is the direction of the edge gradient, we can find the maximum value and set all other pixels to zero [39].

The final step is the threshold, if a single threshold T is used, if a value is below the defined threshold the value are set to 0. Therefore if the threshold is set too low, there will be false edges, and if set too high then actual valid points are eliminated.

Canny algorithm attempts to improve in this situation by using hysteresis threshold, which is composed of two thresholds: (i) a low threshold T_L and a high threshold T_H . For each nonzero pixel that exceeds the upper threshold a chain is created of adjacent pixels that exceed the lower threshold, and any other pixels are set to zero. The algorithm consists of the following basic steps [39]:

1. Smooth the input image with a Gaussian filter.
2. Compute the gradient magnitude and direction.
3. Apply nonmaxima suppression to the gradient magnitude image.
4. Use double threshold and connectivity analysis to detect and link edges.

4.2.8 Line Identification

Once the edge image is acquired, it is used to compute if a set of these pixels is lied on a predefined shape. Lines are distinct visual features that are commonly expected in man-man environment, e.g. roads edges, buildings, doorways. In the WAAM deposition, the single and multi-bead boundaries are both represented by lines. Suppose that a task is configured to find if a set of the points of the edge image is part of a straight line, one possible solution is to find all the lines represented by every pair of points and then find all subsets of points that are close to a particular line. However this is a prohibitive computational task, therefore not ideal for an online monitoring application [39].

HOUGH [40] proposed a different approach to identify these geometric features with a lower computational cost, it is commonly known as Hough Transform. Consider a point (x_1, y_1) in xy -plane, and general representation of the line in slope form is described by 4.29. Infinity lines can be represented passing through the point (x_1, y_1) , and it also satisfy the Equation 4.29 with varying values for a and b .

$$y = a x_i + b \tag{4.29}$$

This equation can also be written in the parameters representation as shown in 4.30, and then the $a b$ -plane (parameter space) can be set. Where a line, based on the value of a point from the xy -plane is now represented as a line in the ab -plane, with the x and y varying.

$$b = y - a x_i \tag{4.30}$$

A second line can also be represented in the parameter space when a second point (x_2, y_2) is considered. Unless they are parallel both lines intersect at some point

(a_i, b_i) , where a_i is the slope and b_i the intercept of the line containing both points of the xy -plane, Figure 4.17 illustrates this concept. However this representation has a problem, when the slope of the line approximates 90 degrees, the value of the slope (a) tends to infinity. One way around this problem is to use the line normal representation 4.31. Figure 4.18 details this implementation.

$$x \cos \theta + y \sin \theta = \rho \quad (4.31)$$

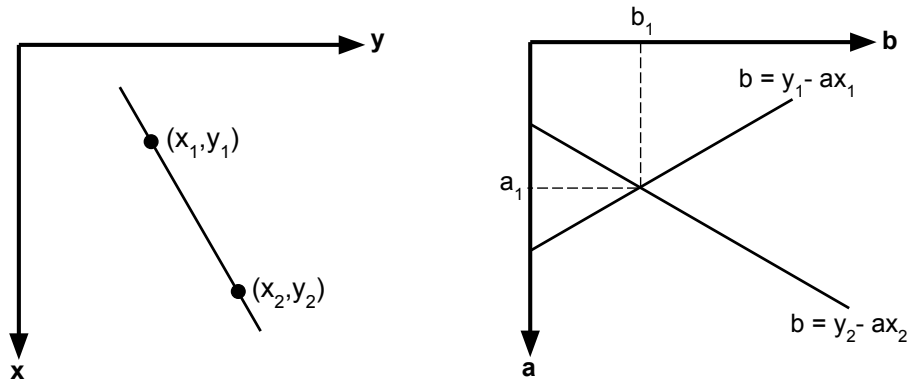


Figure 4.17: Line and point representation at xy -plane and ab -plane. Adapted from [39].

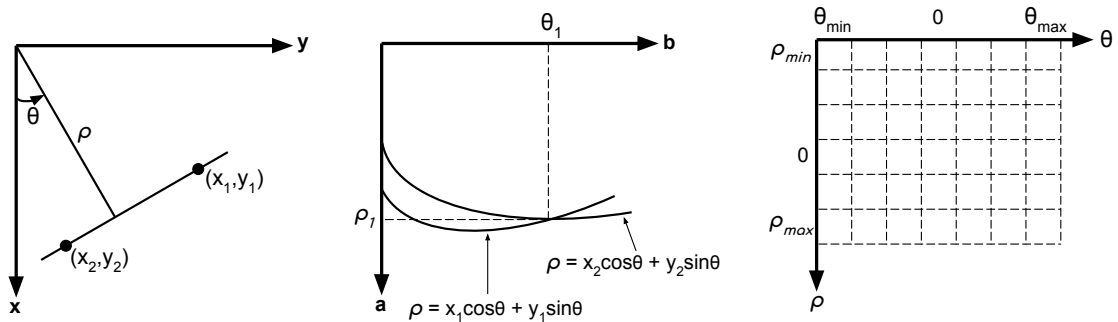


Figure 4.18: Line and point representation at xy -plane and $\rho\theta$ -plane. Adapted from [39].

The computational attractiveness of the Hough transform arises from subdividing the $\rho\theta$ -plane into accumulators cells A , as shown at Figure 4.18. The cell at a given coordinate $A(i, j)$ accumulate points for a line which n points of the xy -plane lie in its path, the dimension of each cell represents the accuracy of the algorithm but with the expense of computational cost. Therefore, the value in each cell at the end of the process represent the number of pixels lied above the line represented by that particular cell position (ρ, θ) , and so the dominant line in the scene. Figure 4.19 shows an example of the Hough transform algorithm applied at the edge image. The lines, which are the representation of the square four edges at

the uv -plane, where $u = x$ and $v = y$, are given by the 4 highest intersection points of the $\rho\theta$ -plane since they got the highest amount of votes [16, 39].

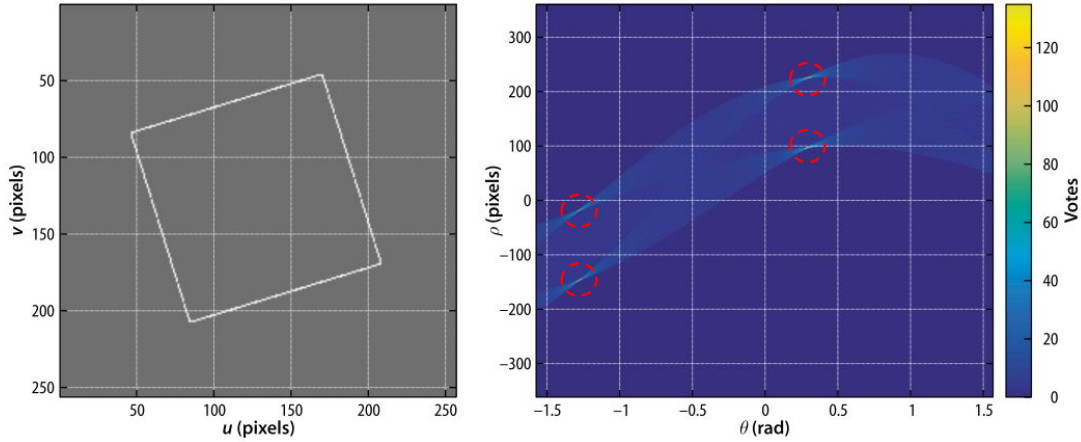


Figure 4.19: Example of the Hough transform algorithm. Adapted from [16].

4.3 Gaussian Filters

Gaussian filters historically constitute the earliest tractable implementations of the Bayes filter for continuous spaces. They are also by far the most popular family of techniques to date. Gaussian techniques all share the basic idea that beliefs are represented by a multivariable normal distributions

$$p(x) = \det(2\pi\Sigma)^{-\frac{1}{2}} \exp\left\{-\frac{1}{2}(x - \mu)^T \Sigma^{-1}(x - \mu)\right\}. \quad (4.32)$$

The density function 4.32 is characterized by two sets of parameters: the mean μ and the covariance Σ . Where the mean posses the same dimension as the state x . The covariance matrix is quadratic, symmetric, and positive semidefinite.

Consider a system which has a true state that evolves over time according to an applied input, and that it is not possible to directly measure the state. While sensors of the system have outputs that are a function of the true state. The challenge is to estimate the unknown true state x and how certain we are of that estimate, based on the given inputs and the sensors output.

The estimation problem can be summarized by: given a model of the system $f(\cdot)$, $h(\cdot)$, \hat{V} and \hat{W} ., the known inputs applied to the system u , and some noisy sensor measurement z , to find an estimate \hat{x} of the system state and the uncertainty \hat{P} in that estimate.

4.3.1 Kalman Filter

The Kalman filter is an optimal estimator for the case where the process and measurement noise are zero-mean Gaussian noise. It is used for continuous states, and not applied for discrete or hybrid state spaces. Consider the model described as a discrete-time linear invariant system

$$x(k) = Fx(k-1) + Gu(k-1) + v(k-1) \quad (4.33)$$

$$z(k-1) = Hx(k-1) + w(k-1) \quad (4.34)$$

Where k is the time step, $x \in \mathbb{R}^n$ is the state vector, and $u \in \mathbb{R}^m$ is a vector of inputs to the system at time $k-1$. The matrix $F \in \mathbb{R}^{n \times n}$ describes the dynamics of the system, and the matrix $G \in \mathbb{R}^{n \times m}$ describes how the inputs are coupled to the system states. The vector $z \in \mathbb{R}^p$ represents the outputs of the system as measured by the sensors, and the matrix $H \in \mathbb{R}^{p \times n}$ describes how the system states are mapped to the system output which we can observe. The error (noise) of the process and the measurement is represented by $v(k-1)$ and $w(k-1)$ respectively, which are Gaussian random variables $N(0, V)$, see Figure 4.20, with zero mean and covariance $V \in \mathbb{R}^{n \times n}$. Covariance is a matrix quantity which is the variance for a multi-dimensional distribution, a positive definite matrix and therefore symmetric [16].

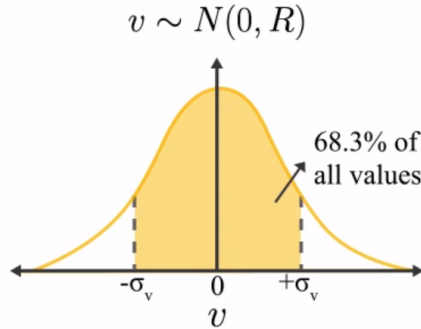


Figure 4.20: A random variable graph representation, where 68.3% of all values are inside the covariance range. Retrieved from <https://www.mathworks.com/videos/understanding-kalman-filters-part-3-optimal-state-estimator-1490710645421.html> at 03/25/2022.

The Kalman filter is composed of two main steps, the prediction and the update. The prediction step is computed based on the previous states and inputs, where \hat{x} and \hat{P} are the estimate for the state and the covariance matrix respectively. They are described by 4.35 and 4.36.

$$\hat{x}_k = Fx_{k-1} + Gu_k \quad (4.35)$$

$$\hat{P}_k = FP_{k-1}F^T + \hat{V} \quad (4.36)$$

The indicated term \hat{P} project the estimated covariance matrix from the current time to the next, it is the result of the computation of two positive-definite matrices, therefore in this step the uncertainty will increase. However, \hat{V} must be a reasonable estimate of the actual process noise to avoid a computed pessimist estimate when overestimating the uncertainty. To correct the uncertainty growth it is necessary to add the measurement made by the sensors to the estimation model. The difference between the prediction and the sensor measurement is given by 4.37.

$$v = z_k - H\hat{x}_k \in \mathbb{R}^p \quad (4.37)$$

A portion of this difference is caused by the measurement noise, Equation 4.37 provides valuable information related to the error of the actual and the predicted state. A good approach for this information is to call it *innovation* rather than error, since it is used to adjust the state estimate with the Kalman gain. The second step of the Kalman filter is the *update*, that maps the innovation into a correction for the predicted state, tweaking the estimation based on what the sensors observed, this tweaking is performed by the Kalman gain 4.38.

$$K = P_k H^T [H P_k H^T + \hat{W}]^{-1} \in \mathbb{R}^{n \times p} \quad (4.38)$$

$$P_k = \hat{P}_k - KH\hat{P}_k \quad (4.39)$$

$$x_k = \hat{x}_k + Kv \quad (4.40)$$

The denominator term of 4.38 is the estimated covariance matrix of the innovation, and comprises the uncertainty in the state and the estimated measurement noise covariance. For example, if the innovation has high uncertainty in some dimensions then the Kalman gain value will be low for that dimensions. In other words, if the new information is has a high degree of uncertainty then only small changes are made to the state vector. Some characteristics can be highlighted for the Kalman filter: (i) It is an optimal filter; (ii) It is recursive, the output of one interaction is the input for the next; (iii) It is asynchronous, if there is no sensor data in one of the interactions the algorithm just perform the prediction step [16, 60].

A simple example of the Kalman filter is shown at Figure 4.21. After the car move from its initial known state estimate x_{k-1} , the a new predicted state estimate \hat{x}_k is computed based on the system dynamics and the control inputs. With the

updated measurement, the optimal state estimate x_k is computed using both the measurement the predicted state.

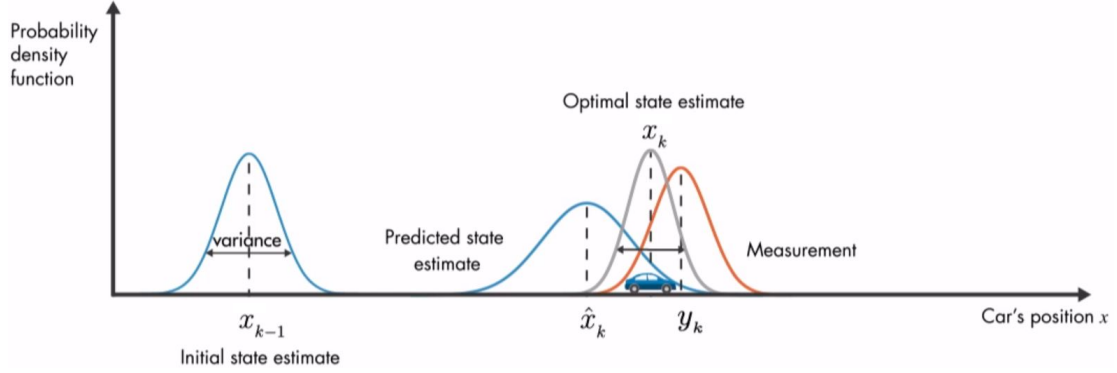


Figure 4.21: A car state estimate example after one time step. Adapted from <https://www.mathworks.com/videos/understanding-kalman-filters-part-3-optimal-state-estimator-1490710645421.html>, retrieved at 03/25/2022.

4.3.2 Extended Kalman Filter

The extended Kalman filter (EKF) is used for non-linear systems. Where the state transition 4.41 and the sensor model 4.42 are described by two non-linear functions 4.41 and 4.42, where the model uncertainty, external disturbances and sensor noise are represented by two Gaussian random variables v and w .

$$x_k = f(x_{k-1}, u_{k-1}, v_{k-1}) \quad (4.41)$$

$$z_k = h(x_{k-1}, w_{k-1}) \quad (4.42)$$

Since the Kalman filter is applied for unimodal distributions and linear systems, it is a necessity to linearize the state transition function about its current state estimate x_k as shown in Equation 4.43 [60].

$$x_k \approx F_x x_{k-1} + F_u u_{k-1} + F_v v_{k-1} \quad (4.43)$$

$$z_k \approx H_x x_{k-1} + H_w w_{k-1} \quad (4.44)$$

Where F and H are Jacobians of the functions described at 4.41 and 4.42 around the current state estimate as previously mentioned. When the disturbances are considered equal to 0 ($v_{k-1} = 0$) in Equation 4.41, the prediction (4.45 and 4.46) and update (4.47 and 4.48) Equations can be written as:

$$\hat{x}(k) = f(\hat{x}(k-1), u(k-1)) \quad (4.45)$$

$$\hat{P}(k) = F_x \hat{P}(k-1) F_x^T + F_v \hat{V} F_v^T \quad (4.46)$$

$$x(k) = \hat{x}(k) + K v \quad (4.47)$$

$$P(k) = \hat{P}(k) - K H_x \hat{P}(k) \quad (4.48)$$

It is important to mention that these equations are only valid at the mentioned linearization point, and that the Jacobian must be computed at every iteration [16].

Chapter 5

Bead Geometry Estimation and Localization Algorithms

In this section it is presented the algorithm developed to monitor the deposition and estimate the bead width and centerline during the print. As mentioned in section 3, the bead width has a direct influence with the optimum overlapping distance of adjacent beads, and this parameters directly influence the surface quality of the layer and the geometric accuracy of a part. Some examples of noise occurrences while printing is shown at Figure 5.1, where the presence of fumes, arc, radiation, light variation, and spatter are presented. These characteristics make the estimation through vision a challenge.

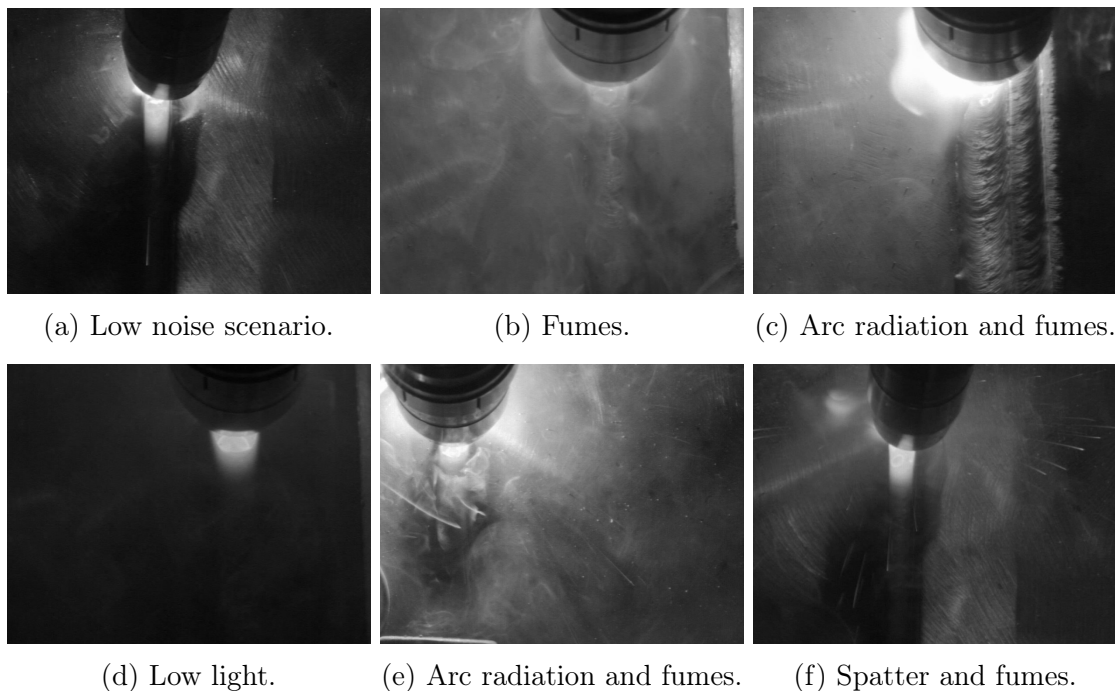


Figure 5.1: Captured frames during the monitoring and their different noises [17].

It is important to highlight that in the chapters 6 and 7, it is presented the

historical setup used for the experiments performed at the current work as well as the result obtained so far in the development. Each step of the vision-based algorithm are tested for better performance for the current application and could be modified and upgraded during the development, where as in this chapter the algorithm described will be in its last release state.

5.1 Bead geometry measuring algorithm

The vision-based proposed algorithm developed to extract the features and real-time estimate the bead width and position in a WAAM deposition scenario with CMT is detailed at Figure 5.2 and in the followed steps:

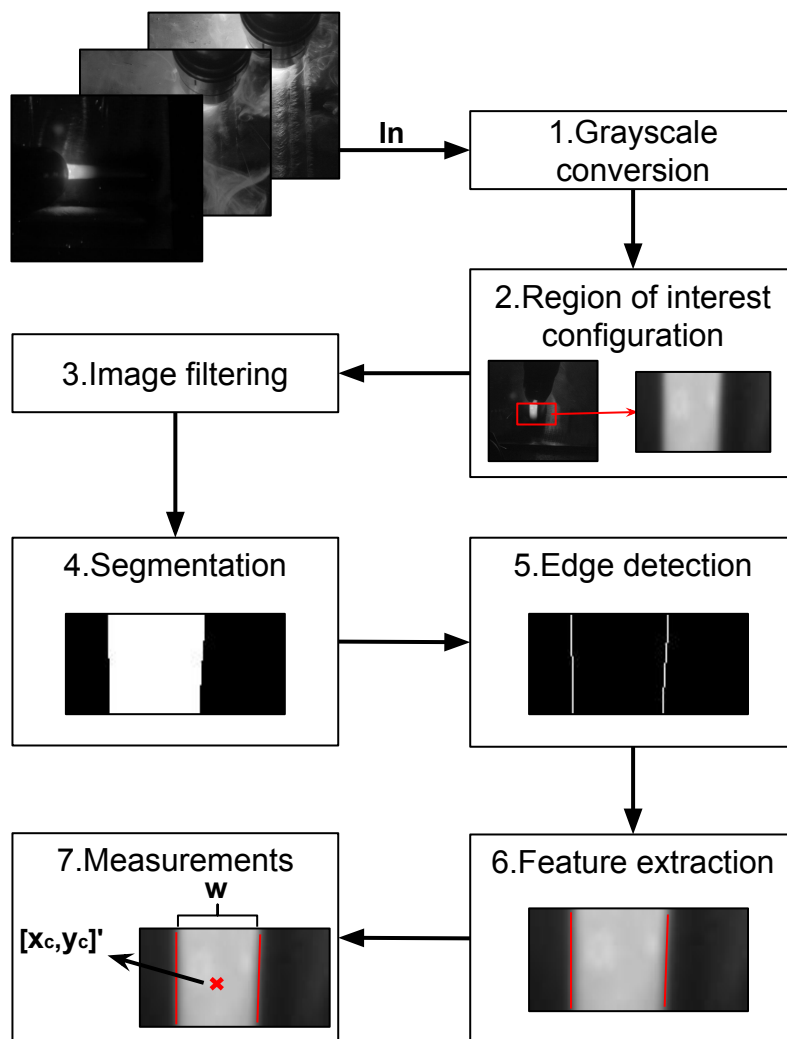


Figure 5.2: Stages used in the vision-based algorithm [17].

Step 1: Receive the image from the camera and converted to gray-scale, which reduces computation cost and standardizes its format;

Step 2: define the region of interest (ROI), that reduces the CPU cost and process only the image inside its region;

Step 3: Apply a Gaussian spatial filter 4.2.4 at the ROI image to attenuate the noise and smooth it;

Step 4: Segment the filtered image $I_{in}(x, y)$ with an adaptive binary threshold algorithm, resulting in a binary image. The output pixel $I_{out}(x, y)$ at a location (x, y) assumes maximum value I_{max} when it is above the computed threshold T , or 0 otherwise, as follow.

$$I_{out}(x, y) = \begin{cases} I_{max}, & \text{if } I_{in}(x, y) \geq T, \\ 0, & \text{otherwise.} \end{cases} \quad (5.1)$$

The adaptive threshold is computed at every frame, assuming the mean value of a region inside the ROI, and can also be adjusted with a fitting variable.

Step 5: detect the edges in the segmented image using the Canny algorithm [4]. Edges are the result of intensity change evaluation in an image f at location (x, y) , and are obtained through first or second-order derivative in orthogonal directions using an image gradient ∇f given by 5.2:

$$\nabla f = grad(f) = \begin{bmatrix} g_x \\ g_y \end{bmatrix} = \begin{bmatrix} \frac{\partial f}{\partial x} \\ \frac{\partial f}{\partial y} \end{bmatrix}. \quad (5.2)$$

Step 6: use a point cloud image from the edge detection algorithm for the line identification. A subset of this point cloud is tested, and through the Hough-lines transform, lines are then identified. In general, lines are described in terms of a minimum representation as $y = mx + c$ where (m, c) are the lines parameters. However, such a description is troublesome for the case of vertical lines where $m = \infty$. Then, it is usual to represent lines using (ρ, θ) parameterization as:

$$y = -x \tan(\theta) + \frac{\rho}{\cos(\theta)}, \quad (5.3)$$

where $\theta \in [\frac{-\pi}{2}, \frac{\pi}{2})$ is the angle from the horizontal axis to the line and $\rho \in [-\rho_{min}, \rho_{max}]$ is the perpendicular distance between the origin and the line.

Hough-lines transform has a strong anti-noise ability; therefore, it is well applied to detect feature in low signal-to-noise ratio scenarios [69], and may be satisfactorily applied in WAAM. However, due to high level of noise and non-linearity of the process, many undesirable lines are identified and need to be filtered. To overcome these issues, the filtering is performed by using

the orientation of the end-effector velocity in the image plane. Since the bead edges are parallel to the end-effector velocity vector, lines with a deviation above a defined threshold are rejected. It is possible to see that the bead edge formation has little or no deviation when compared to the direction of the velocity vector (Fig. 5.3). After identifying all possible lines, the undesired lines (red) are rejected, and the desired (green) accepted.

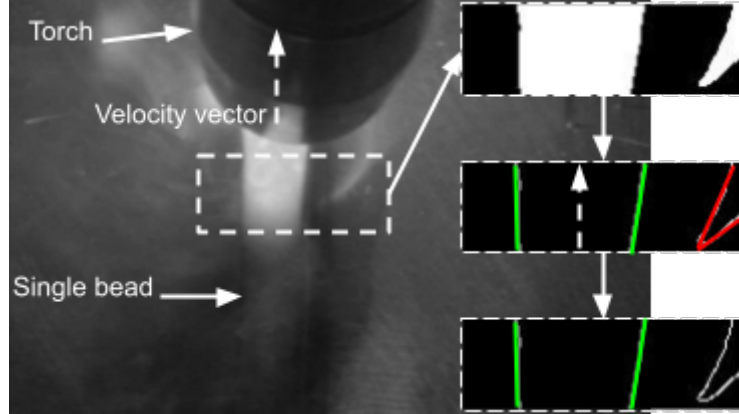


Figure 5.3: Removing undesired lines.

In many frames analyzed during the printing, multiple lines are identified for the same bead edge. After comparing all lines, if their parameters (ρ, θ) are below a given threshold, they are considered the same line and their mean is computed and adopted as a new line.

Step 7: some previous filtering must also be performed to measure the bead width and position and avoid undesirable lines. First, an orthogonal line to the end-effector velocity vector that passes through a configurable point (C_0) is calculated inside the ROI (Figures 3.1 and 5.4). The intersection points of the orthogonal line with the bead edges (P_1 and P_2) are used to compute the bead width (w) and centerline (C).

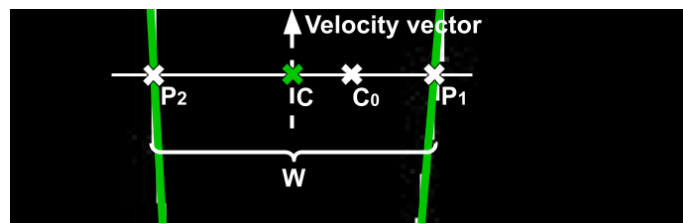


Figure 5.4: Bead width and centerline computed by the algorithm.

It is assumed a constant and symmetric bead profile for measuring the bead centerline position. Ideally, the bead centerline (C) (Figure 3.1) follows the deposition path planned, which is not always the case as its deposition might

be affected by the metal droplet misplacement, asymmetric temperatures surrounding the sides of the bead (as for parallel bead deposition) and low quality wire feedstock. The bead centerline position is also used to find where the bead width is being measured in the substrate, which creates a database for future analysis of possible failures and improves quality control of the part. The bead position is then transformed from the image plane to the substrate reference frame $\{S\}$, using the camera projection matrix and the known poses of the substrate, torch, and camera.

5.1.1 Multi-Bead width measuring

A common aspect of WAAM is the necessity of depositing many adjacent beads at a given layer during the part buildup, this particular scenario has a higher degree of noise when compared with single-bead deposition. The challenge of measuring the width in multi-bead layer deposition arises because one bead edge cannot be seen clearly (Fig. 5.5). When a single bead is printed, its edges are identified through the difference of light emitted in the intersection of the bead with the substrate; in multi-bead printing, there is overlapping of two beads and the identification of the edge in the overlap region becomes more complex because it depends on the light emitted and on the intersection of the two passes, which makes the bead width measurement problematic.

For the multi-bead width estimation proposal, width variation is detected and expected in the measurements of the subsequent bead $_k$ with $k=2, \dots, n$ to the first deposited bead $_1$ provided that the measurement pattern changes. The first bead width W_1 is measured by identifying its two edges which intersects the substrate. However, the next deposited beads only intersect the substrate in one edge whereas the second edge intersects the previous bead at the valley area that results in a different measurement pattern with bead width W_2 , as described in Fig. 5.5. The edge intersecting the substrate (the previous layer) has a clearer view and it is much easier to identify when compared to the other edge, that is influenced by higher process noise.

5.1.2 Bead placement estimation during the deposition

The bead placement readings performed during the print is achieved through the centerline estimation by the developed vision-based algorithm. Since the camera, the robot arm joints, and the end-effector pose are known at every iteration, it is possible to estimate the bead placement in real-time during a deposition with the use of the camera perspective model introduced at section 4.2.1.

These information is used to ensure the bead layer quality and can also be used

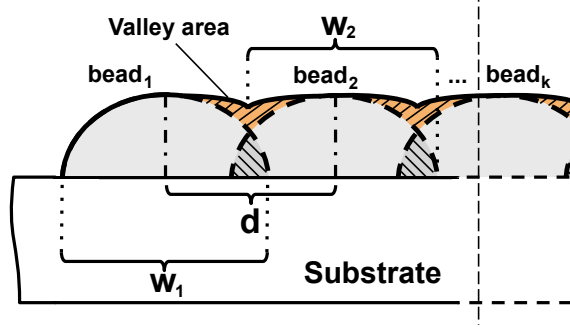


Figure 5.5: Multi-bead cross-section profile in WAAM, where d is the overlapping distance between the beads centerlines, W_1 is the width measurement pattern for the first bead deposited and W_2 the width measurement pattern for the subsequent deposited beads, and $bead_k$ represents a quantity k of beads deposited [17].

to develop defect prediction algorithms based on the width and the bead placement. The detail about how all the items are disposed and the poses relation between the items of the monitor and deposition system is shown in Figure 5.6. Joint 6 J_6 pose is computed with the forward kinematics algorithm, through a set of homogeneous transformations from the robot base to its last joint as shown in 5.4, and with the same operation the other references are known in every iteration during the deposition process.

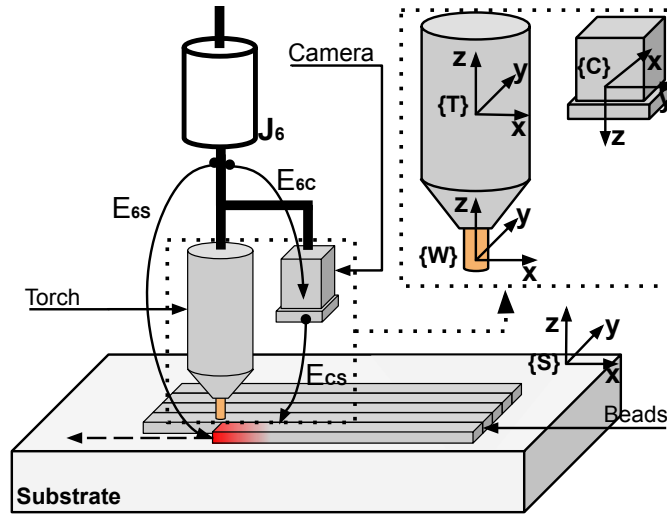


Figure 5.6: Multi-bead deposition and vision monitoring setup. Camera, torch and wire amplified with their coordinate systems [17].

$$T_{06} = T_{01} T_{12} T_{23} T_{34} T_{45} T_{56} \quad (5.4)$$

The camera pose is computed by the transformation $T_{6c} = T_{06} T_{6c}$, from the robot J_0 to the camera frame. Accordingly to what was shown at section 4.2.1, and considering that: (i) The camera pose is known; (ii) The camera distance to the substrate is known. The estimation is performed using the following assumption:

1. Bead geometry symmetry during the single-bead deposition.
2. A Gaussian thermal profile for single-bead and multi-bead deposition.

The centerline position representation at the world reference frame $\{0\}$ is computed accordingly to the following steps:

Step 1: Convert the feature position from the non-homogeneous representation $p = [u, v]$ to the homogeneous image plane representation $\tilde{p} = [\tilde{x}, \tilde{y}, \tilde{z}]$, with the known camera distance z_c .

Step 2: Compute the feature position in reference to the camera frame $\{C\}$, with the 4×3 inverse camera matrix as shown in Equation 5.5. Where C is the camera matrix, \tilde{p} is the point in homogeneous coordinates, and P_C the position of the point in respect to the camera frame. In this step a previously knowledge about the distance of the camera to the feature observed is necessary, since this information (DOF) is lost during the projection operation.

$$P_C = C^{-1} \tilde{p} \quad (5.5)$$

Step 3: Compute the feature position P in relation to the world frame $\{0\}$, with the camera homogeneous transformation T_C . Where 5.6 gives the transform from the camera frame to the world coordinates frame. See the schematic presented at Figure 4.5 and the Equation 5.7.

$$T_C = T_{06} T_{6C}. \quad (5.6)$$

$$P = T_C \tilde{P}_C \quad (5.7)$$

5.1.3 Measurement filtering

To monitor the system characteristics in WAAM particularly using CMT presents many challenges for the vision system. For online monitoring of the information desired, it is necessary to develop a filtering approach since CMT frequently generates reading failure. Therefore, a filter is developed to store valid readings using outlier rejection, handle data loss by comparing actual with previous identified features, and output data filtering through a set of stored information. The newly acquired data is stored in a vector with a user-configurable size (n_1) and stacked in a queue. Then, the latest valid data is stored in the first vector position while the oldest is discarded.

This is performed after outlier rejection with a second filter, called SFilter, which records valid and outlier data with 1 or 0, respectively. When the mean value of SFilter is equal to 0, outlier data is considered and stored in the main filter. The steps used for filtering the data measured are described in Figure 5.7. The flowchart steps happen for every frame delivered by the camera, being a continuous process. Output data is filtered using mean or low-pass band filtering.

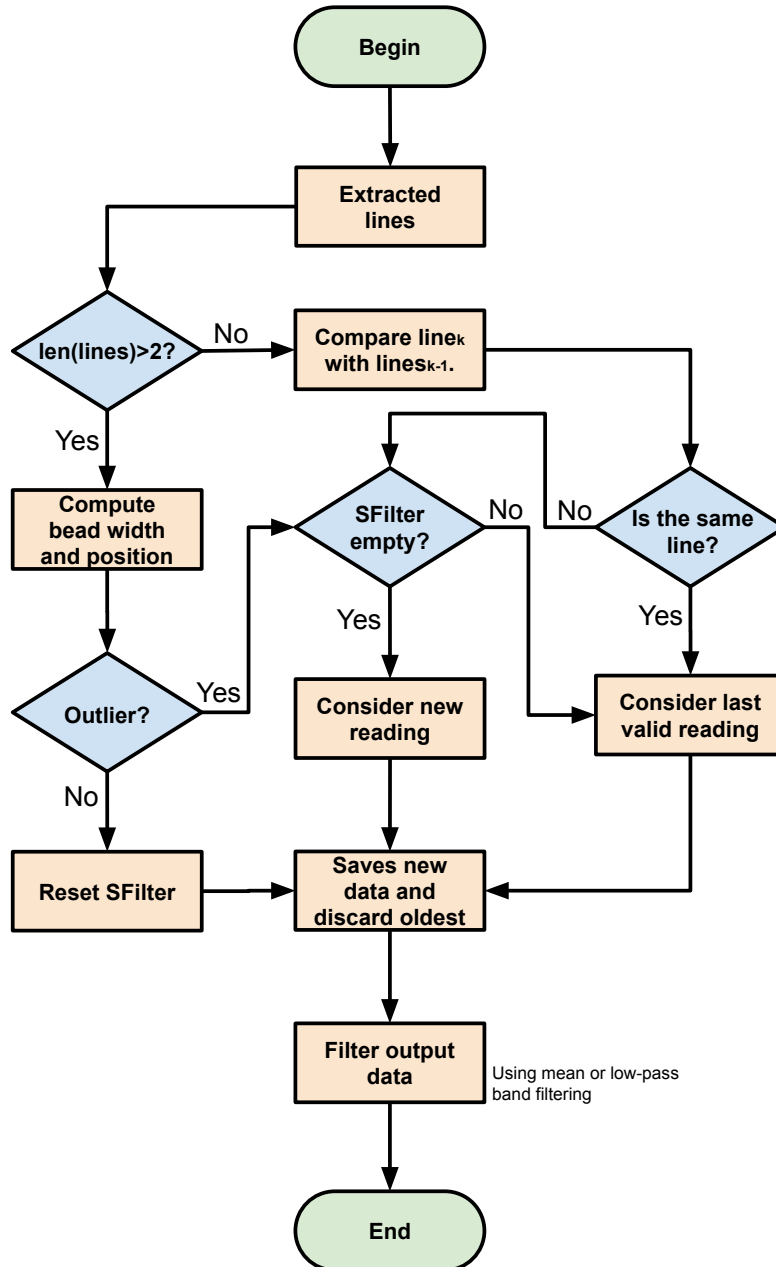


Figure 5.7: Filtering steps of the bead geometry estimation and localization algorithm.

5.1.4 Centerline estimation for WAAM with independent wire feeding system

To keep track of the bead position during the deposition with an independent wire feeding system (PAW, GTAW, etc), and also filter the estimation performed. A deposition simulation is performed with two cameras, where each of them make readings of particular characteristics of the deposition. Since the environment and the monitoring tends to be highly noisy an extended Kalman filter (EKF) is proposed for filtering and estimate the desired state. This simulation is developed inside Matlab with the purpose of testing the algorithm performance for the proposed problem and assumptions considered.

The simulation is configured with a 6-DOF robot arm (Kuka KR90 2700), an independent wire feeding system, and two HDR monocular cameras with the same parameter as Xiris XVC-1000 previously detailed. Zero mean Gaussian noise is used for the estimations performed through the cameras, and the assumptions considered are described as follows:

1. Globular droplet transfer mode;
2. The droplet is transferred to the substrate considering only the gravity influence;
3. The bead geometry is considered symmetric;
4. The wire stick-out length is constant;
5. Bead placement deviations are caused by wire tip lateral deviations of the planned path;
6. Bead width variations are caused by wire tip deviations along the path planned.
7. The centerline prediction and measurement are performed in the same area.

It is known that the wire quality influences the part quality, as presented by ZHAN *et al.* [76]. Figures 3.13 and 3.15 describe a deviation in the wire feeding, and Figure 5.8 shows an example of reading performed with a camera in the same configuration as camera 2 from Figure 5.9. This behavior is most noticeable when a low quality wire is used to build-up a part.

The bead centerline estimation is performed using the camera projection matrix with Xiris-1100 intrinsic parameters, and are specified in Table 5.1. Since the pose of the camera in relation to the joint J_6 is computed at every iteration using

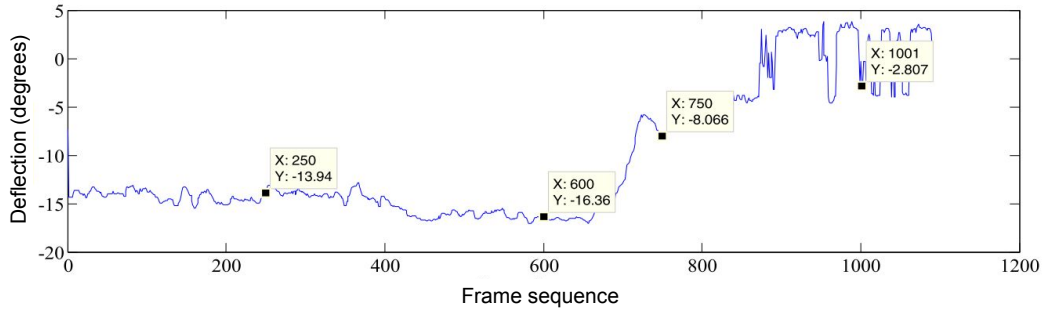


Figure 5.8: Wire stick-out orientation using a passive vision sensor. Adapted from ZHAN *et al.* [76].

Table 5.1: Camera main parameters used in the camera perspective model.

Characteristics	Value
Focal length	32 mm
Pixel size	$6.8 \cdot 10^{-6} m$
Resolution	1280×1024
Centre	[640, 512]

direct kinematics, the camera extrinsic parameters are known throughout the entire deposition.

The overall setup of the simulation is described at Figure 5.9. Where camera 1 is responsible to measure the centerline of the bead being deposited, and camera 2 is configured to capture the wire being fed to the system and estimate its angle deviation. A zero mean Gaussian noise is used to simulate the noise in both readings.

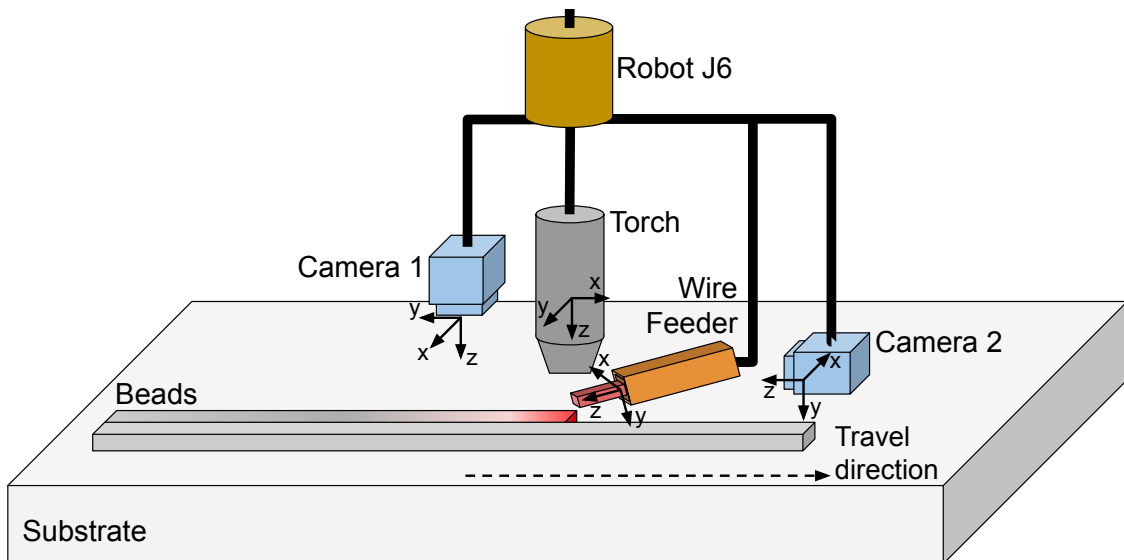


Figure 5.9: The Deposition setup proposed for the simulation. Camera 1 assembled in a top-view configuration to get the bead width and centerline and camera 2 assembled in a lateral-view configuration to get the wire feeder deviation angle.

Figure 5.8 shows an estimation of the wire deflection, which presents high noise

and some problems around the frame sequence 1000 with the deviation angle varying highly in a short amount of time. Another reading shown at ZHAN *et al.* [76] work is presented at Figure 5.10 where the presence of high noise with and high variance can be noticed.

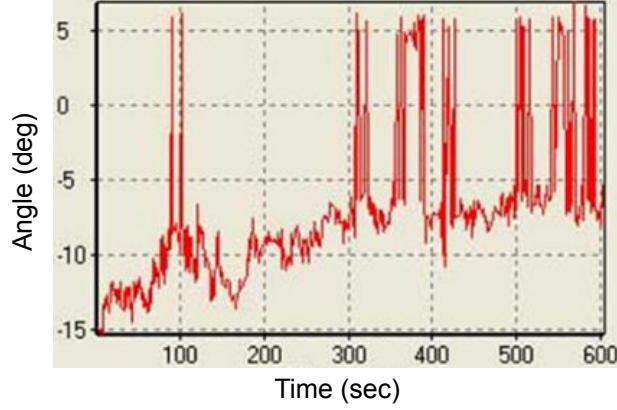


Figure 5.10: Noisy wire angle deflection reading. Adapted from ZHAN *et al.* [76].

It is challenging to monitor in a high-noise scenario, the noises embedded contributes to loss of signal and to increase the variance of the estimation performed. To overcome the noisy readings and improve the accuracy of the bead placement estimation, a model is proposed to govern the bead placement dynamics while also considering the wire deflection during a deposition. The unicycle model 5.8 is used in this simulation, it is a simple model but with important characteristics that helps to decrease the level of noise on the reading performed of the bead placement and make the monitoring system reliable. In this application its nonholonomic characteristics is an important feature, its orthogonal velocity constraint in relation to its heading direction (x unit vector) helps to attenuate the centerline estimation problems caused by the noise from both camera 1 and camera 2, as shown at both Figures 5.8 and 5.10.

$$\begin{bmatrix} \dot{x} \\ \dot{y} \\ \dot{\theta} \end{bmatrix} = \begin{bmatrix} \cos \theta & 0 \\ \sin \theta & 0 \\ 0 & 1 \end{bmatrix} \begin{bmatrix} v \\ w \end{bmatrix} \quad (5.8)$$

Two discrete forms of the unicycle dynamic are presented at Equations 5.9 and 5.10, which are respectively the result of using the Euler integration method and the second-order Runge-Kutta integration method [57]. They are tested to check the impact of the integration method used in the estimation accuracy. The linear form of the Equations 5.9 and 5.10 are described by Equations 5.11 and 5.12.

$$\begin{bmatrix} x_k \\ y_k \\ \theta_k \end{bmatrix} = \begin{bmatrix} x_{k-1} + v_k \delta_t \cos \theta_{k-1} \\ y_{k-1} + v_k \delta_t \sin \theta_{k-1} \\ \theta_{k-1} + \delta_t \omega_k \end{bmatrix} \quad (5.9)$$

$$\begin{bmatrix} x_k \\ y_k \\ \theta_k \end{bmatrix} = \begin{bmatrix} x_{k-1} + \delta_t v_k \cos(\theta_{k-1} + \omega_k \delta_t/2) \\ y_{k-1} + \delta_t v_k \sin(\theta_{k-1} + \omega_k \delta_t/2) \\ \theta_{k-1} + \omega_k \delta_t \end{bmatrix} \quad (5.10)$$

$$\begin{bmatrix} x_k \\ y_k \\ \theta_k \end{bmatrix} = \begin{bmatrix} 1 & 0 & -\delta_t v \sin \theta_{k-1} \\ 0 & 1 & +\delta_t v \cos \theta_{k-1} \\ 0 & 0 & 1 \end{bmatrix} \begin{bmatrix} x_{k-1} \\ y_{k-1} \\ \theta_{k-1} \end{bmatrix} + \begin{bmatrix} \delta_t \cos \theta_{k-1} & 0 \\ \delta_t \sin \theta_{k-1} & 0 \\ 0 & \delta_t \end{bmatrix} \begin{bmatrix} v_k \\ \omega_k \end{bmatrix} \quad (5.11)$$

$$\begin{bmatrix} x_k \\ y_k \\ \theta_k \end{bmatrix} = \begin{bmatrix} 1 & 0 & -\delta_t v \sin(\theta_{k-1} + \omega_k \delta_t/2) \\ 0 & 1 & +\delta_t v \cos(\theta_{k-1} + \omega_k \delta_t/2) \\ 0 & 0 & 1 \end{bmatrix} \begin{bmatrix} x_{k-1} \\ y_{k-1} \\ \theta_{k-1} \end{bmatrix} + \begin{bmatrix} \delta_t \cos(\theta_{k-1} + \omega_k \delta_t/2) & -\delta_t^2 v/2 \sin(\theta_{k-1} + \omega_k \delta_t/2) \\ \delta_t \sin(\theta_{k-1} + \omega_k \delta_t/2) & +\delta_t^2 v/2 \cos(\theta_{k-1} + \omega_k \delta_t/2) \\ 0 & \delta_t \end{bmatrix} \begin{bmatrix} v_k \\ \omega_k \end{bmatrix} \quad (5.12)$$

It is important to highlight that no control strategy with the purpose of keeping the bead placement above the desired trajectory is proposed in the current work, the observer is implemented and used with the intent of improving the quality of the estimation by filtering the outliers.

The unicycle model is used to pursue the wire tip position during the deposition, this is performed by the pure pursuit algorithm, a block diagram of the pure pursuit is detailed in Figure 5.11. The pure pursuit is a simple and effective algorithm for trajectory following, where the goal moves along the trajectory. The unicycle speed is computed by a proportional and integral controller, based on the distance between the current position of the unicycle and the position of the goal. The heading control is performed by a proportional controller, which is also based on the heading error of the unicycle and the vector orientation from it to the goal[16].

The pure pursuit is then used in the EKF to pursue the wire tip during a deposition process, and it is responsible of providing the state update in the prediction step. Hence, the EKF is used to attenuate the placement estimation noise. Figure 5.12 shows an upper view of the deposition system with the unicycle highlighted, the unicycle will follow the tip of the wire during the deposition as mentioned. The wire-feeder is configured with an angle of 70 degrees and the wire feeding angle deviation expected is inside the range of $[-15, 15]$ degrees. The droplet

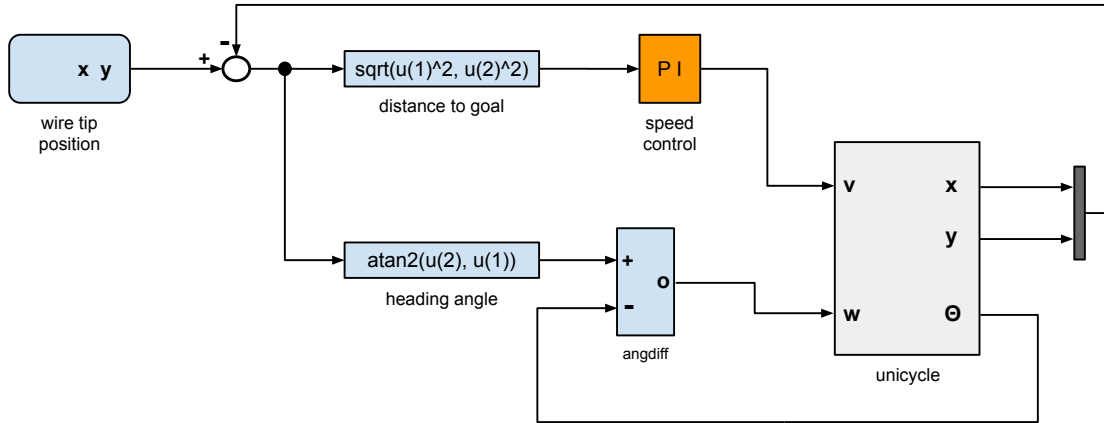


Figure 5.11: The block diagram of the pure pursuit algorithm with the unicycle dynamics. Adapted from CORKE [16].

deposition is governed by the gravity alone and the stick-out length is considered constant.

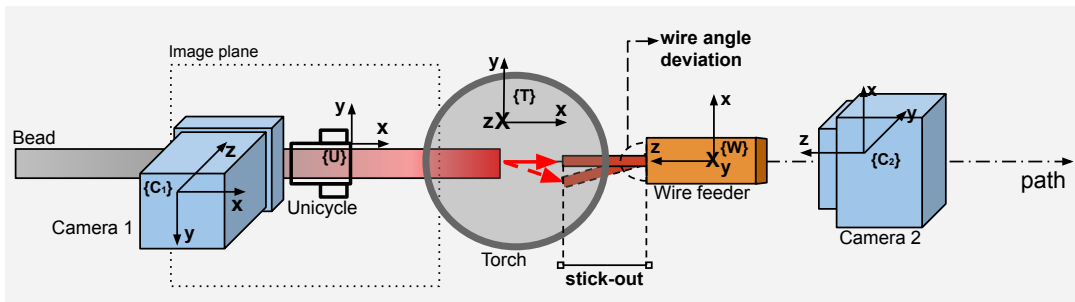


Figure 5.12: Topside view of the system simulation with the unicycle representation above the bead.

Camera 1 is focused at the bead formation area, right after the molten pool, like presented in Figure 5.4. It will gather bead centerline placement and width in real time. Camera 2 is used to capture the wire tip deviation angle, as presented also in Figure 3.15, its usage is based on the results presented in the work publish by ZHAN *et al.* [76].

The state transition and measurement covariance matrices are shown at 5.13 and 5.14. The diagonal values from the measurement covariance matrix related to x and y are estimated with some samples of centerline monitoring and with the use of the maximum likelihood estimation (MLE) algorithm. The covariance matrix from the state transition is defined using the data from the work of ZHAN *et al.* [76], in the current work the bead deviation is proposed to be the result of the wire feeding deviation projection in the substrate.

$$\hat{V} = \begin{bmatrix} 0.087^2 & 0 & 0 \\ 0 & 0.087^2 & 0 \\ 0 & 0 & 0.0436^2 \end{bmatrix} \quad (5.13)$$

$$\hat{W} = \begin{bmatrix} 0.21^2 & 0 & 0 \\ 0 & 0.21^2 & 0 \\ 0 & 0 & 0.0436^2 \end{bmatrix} \quad (5.14)$$

The unicycle first orientation is given by the vector between the initial position and the desired way point. However, its desired trajectory along the deposition path is defined by the wire-tip projection at the image plane during the print. Therefore, its desired heading is computed at every iteration with its actual and desired position using the Matlab “atan2” four quadrant inverse tangent operation, which returns values between $[-\pi, \pi]$.

The wire feed is configured in a front feeding configuration (Figure 3.12) as shown in Figure 5.9. When a low quality wire is used during the deposition process, the angle deviation readings from camera 2 is simulated with a random angular velocity input such as,

$$\dot{\theta} = \omega_{wire}$$

which makes the feeding angle varies constantly along the trajectory and simulate the θ deviation.

After fusing the measurement and the prediction data in the update step of the EKF it must be transformed from the image plane to the inertial reference frame. This step is performed with the inverse camera perspective model and the homogeneous transformation from the robot base to the camera, which is detailed at section 5.1.2. It is important to highlight again that, it is only possible to make the reference from the image plane to the inertial reference frame with the knowledge of the distance z_c from the camera lens to the object being observed.

Chapter 6

Experiment and Simulation Setup

To develop the algorithms in this work a set of deposition experiments are performed using two WAAM robotics cells to deposit single-bead and multi-bead. A passive vision camera is used to acquire the data during the print, the video is recorded using the camera proprietary software and the robot joint state is acquired with the robot operating system (ROS).

6.1 First experiment setup

The first WAAM print setup consists of a robotic cell using CMT process for material deposition and a single CMOS monocular camera from Xiris Automation. Cold Metal Transfer (CMT) provides improved stability and lesser spattering, being both important features for Additive Manufacturing. A great advantage of CMT is the ability of providing a uniform bead profile and consequently decrease surface waviness. It also has a lower heat input decreasing part distortion during build up and better mechanical property chances, producing a higher string quality, which is expected for WAAM [24, 28]. Due to these properties the CMT is used as the deposition process.

The deposition trajectory is performed by a 6 DOF Motoman HP20 robot arm (Figure 6.1) and the welding equipment as well as the camera are both attached to the robot end-effector. The specifications of the HP20 robot arm are: 20 kg payload; ± 0.06 mm Repeatability; 1,717 mm H-Reach; 3,063 mm V-Reach; 280 kg Mass; NX100 controller providing best-in-class path planning and collision avoidance/arm interference prevention. The path planned is guided by the robot arm with a constant travel speed.

For acquiring the images of the bead, a regular welding camera from Xiris, model XVC-1000 was used (Figure 6.2) and configured at a distance of 285 mm from the substrate. The specification of the camera are: up to 55 FPS at 1280 (H) \times 1024 (V) pixels; lens with 16 mm focal distance; 6.8 μ m square pixel; 998 μ m exposure time.

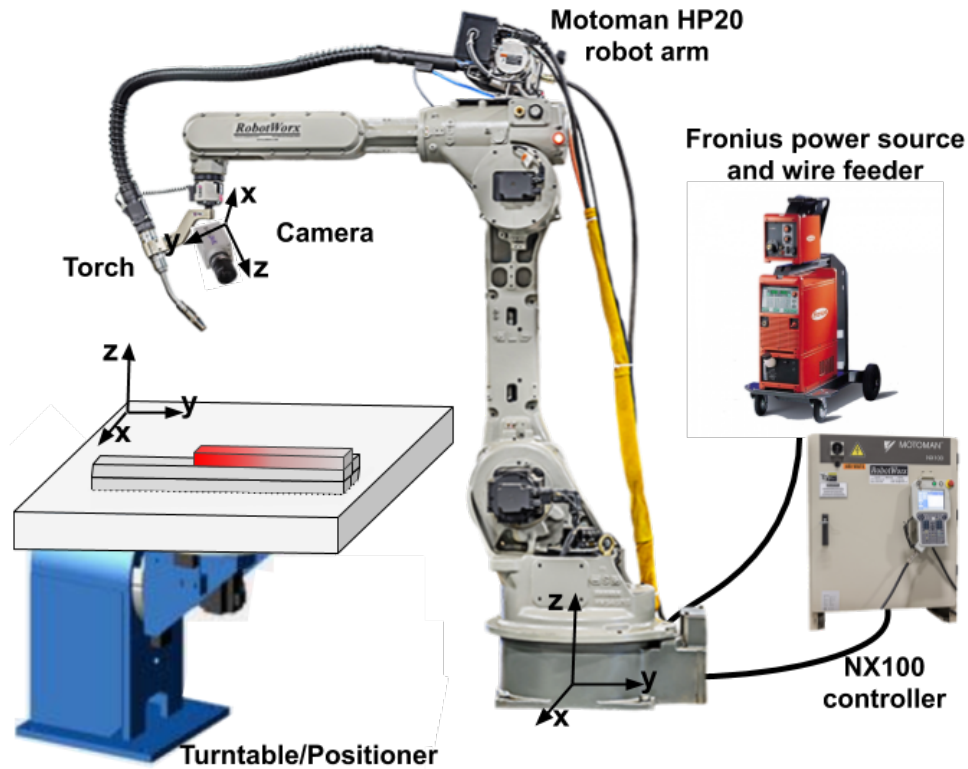


Figure 6.1: First WAAM setup configuration with Motoman HP20 robot arm, welding torch, camera, and NX100 controller [49].

However, any other camera with proper specification for capturing welding and deposition images by electric arc could be used.



Figure 6.2: Gray-scale camera from Xiris used during metal deposition.

Both welding torch and camera are attached to the robot arm, which guides them through the planned path with a constant linear velocity of $TS = 8 \text{ mm s}^{-1}$. The camera is assembled facing the substrate right after the metal pool, the light emitted by the bead in relation to the other features in the image is higher and this characteristics is used for highlight and extract the desired features. One set of single beads specimens are deposited during the deposition step can be seen in Figure 6.3, which is used to develop the bead geometry monitoring algorithm.



Figure 6.3: Single-bead specimens of the first experiment.

This experiment is used to test the response of noise reduction filters, the edge detect algorithm for WAAM using CMT and the development of the algorithm responsible of measuring the bead width with a passive camera. Therefore, the adequate smoothing filter and edge detection algorithm can be used in the online monitoring system. Table 6.1 shows the process parameters used, and the wire and the substrate chemical composition are described in Table 6.2.

Table 6.1: Process parameters of the first print experiment.

Characteristics	Value
Process	CMT
Wire feed speed	5.0 m/min
Travel speed	8.0 mm/s
Contact tip to work distance	15 mm
Gas Flow	15 L/m
Shielding gas	92% Ar and 8% CO ₂
Filler wire	Aristorod 55 _{1.2mm}
Reference current	165 A
Reference voltage	15.2 V

Table 6.2: Chemical composition of the wire filler and the substrate.

	C	Si	Mn	P	S	Cr	Ni	Mo	Cu
Wire filler	0.11	0.5	1.1	0.015	0.015	0.5	0.5	0.2	0.07
Substrate	0.16	0.222	1.05	-	-	2.5	-	-	-

6.2 Second experiment setup

The second deposition experiment is carryout with a set of equipment. The purpose is to print a set of single-beads and a multi-bead specimens, test the algorithm response to different deposition parameters settings and width variations during the deposition as well as the measurement of bead width in a multi-bead scenario. The WAAM robot cell deposits metal with a 6-DoF Kuka KR90 R2900 extraHA robot arm with $\pm 0.05\text{mm}$ repeatability (Figure 6.4) over a 2-DoF Kuka KP2 HV1100 positioning table. The torch and the camera (Figure 6.2) are attached to the robot end-effector. Both KR90 robot arm and KP positioner are managed by a KRC4 controller with the ArcTech and Robot Sensor Interface (RSI) software add-ons installed, all supplied by Kuka Robotics. The ArcTech provides tools to print with the welding power source, while the RSI is used to provide the robot joint positions.

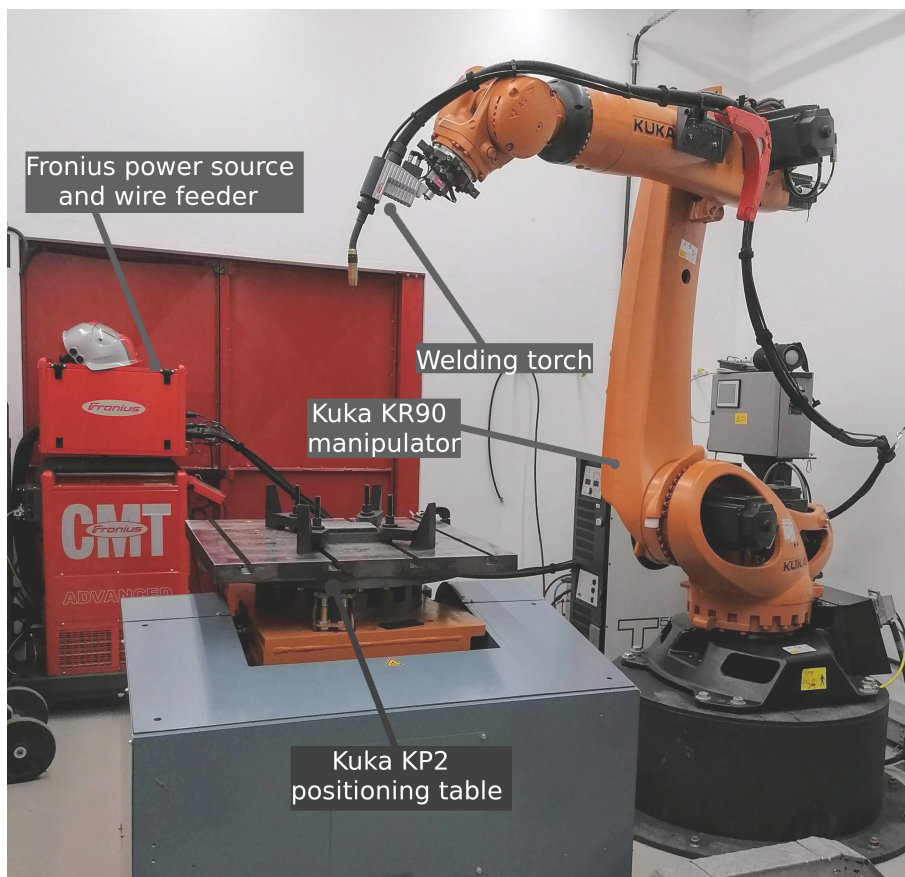


Figure 6.4: WAAM system with a Kuka KR90 robot arm, welding torch, Kuka KP2 positioning table, Fronius power source, and wire feeder.

The reference path is covered with constant travel speed (TS), defined as the linear velocity that the robot end-effector follows the path with respect to inertial coordinates. To monitor and perform image acquisition during the deposition, a Xiris XVC-1000 Weld Camera from Xiris Automation is used (Figure 6.5). The main specification of the camera are: up to 55 fps at $1280(\text{H}) \times 1024(\text{V})$ pixel

resolution, dynamic range 140+ dB, a lens with 35 mm focal distance, 6.8 μm square pixel, and 998 μs exposure time.

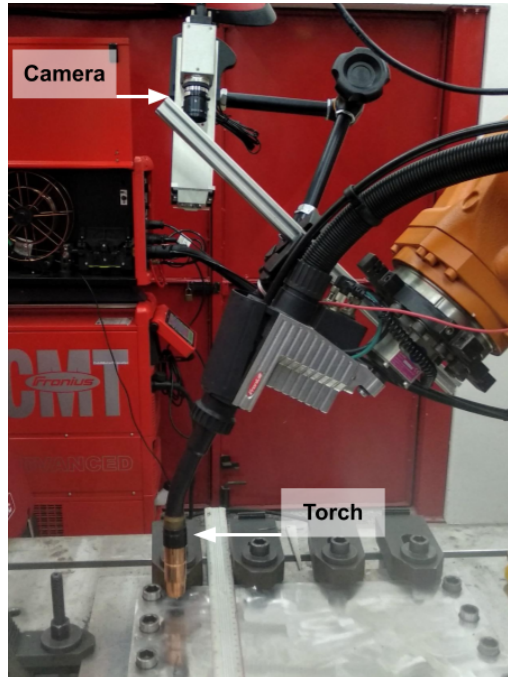


Figure 6.5: Xiris XVC-1000 camera and the welding torch assembly used in the second deposition setup.

Figure 6.6 shows the multi-bead deposition system. The color gradient used in the bead represents the temperature distribution during buildup, and shows how it affects the bead light emission. The camera is focused on the metal being deposited right after the molten pool. The light emitted by the bead in this area is higher due to its high temperature, and is used to detect the bead edges.

The specimens are printed on a substrate in a straight line along the end-effector y-axis. The torch and the camera are mounted in a top-view configuration facing the substrate and aligned with its z-axis (Figure 6.6).

The robot arm joint positions are acquired by a computer running the robot operating system (ROS ¹) Kuka package connected to a RSI network implemented on the Kuka robot controller. The ROS is an open source set of libraries and software tools that provide functionalities and conventions that facilitate the development of robotic applications. Considering that the robot kinematic chain is known and its joints positions are measured, it is possible to calculate the camera and the Cartesian welding electrode positions relative to the KR90 base by using a forward kinematic algorithm during the deposition. The vision-based algorithm is also coded following the ROS framework.

¹<https://www.ros.org/>

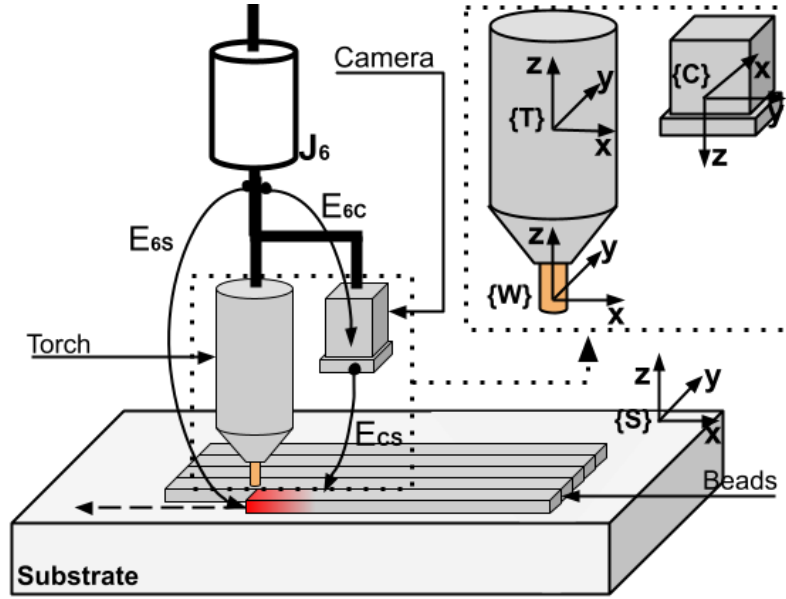


Figure 6.6: Schematic of the multi-bead deposition and vision monitoring setup. The camera, torch and wire are amplified with their coordinate systems.

6.2.1 Bead mapping

In the WAAM system with CMT, the wire is fed through the torch, and in most scenarios, their coordinate systems $\{W\}$ and $\{T\}$ have no attitude difference (Figure 6.6). Also, metal transference mode changes are not considered during the deposition. Assuming a symmetric geometric profile for the molten pool, the bead centerline is placed above the planned path during the deposition.

The bead centerline (C) is used to relate the bead width with bead position in the substrate, enabling quality management analysis by verifying the realized with the planned. The problem in the wire feeding is more common in a deposition system where the wire is fed independently with a predefined orientation, such as the GTAW and PAW. A deviation in the wire input angle increases the probability of part defects.

6.2.2 Bead samples

To validate the algorithm and its measuring accuracy, a set of experiments consisting of single beads deposition (Figure 6.7) and a layer (Figure 6.8) is carried out. The first specimen (A) uses a constant WFS, resulting in a continuous and uniform bead. For the remaining single beads, a step in the WFS is performed to study its influence on the beads' widths. Figure 6.7 and Table 6.3 show the single beads and the deposition parameters, respectively. All specimens are deposited with the same TS.

The specimens are transversely cut, following the lines (11 to 42 in Figure 6.7)

to produce specimens for macrography, then grinded, polished and etched with nital 2%. A Zeiss light microscope measures the width with the AxioVision SE64. The results of the vision and physical measurements are compared and shown in Section 6.



Figure 6.7: Samples of the second single-bead experiment with constant and varying wire feed speed (Table 6.3).

Table 6.3: Travel speed and wire feed speed used for the second single-bead experiment.

Samples	WFS_{init}	WFS_{final}	TS
A	6	6	6
B	4	6	6
C	8	6	6
D	4	8	6
Units	$m\ min^{-1}$	$m\ min^{-1}$	$mm\ s^{-1}$



Figure 6.8: Five bead layer sample of the second experiment. The deposition of all bead are performed in the same direction.

6.3 Third experiment setup

Another experiment setup is performed using a similar setup to the one presented at Figure 6.2 and Figure 6.6, a infrared camera is used in this new setup in addition with the already used items. The main objective of this test is to acquire data with an HDR camera from Xiris and an IR camera from NIT with a topside view configuration, and then use the same algorithm developed to extract the bead width information and the centerline in reference to the inertial coordinate while printing. IR camera main specifications used in the camera perspective model are described in Table 6.4.

Table 6.4: NIT Tachyon 16 IR camera main specification

Tachyon 16k camera	
Array format	128 × 128
Pixel size	50 μm × 50 μm
Focal lens	32 mm
Maximum frame rate	2000 fps
Spectral range	MWIR (1.0 a 5.0 microns)
Peak wavelength of detection	3.7 μ

The setup used of the current experiment is detailed at Figure 6.9, the HDR and the IR cameras were both positioned at a topside view to capture the same deposition characteristics.

The bead width estimation is performed in the IR camera for single-bead deposition, in the multi-bead scenario the bead width is estimated using both IR and HDR cameras. In this experiment single-bead, multi-bead, and a 5 layer pad is produced, they are shown at Figures 6.10 and 6.11. Table 6.5 detailed the main information about the third experiment, the bead width estimation is expected to be within the 9.30 to 9.59 mm range, which is also the measurement reference to be achieved by the vision-based monitoring system. The step-over distance used is according to 0.667 w , where w is the bead width. Variations in the width estimation are expected due to the noise present in the deposition process and detailed in Table 6.5. The multi-bead specimen (Figure 6.10) have the following width in its 4 sections: (i) 9.32 mm ; (ii) 14.84 mm ; (iii) 21.11 mm ; (iv) 27.10 mm , these measurements are referred to the first bead deposited, which has the longest length, to the set of 4 beads.

6.4 Simulation setup

The third setup is used inside a simulation environment configured at Matlab. It is configured such as the deposition of single-beads is performed using a 6-DOF robot

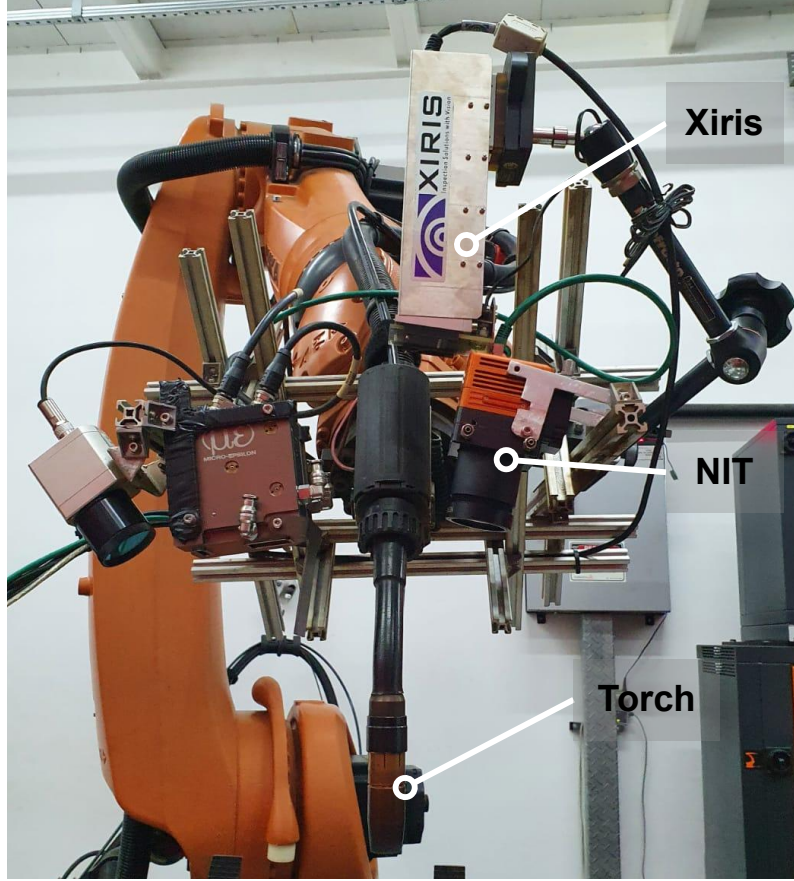


Figure 6.9: The sensors setup used in the third experiment.

Table 6.5: Third experiment deposition information.

Deposition information	Value
Process	CMT
Travel speed	11.0 mm s^{-1}
CTWD	10.0 mm
Expected bead width	$9.30 \text{ to } 9.59 \text{ mm}$

arm that guides the torch and an independent wire feeder. This step is used to simulate the influence of the wire deviation, which is a result of the wire deflection during the print as described in section 3.3. The deflection is simulated by a feeding rotation around the y-axis of the wire feeder coordinate system that result in lateral deviations along the trajectory. The proposed setup is described in Figure 5.9.

The welding torch is configured facing the substrate surface, with its z-axis orthogonal to the deposition plane. The wire feeder is assembled in a front configuration (see Figure 3.12). Camera 01 is assembled facing the substrate to capture the bead being deposited, which is setup to simulate the bead centerline measurement. Camera 02 is configured in a position to capture the wire deviation (θ_{wd}) as in the work performed by [76]. Its image view and measurement is simulated in according with Figure 3.14 and Figure 3.15.



Figure 6.10: Single-bead and multi-bead specimens, where the passes of the multi-bead specimens have different length.

The robot in the simulation is setup following the datasheet of Kuka KR90 2700, similar to the robot arm used in the second experiment (Figure 6.4). The camera is configured using the same specifications of the Xiris XVC-1100 mentioned previously, a zero mean Gaussian noise with a variance of 0.4 pixels for the wire feeding angle estimated for camera 2, and a zero mean Gaussian noise with 5 pixels of variance for the centerline identified is considered in the image plane from camera 1. These cameras configuration are detailed in Figure 6.12, where a sided-view representation of the system with some parameters used in the simulation is shown. The KR90 2700 robot arm used for the simulation performed in Matlab is shown at Figure 6.13.

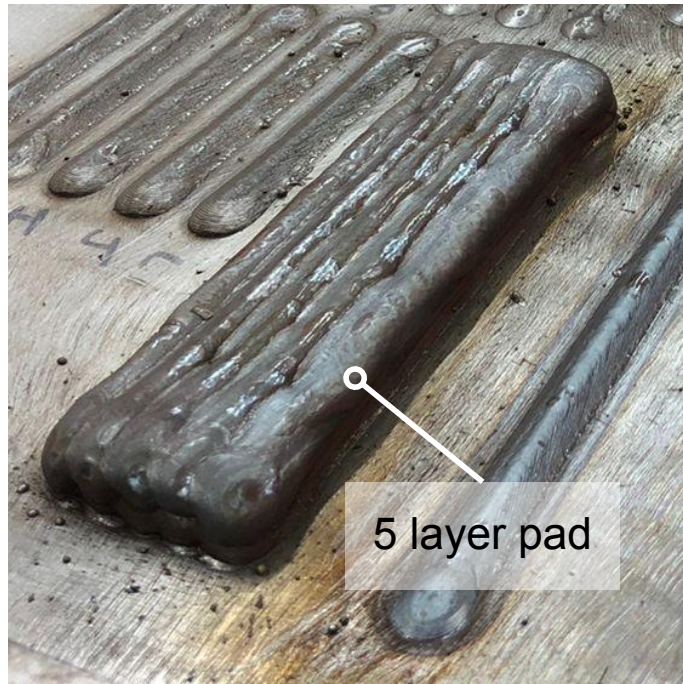


Figure 6.11: Third deposition experiment five layer pad.

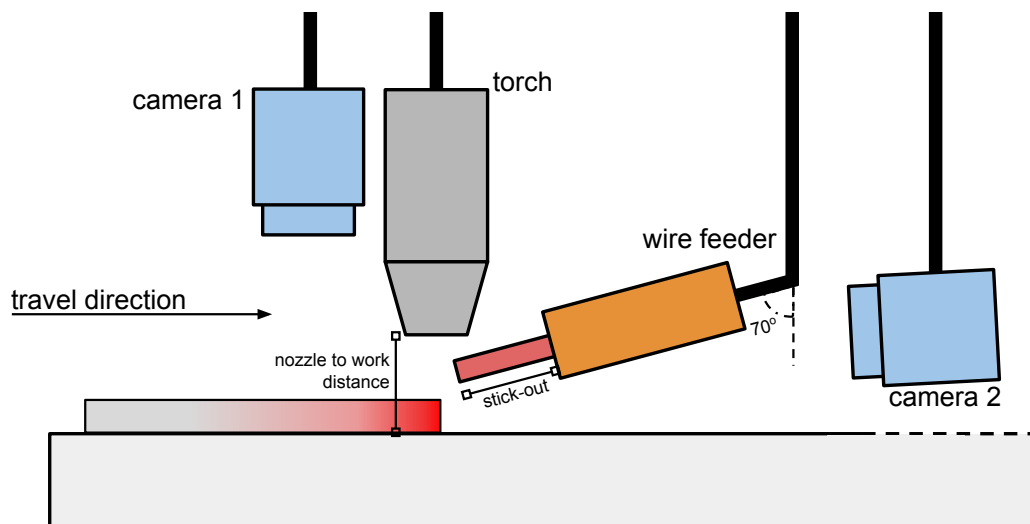


Figure 6.12: Side view of the deposition system simulation with the stick-out, distance from torch to the substrate and the wire feeder angle highlighted.

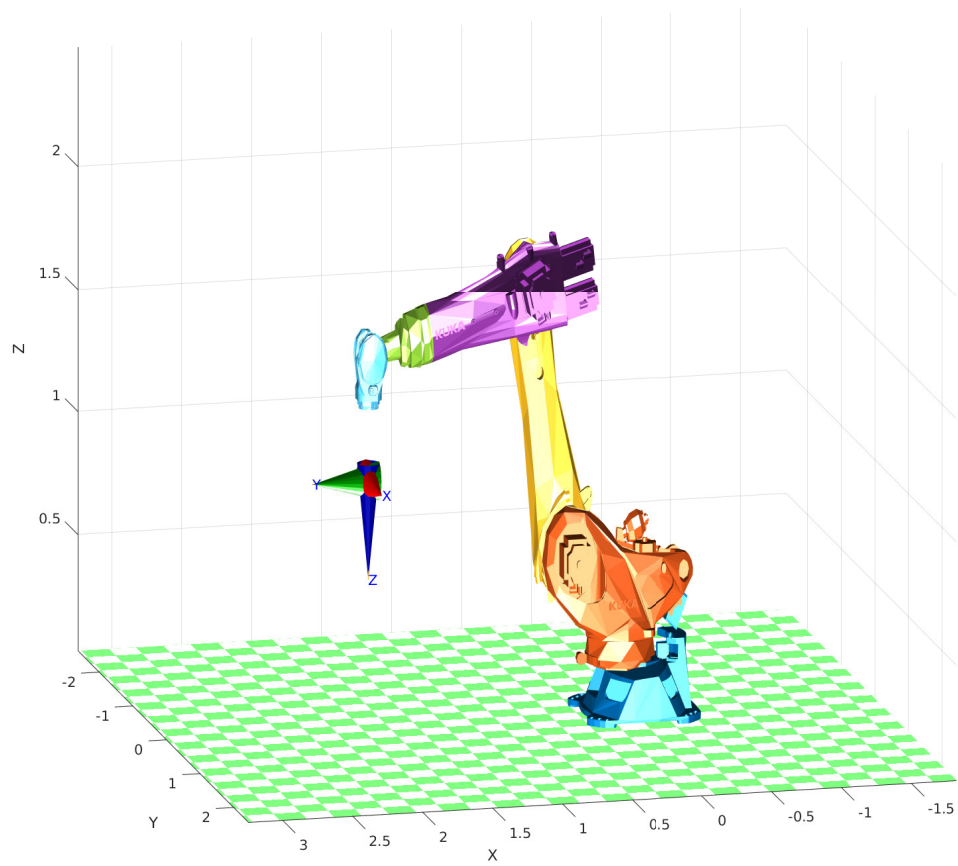


Figure 6.13: 3D schematic of the Kuka KR90 2700 used in the simulation.

Chapter 7

Results and Discussion

This section details the results obtained from the three deposition experiment performed with the vision-based algorithm developed for passive vision sensors. Followed by the results for the test of the smoothing filters and edge detection algorithms for the images acquired with the passive vision sensors. Next the bead width and centerline measurement are presented for both experiment print configuration. The centerline estimation is carried out from the second to the last experiment presented. All deposition is performed using CMT.

7.1 First experiment

The first experience performed has the focus on testing the performance of the smoothing filters and edge detectors and confirm based on the references an approach to be used in the development of the monitoring system. An initial bead width measurement experiment is also presented, however without the addition of specific filtering to increase the robustness of the monitoring system.

7.1.1 Width measurement of single-bead deposition

The images acquired from a single-bead deposition is used to test a set of noise reduction filters. In Figure 7.1 the result of the test is described, is it noticed that the median filter in this scenarios have a higher impact in the sharpness of the image and also has a higher CPU cost when compared with the Gaussian filter. Since the image sharpness is important for a accurate measurement and the CPU cost impact the online performance of the algorithm, therefore the Gaussian filter is used in the noise reduction step.

After defining the region of interest (ROI), the performance of the edge detection algorithms are tested, the edges detected of the bead being deposited with each algorithm are shown in Figure 7.2. It evidences the results obtained with each

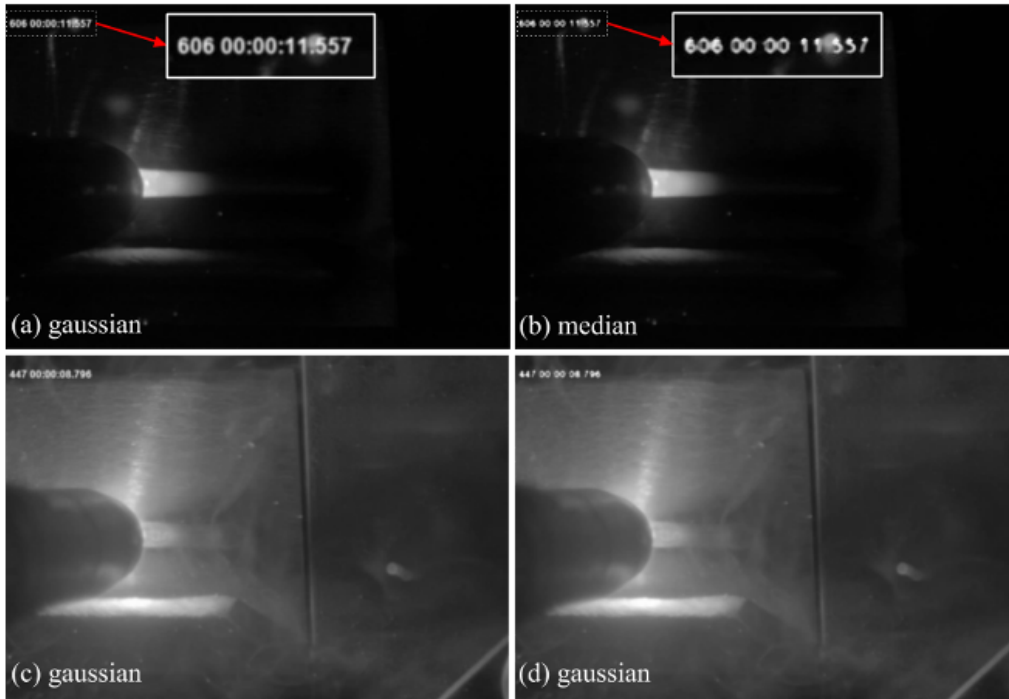


Figure 7.1: Median and Gaussian filters results in WAAM. Where low and high light scenarios are analyzed for both filters [18].

algorithm, with Canny edge algorithm having the best edge identification of them. A similar conclusion is reached by MA *et al.* [46], where the authors compared the Prewit, Roberts, Kirsch and Canny edge detection algorithms for welding images.

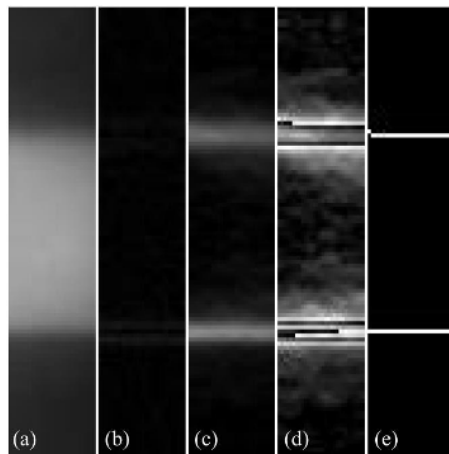


Figure 7.2: Edges of the bead (a) detected inside the region of interest using Laplacian (b), Sobel (c), Schar (d), and Canny (e) edge detection algorithms [18].

The noise reduction and edge detection algorithms tested performances are described in Figure 7.3. A first measurement experiment with the data acquired from the camera is also performed in COUTO *et al.* [18]. The first measurement test (Figure 7.4) is performed after the line identification and a simple mean filter, which in further tests showed little robustness to deal with the WAAM non-linear

noises.

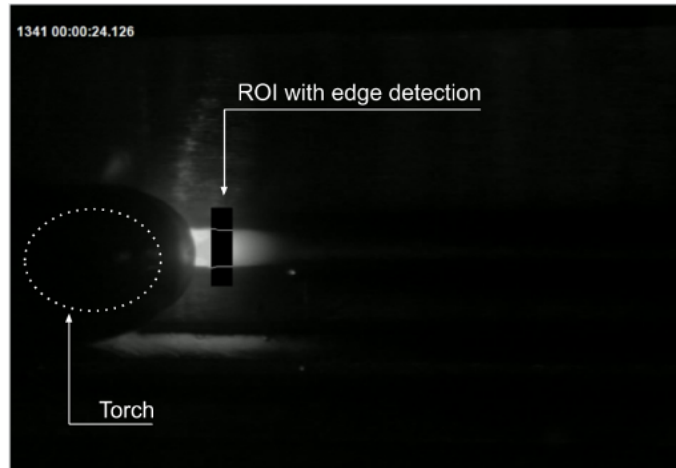


Figure 7.3: Video of deposition using CMT with the region of interest [18].

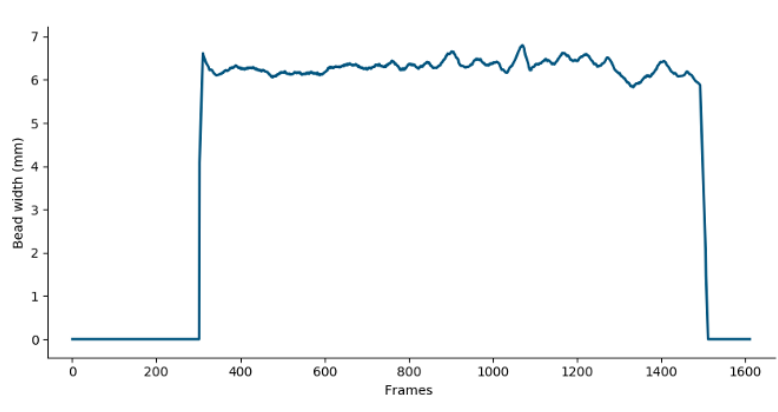


Figure 7.4: Bead width estimation of the first experiment with the usage of a mean filter [18].

To improve the reliability of the measured width and attenuate the noise it is used a low-pass band or moving average filter, the result is described in Figure 7.5. The information is mapped and recorded at every frame of the print and the measurement is performed constantly with low variance. The median and low-pass band filter are represented by the red and blue line respectively.

A comparison between the mean value of both filters and a manually measurement with a software, shows a deviation of 1%. The mean value of the bead width from both filters data is 6.27 mm and 6.24 mm when measured manually (Figure 7.6).

Since hough-lines identify multiple lines due to a low signal-to-noise ratio commonly found in WAAM videos using passive vision, another filtering step is used in this experiment, it considers only the parallel lines for the bead width calculation. However, to measure based in the parallelism of the lines showed little effectiveness

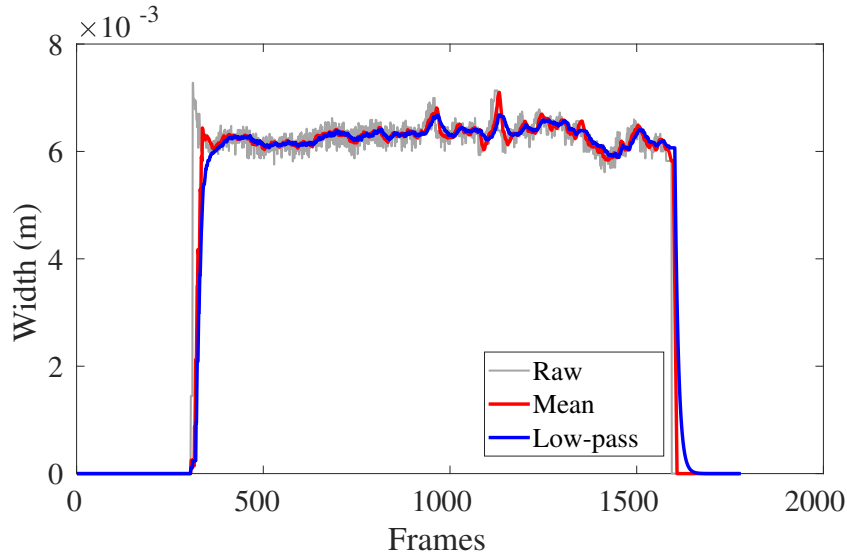


Figure 7.5: Bead width measurement with low-pass band and moving average filtering [49].

in some deposition with low noise-to-signal ration and the rework of the filtering step is performed for the second experiment.

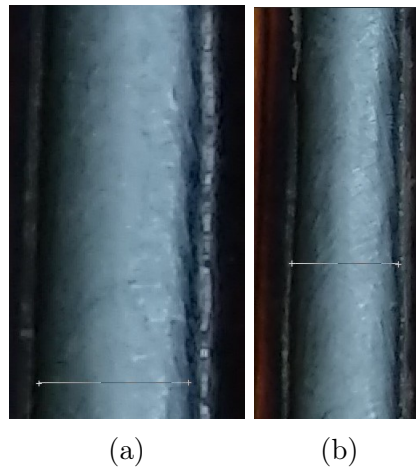


Figure 7.6: Single bead width measured manually, where (a) and (b) are respectively the first and second position measured of the single-bead [49].

7.2 Second experiment

In this section, the results of single-bead and multi-bead depositions carried out with the second WAAM system are described. The specimens are used to test the bead geometry measurement vision-based algorithm and the bead placement estimation for WAAM using CMT.

7.2.1 Segmentation analysis

With the acquisition of new data, it was perceived that the estimation performed under a high noisy scenario had a higher variance, failing in the feature identification step constantly. Therefore, an analysis was performed to increase the reliability of the width estimation. A comparison of the width estimation are performed with a fixed and an adaptive segmentation parameters and also without the segmentation is shown in Figure 7.7. In a low noise scenario, there are no significant differences between the strategies tested (Figure 7.7b). However, in a high noisy scenario, the measurement presents low variance readings only using an adaptive parameter (Figure 7.7a).

Therefore, for all the experiments performed in this work the adaptive threshold is used to do the segmentation of the intended feature, and improve the reliability of the vision-based monitoring system.

7.2.2 Single-bead geometry measurement and estimation

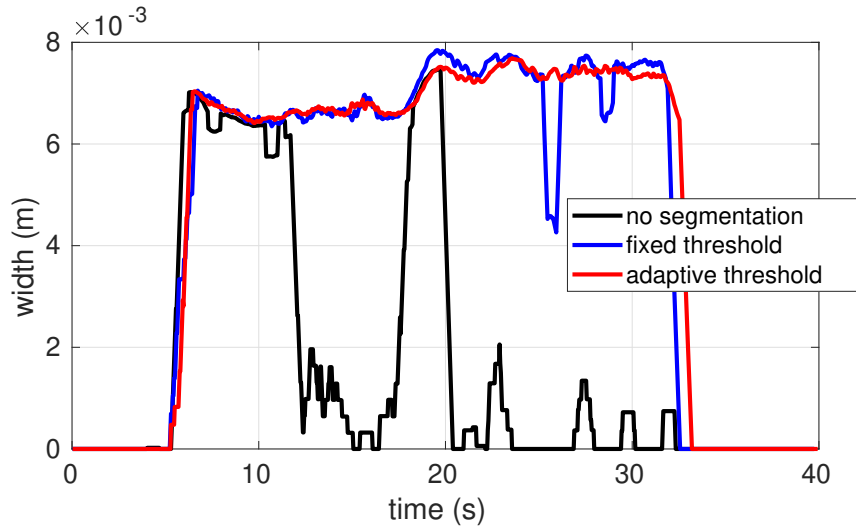
Figures 7.8 to 7.11 show all the beads' width estimation. The small overshooting at the beginning of Figures 7.8 and 7.10 is expected because more metal is deposited until the robot starts moving and reaches the desired linear velocity. Considering all measurements performed in the first and second halves of the plots through vision, the vision-based algorithm constantly monitored the deposition with a low variance outcome. The mean of the estimated widths for each specimen are shown in Table 7.1. It is important also to consider that the vision monitoring system gives much more information when compared with the macrograph measurement since it provides the bead width through its full extension.

Table 7.1: Measurements performed in the first and second halves of the plots.

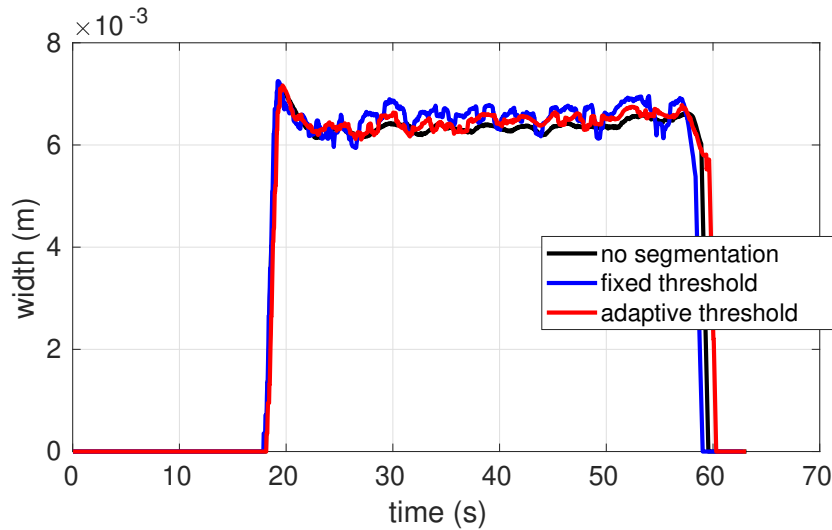
Specimen	1st half	2nd half
A	6.9	7.0
B	6.4	7.1
C	8.5	6.9
D	6.2	8.8
Unit	<i>mm</i>	<i>mm</i>

7.2.3 Multi-bead width measurement

The developed algorithm also is used to estimate the beads' widths in a 5-bead layer (multi-beads layer), as shown in Fig. 7.12. One of the bead edges identified is sharper than the other because it intersects the substrate or last layer deposited.



(a) Monitoring in noisy scenarios.



(b) Monitoring in low noise scenarios.

Figure 7.7: Width monitoring plot using different strategies.

For comparison, the other edge that overlaps the neighbor bead is more difficult to identify, because this edge is the intersection of two beads and the measurements show a higher noise incidence. This results in width variations, and the edge identification becomes a challenge.

It is possible to identify the width variation when observing Figure 7.12. Bead 1 and 2 presented a higher width, but when considering the increase numbers of pass deposited the width estimated tends to decrease and stabilize within a range, which are the behavior experienced in beads 3, 4 and 5. No width estimation pattern based on the indirect deposition parameters and the single-bead width estimation is intended to be achieved in the current work.

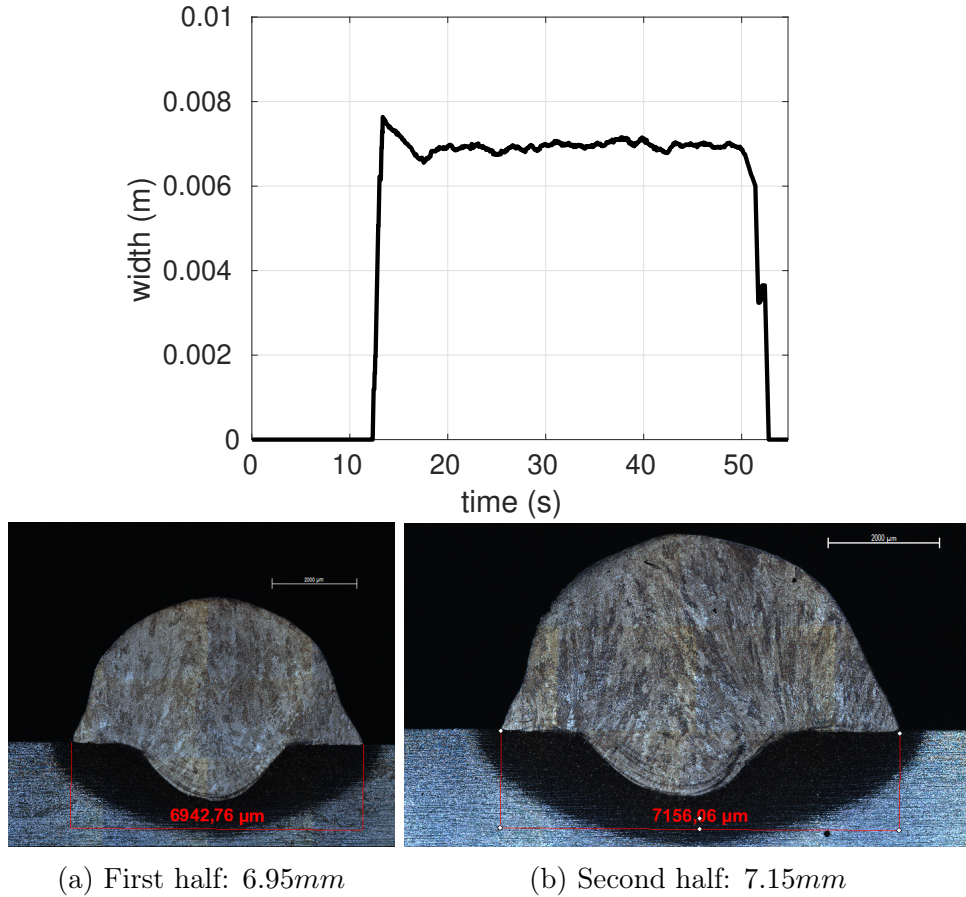


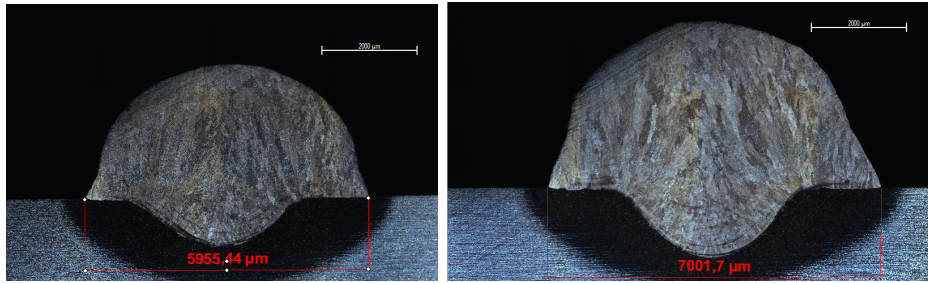
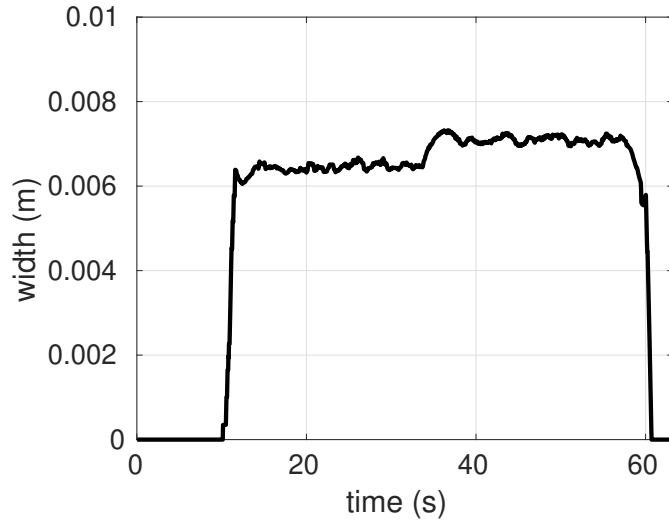
Figure 7.8: Constant WFS, Sample A [17].

7.3 Third deposition experiment result

This section contain result from both HDR and Infra-Red camera. They are capturing the bead formation right after the molten pool and performing the bead width estimation in real-time. The multi-bead estimation test are performed with both cameras, however, the bead placement estimation is performed only using the IR camera since it is integrated in ROS. The single-bead measurement is performed only for IR camera.

For the multi-bead deposition of Figure 6.10 the result contains the bead width information for every pass with both cameras. The purpose is to test the estimation and check the width variation for every bead observed. Figure 6.11 pad is used to test again the width estimation and also the bead centerline placement in real-time, the reading is performed on the last layer. It is also verified if bead placement deviations can be perceived during the monitoring.

The expected bead width variation for the estimation performed is detailed in Table 6.5, where the measurement was performed in a single-bead specimen for the calibration of the parameters.



(a) First half: 5.95mm

(b) Second half: 7.00mm

Figure 7.9: Varying WFS, sample B [17].

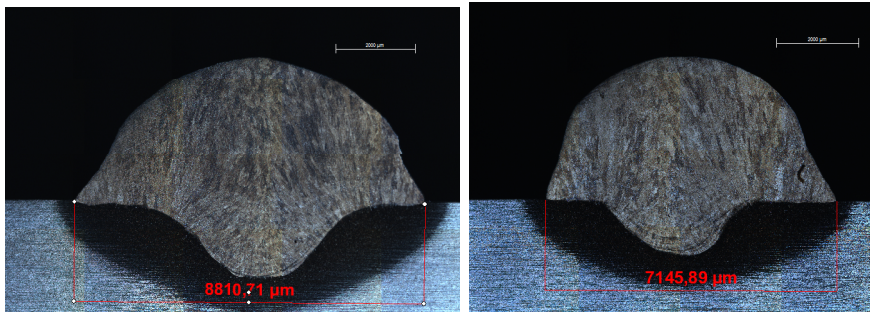
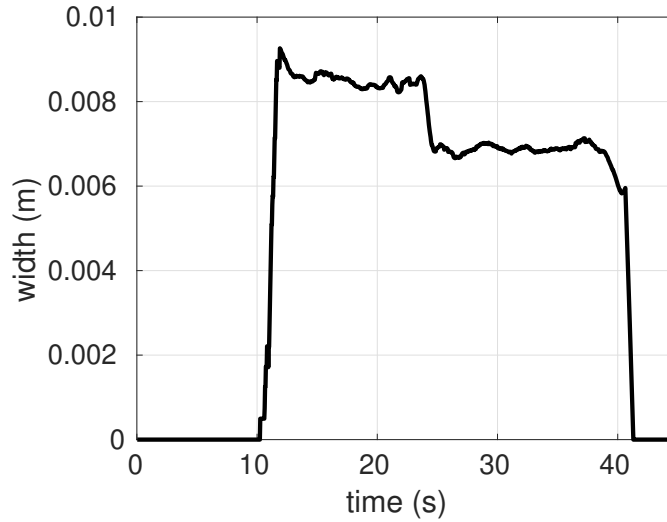
HDR passive vision camera

The results of the experiment using Xiris HDR camera are presented from Figures 7.14 and 7.15. And the detailed information of the estimation is shown in Table 7.2 and 7.3. The mean value is computed at the steady period of the monitoring because the start and end a highly noisy and also the monitoring do not stop when the electric arc turn-off.

Examples of images acquired with the Xiris HDR camera are presented at Figure 7.13, where it is possible to see the noise and also variation in the bead width observed during the monitored, well exemplified at Figures 7.13a and 7.13b.

Table 7.2: Bead width estimation values for the multi-bead deposition using Xiris HDR Camera.

Samples	Width estimation
Bead 01	9.95
Bead 02	9.55
Bead 03	8.77
Bead 04	8.93
Unit	mm



(a) First half: 8.81mm

(b) Second half: 7.14mm

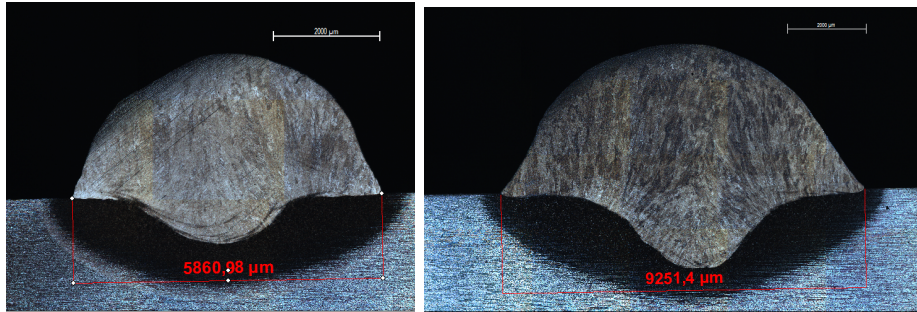
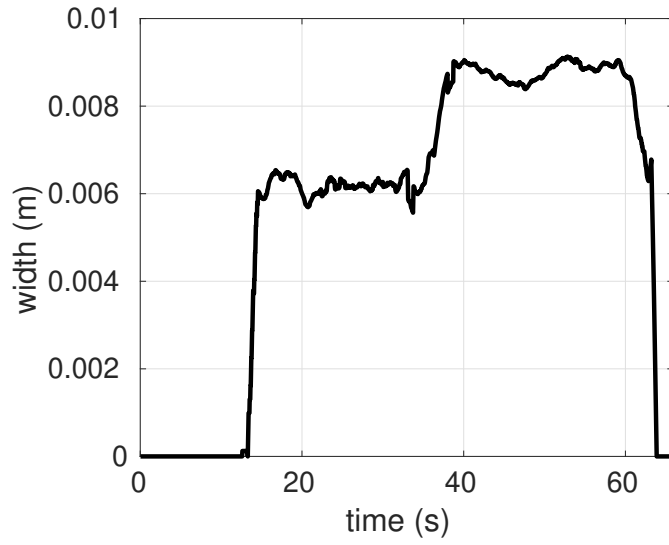
Figure 7.10: Varying WFS, sample C [17].

Table 7.3: Bead width estimation values for the layer 5 of the pad deposited using Xiris HDR camera.

Samples	Width estimation
Bead 01	9.79
Bead 02	9.15
Bead 03	9.05
Bead 04	8.97
Bead 05	8.48
Unit	mm

IR passive vision camera

The width estimation results of the experiment using NIT IR camera are presented at Figures 7.19 and 7.20, where the estimation graph for the multi-bead and PAD (layer 5) are detailed. The width value is shown at Table 7.4 and 7.5. The mean value is computed at the steady period of the monitoring because the start and end of the deposition contains a lot of noise that might be accounted without necessity,



(a) First half: 5.86mm

(b) Second half: 9.25mm

Figure 7.11: Varying WFS, sample D [17].

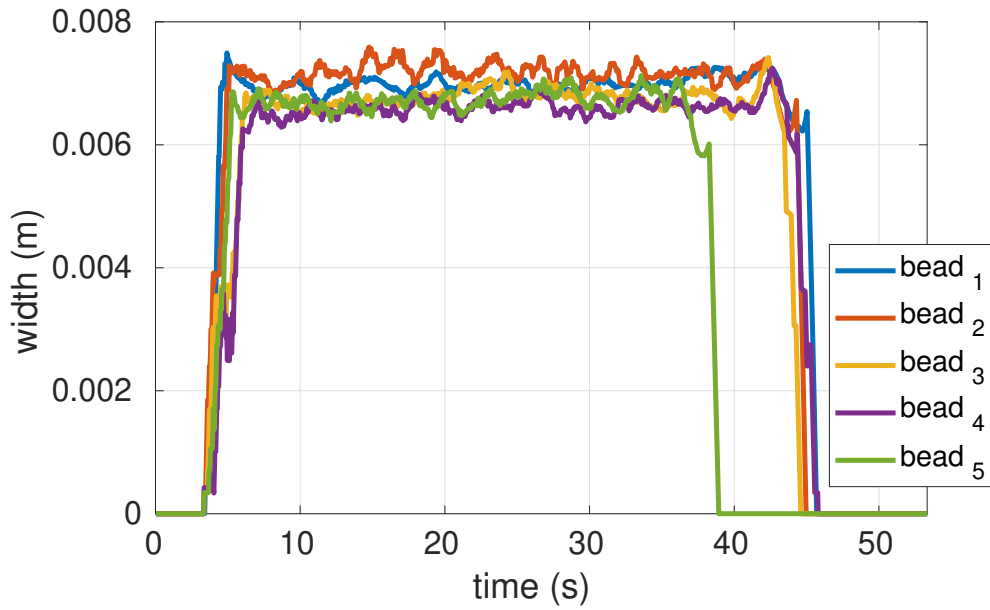


Figure 7.12: Multi-bead width monitoring at current layer [17].

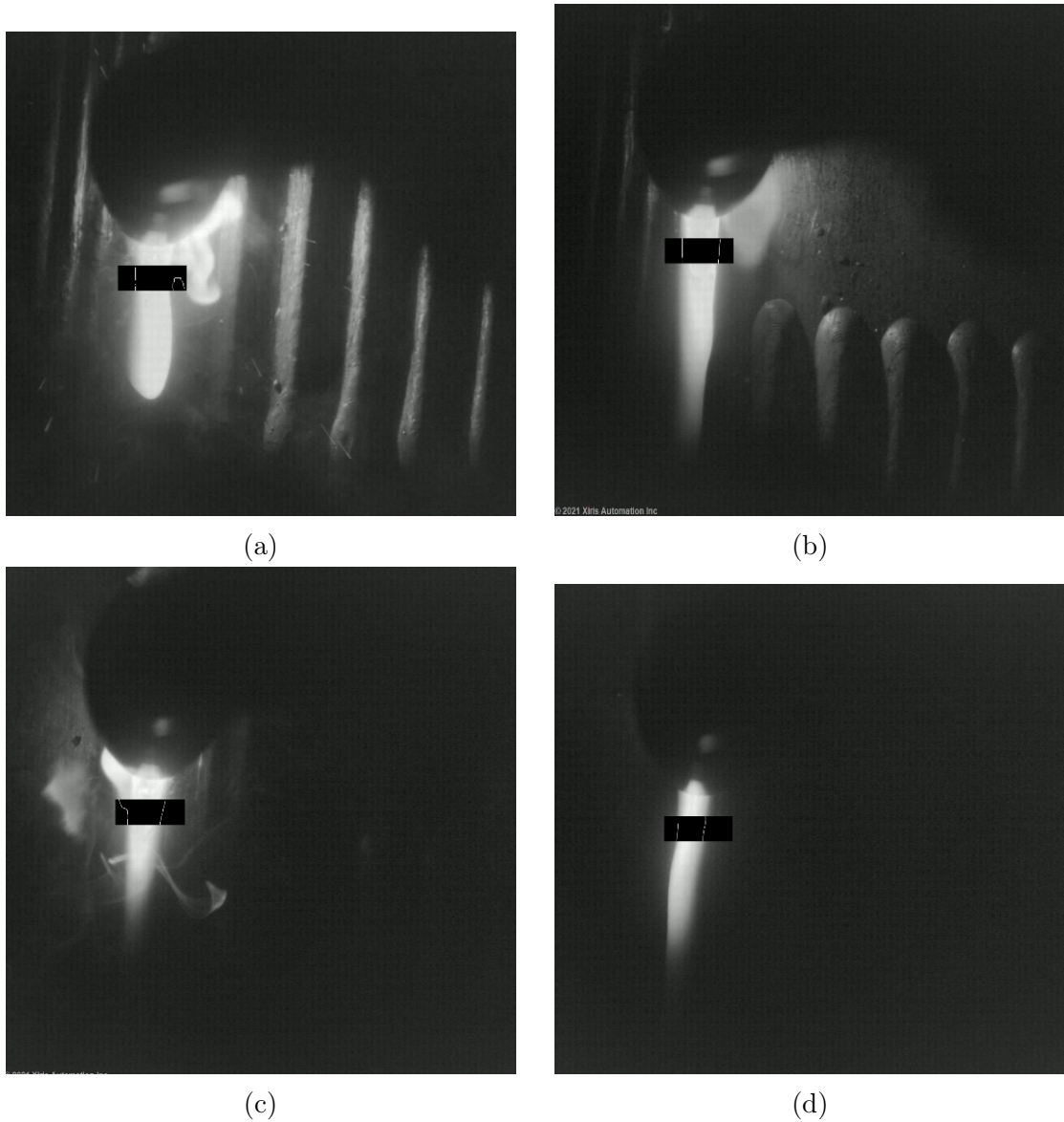


Figure 7.13: Frames captured during the layer 5 deposition of the pad.

e.g. a bead ghost continue present at NIT image even after the deposition stops as shown in Figure 7.16.

Some frames captured from the multi-bead deposition and the pad deposition are shown at Figure 7.17 and 7.18 are present to exemplify the characteristic of the data acquired during the monitoring. The images from the IR camera are less susceptible to noise variations when it is compared with the images from Xiris HDR camera as already shown at Figure 2.14.

The estimation performed in a single bead, bead 1 of the multi-bead specimen, shown constant monitoring but with higher variance when compared with Xiris at previously experiments. Even so, the monitoring system is able to monitor constantly the characteristics for every bead deposited for both multi-layer and pad deposition experiment. Also a function to monitor the characteristics only when the

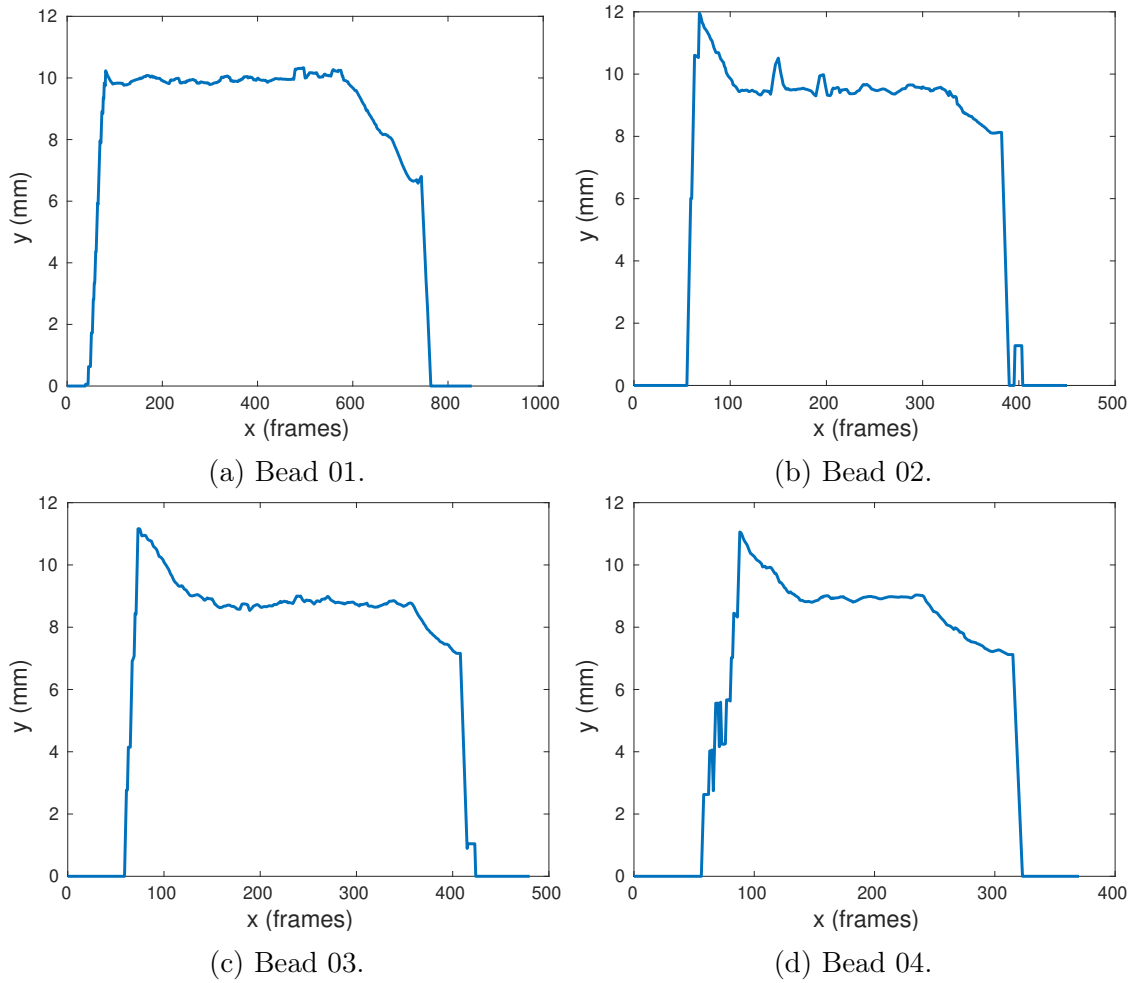


Figure 7.14: Bead width estimation for the multi-bead deposition using HDR camera.

arc is on can be added to avoid the width estimate acquisition in the areas where the monitoring presented a lower signal-to-noise ratio, therefore avoiding unnecessary noises.

Table 7.4: Bead width estimation values for the multi-bead deposition using NIT IR camera.

Samples	Width estimation
Bead 01	10.23
Bead 02	10.05
Bead 03	9.76
Bead 04	10
Unit	<i>mm</i>

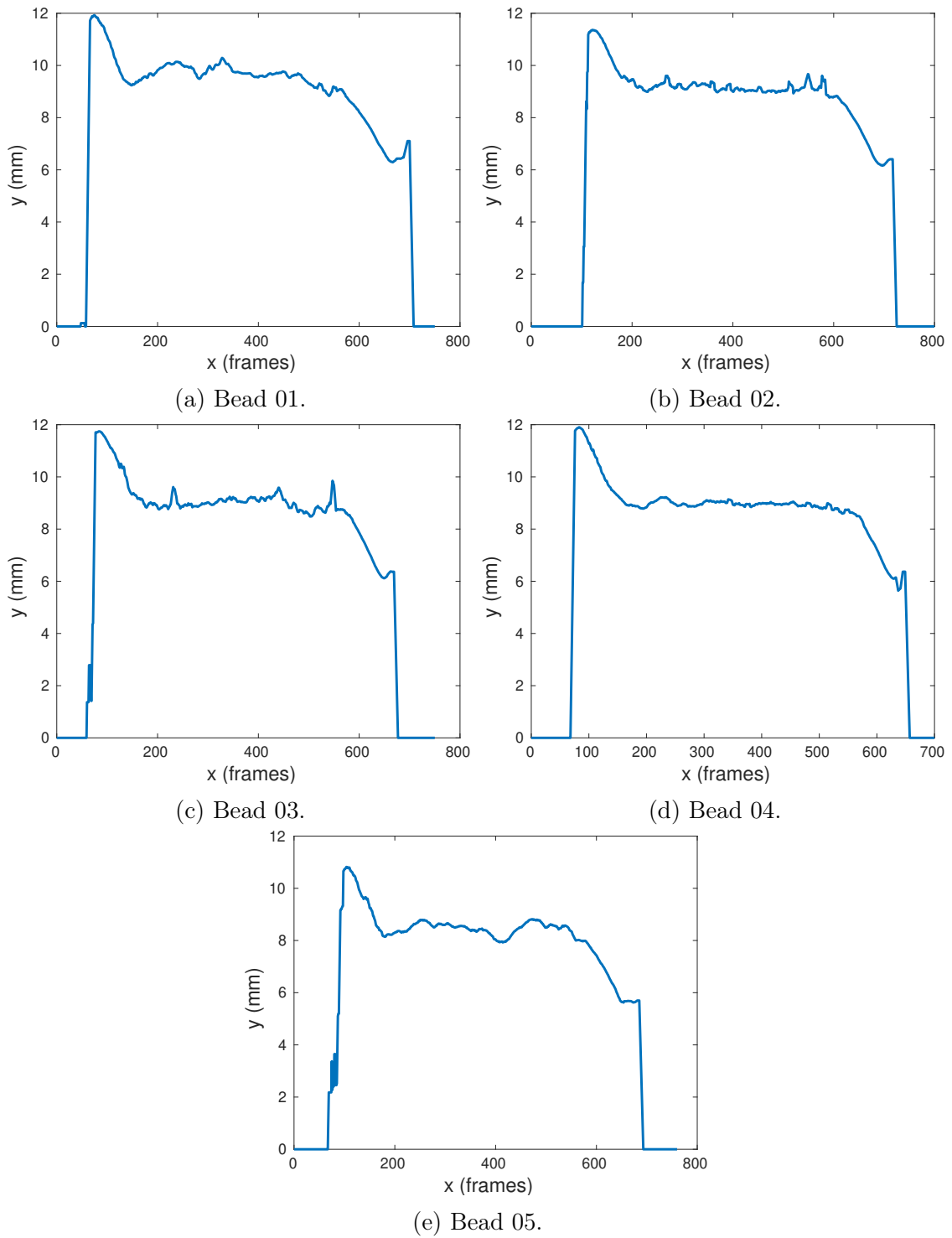


Figure 7.15: Width estimation for every bead of bead layer 5 using HDR camera.

Bead placement with the HDR camera

In this section is presented the result obtained by the current experiment for the multi bead deposition. It is presented the robot arm trajectory for every single-bead deposited, and the bead centerline localization in the x-y plane for the inertial coordinate (robot arm base).

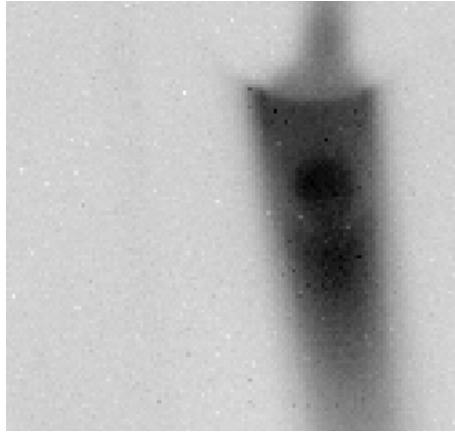


Figure 7.16: Bead ghost present at the IR image even after the end of the deposition.

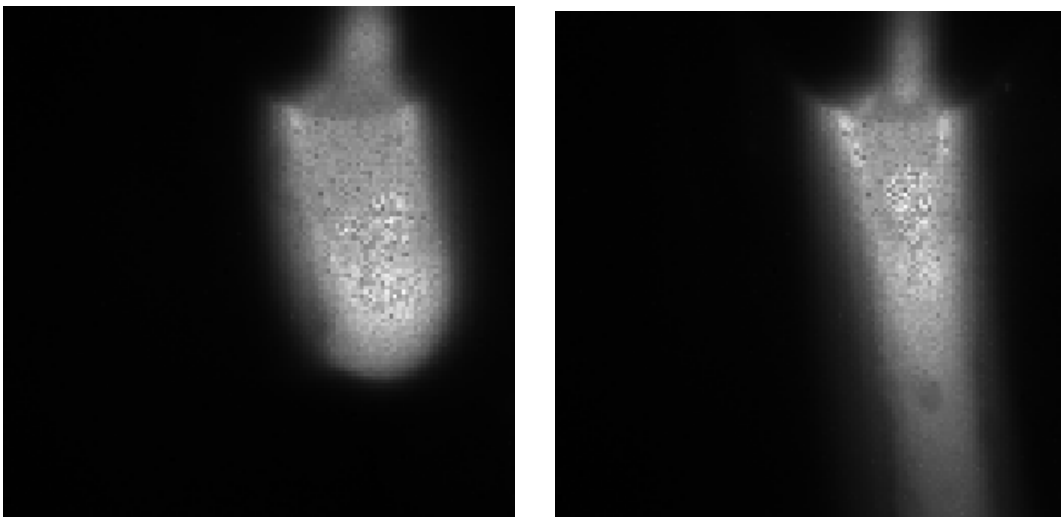


Figure 7.17: Specific frames captures from the multi-bead 4th pass.

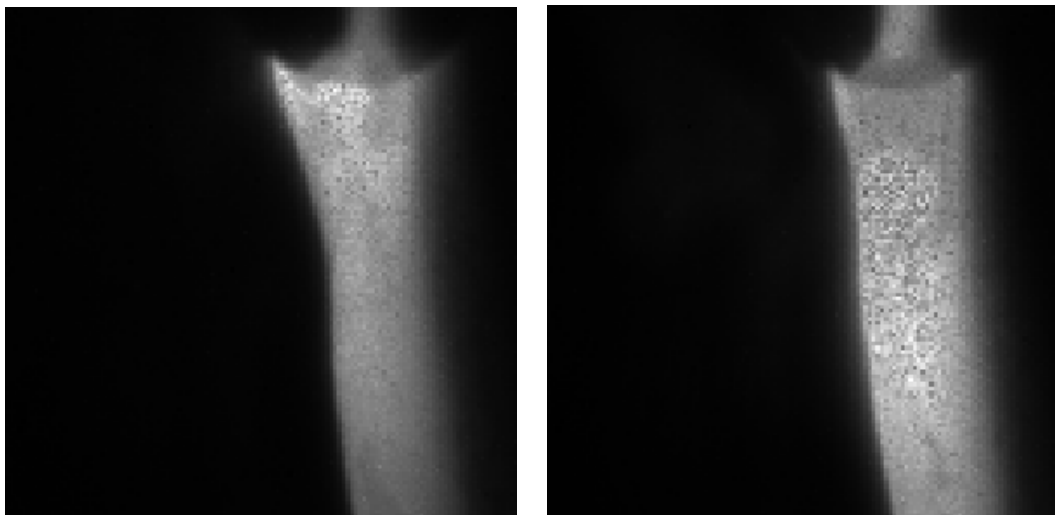


Figure 7.18: Specific frames captures from the pad last layer.

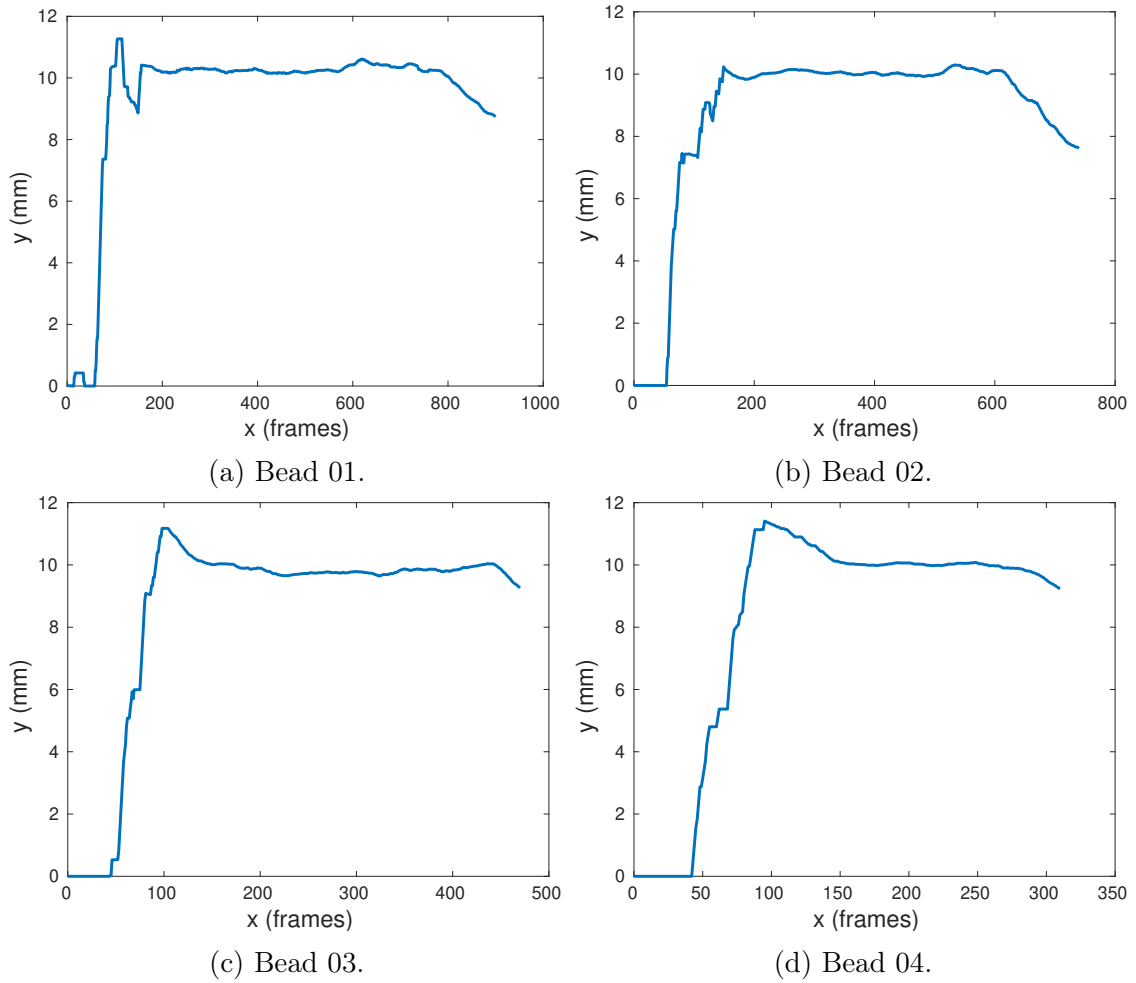


Figure 7.19: Bead width estimation for the multi-bead deposition using the IR camera.

Table 7.5: Bead width estimation values for the layer 5 of the pad deposited using NIT IR camera.

Samples	Width estimation
Bead 01	10.07
Bead 02	10.05
Bead 03	9.73
Bead 04	9.75
Bead 05	9.63
Unit	<i>mm</i>

It is possible to see that the estimation is noisy but was constantly monitored during the deposition process. As expected, the noise affects more the readings at the start and end of every bead. For a more accurate estimation another filtering solution should be developed to prevent abrupt variations in the placement estimation as the ones presented at Figure 7.22. The trajectory performed by the robot arm is also presented individually for each bead at Figure 7.21.

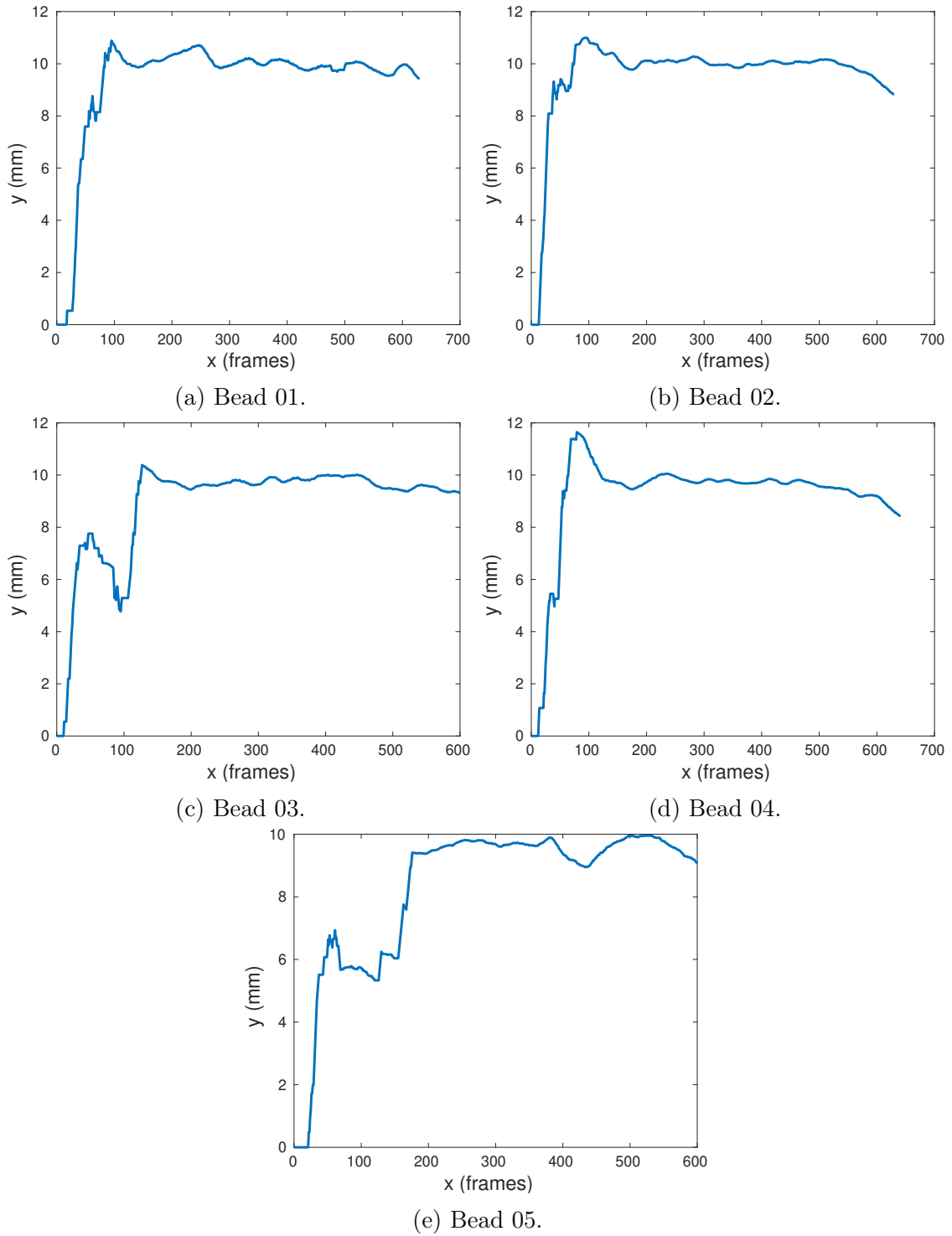


Figure 7.20: Width estimation for every bead of pad (layer 5) using the IR camera.

7.4 Simulation experiment result

In this section, it is presented the results of the Matlab simulation. The proposed estimation is performed in two scenarios: (i) linear trajectories; (ii) circular trajectories. The wire feed varies along the trajectory to simulate a low quality wire, and the robot manipulability is computed at the beginning of each trajectory.

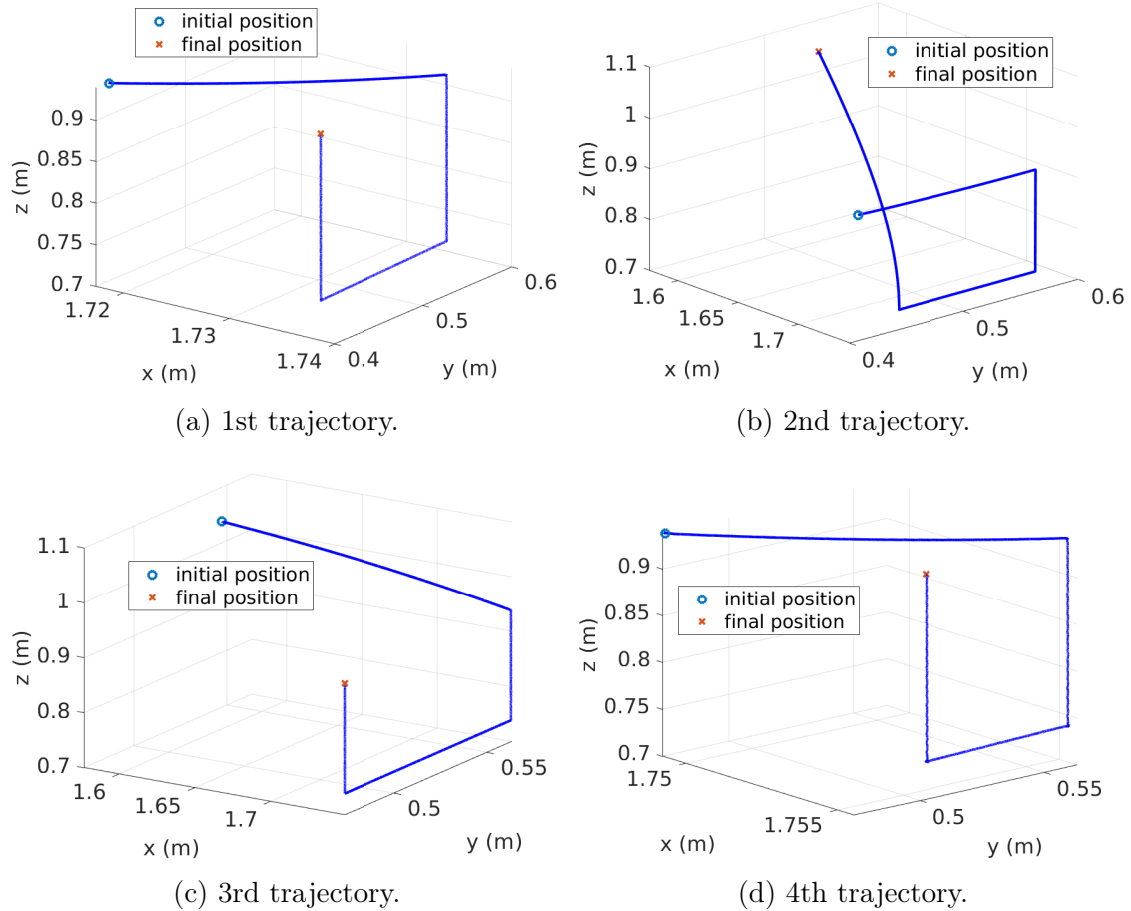


Figure 7.21: Trajectory performed by the robot arm during the multi-bead experiment.

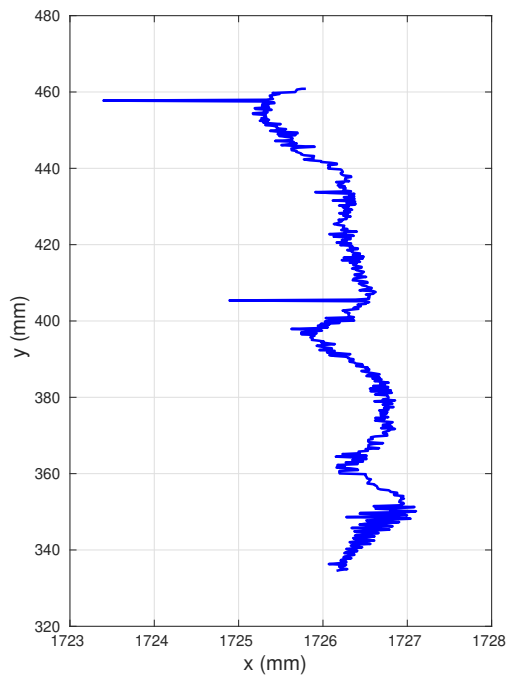
7.4.1 Linear trajectory deposition

The robot arm manipulability is computed to ensure that there is no singularities in the trajectory that could disturb the desired characteristic estimation, it is shown at Figure 7.23.

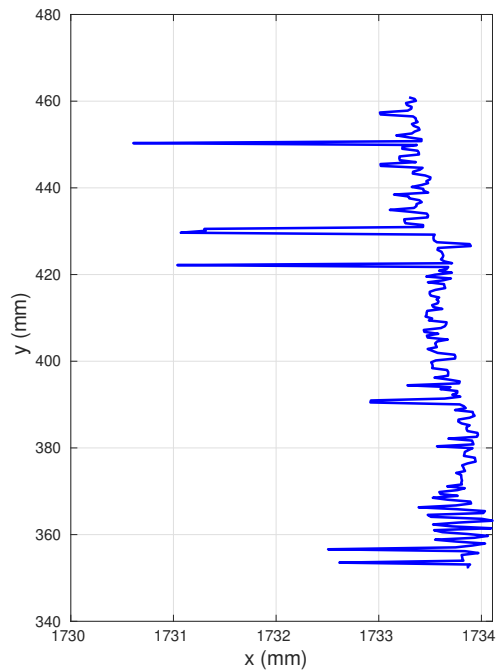
wire orientation: varying

The planned and performed bead placement is shown in Figure 7.26, where it is possible to notice the influence of the deviation in the wire feed angle along the deposition path shown at Figure 7.25. The orthogonal deviation from the path planned caused by the wire feed angle is shown at Figure 7.27. Both Runge-Kutta and Euler integration method are tested to check its performed in the simulation to check if each method produces distinct results. Since the integration step and the linear velocity of the robot arm during the simulation are small, no distinct results are observed.

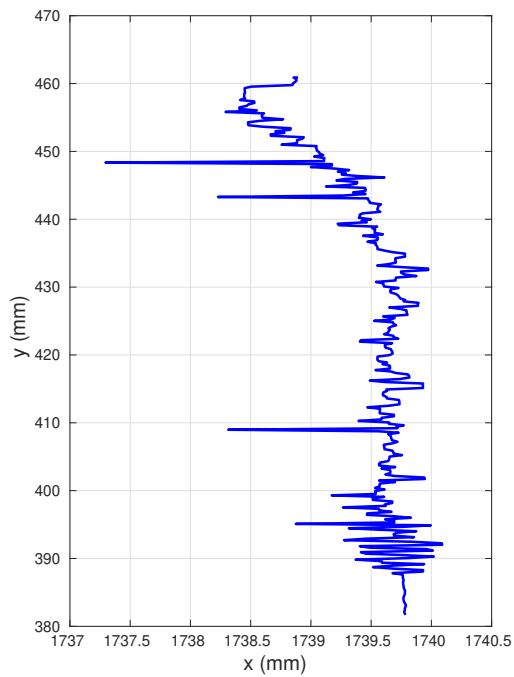
The estimated, the predicted, and the measured bead placement for both Euler



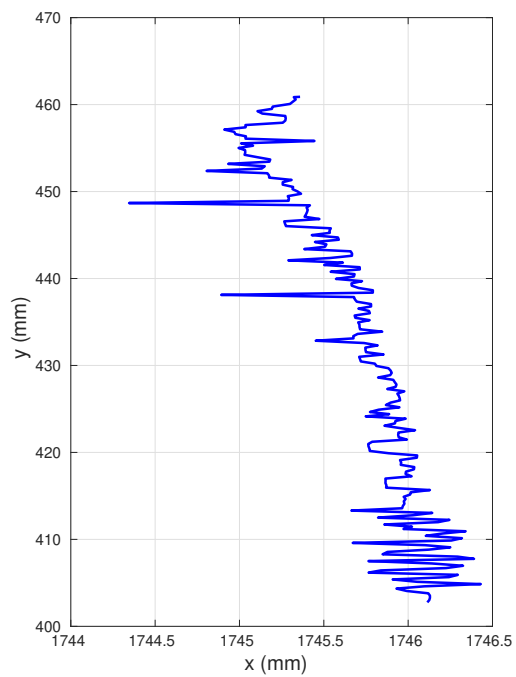
(a) 1st bead.



(b) 2nd bead.



(c) 3rd bead.



(d) 4th bead.

Figure 7.22: Individual beads centerline placement estimation for the linear .

and Runge-Kutta integration methods are presented at Figure 7.28. There is no variance difference when compared the Euler and Runge-Kutta integration method for the bead centerline estimated state. The estimation comparison with the real

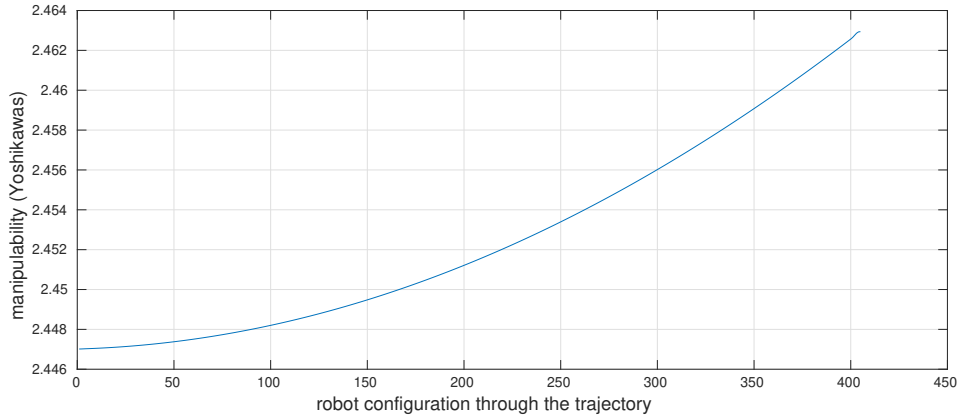


Figure 7.23: Manipulability computed for the linear trajectory.

bead placement is described at Figure 7.29.

7.4.2 Circular trajectory deposition

In the circular trajectory the robot arm manipulability is computed again to ensure there is no singularities along the performed trajectory, which is shown at Figure 7.24.

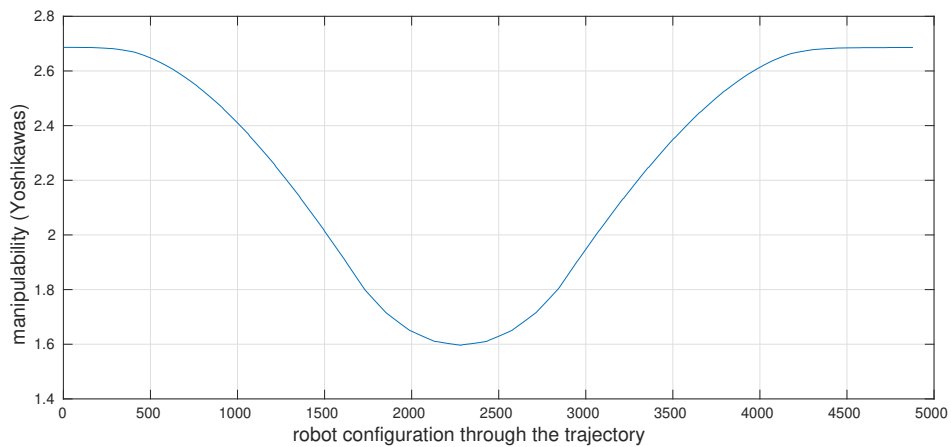


Figure 7.24: Manipulability computed for the circular trajectory.

wire orientation: varying

The planned and performed bead placement is shown in Figure 7.31, it is also possible to identify the influence of the deviation in the wire feed angle along the deposition path especially at the end of the trajectory, as shown at Figure 7.30. Where the orthogonal deviation from the path planned caused by the wire feed angle is shown at Figure 7.32. Both Runge-Kutta and Euler integration methods are tested to check if the integration method impact the simulation result in this

type of trajectory. The result from both integration methods are equivalent as shown in Figure 7.28, which is expected since the robot linear velocity and the integration step are small, then for the other results presented the integration method used is the Runge-Kutta.

The estimated, the predicted, and the measured bead placement for both Euler and Runge-Kutta integration methods are presented at Figure 7.33. No estimated variance is noticed when compared the Euler and Runge-Kutta integration method for the bead centerline state, therefore. The estimation comparison with the real bead placement is described at Figure 7.34.

7.4.3 Simulation discussion

It is possible to perceive that in both simulated scenarios, linear and circular trajectories, and respecting the assumptions made, that the bead centerline deposition along the trajectory deviates from the desired path due to the wire deflection. The noisy data acquired from camera 1 and camera 2 add more uncertainty to the measurement, therefore the proposed estimation plays an important role in improving the quality of the state estimate. An example of a noisy bead placement measurement were presented at section 7.3 which also reinforce the importance of improving the quality of the estimation performed.

Since both prediction and measurement are noisy data, the estimation also differs from the real state. However, as a direct advantage of using the EKF, the state estimate presented a lower variance when compared with the predicted state from the pure pursuit (camera 2) and the measured state acquired from camera 1. A real deposition experiment to test the performance and possible improvements in the current proposal is necessary, this step is detailed in the future work section.

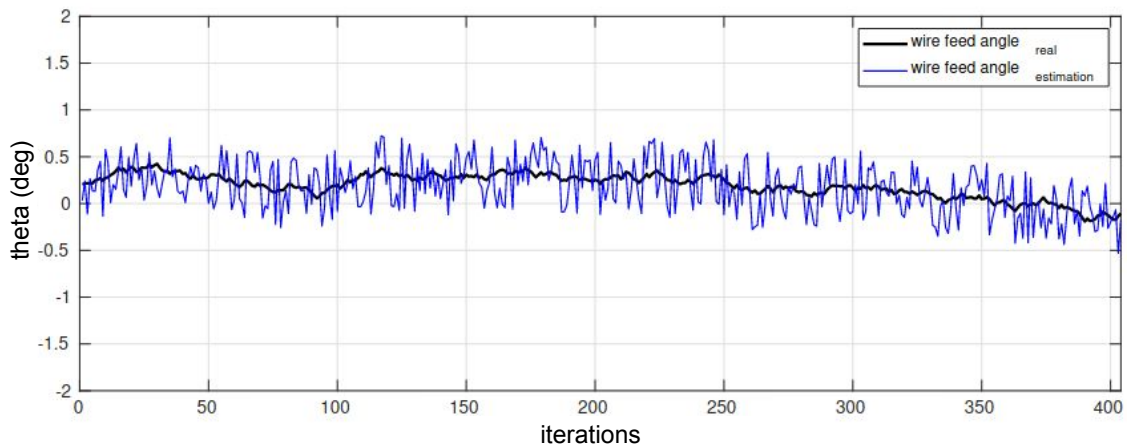


Figure 7.25: Real and estimated wire feeding angle along the linear deposition trajectory for a varying wire feeding angle.

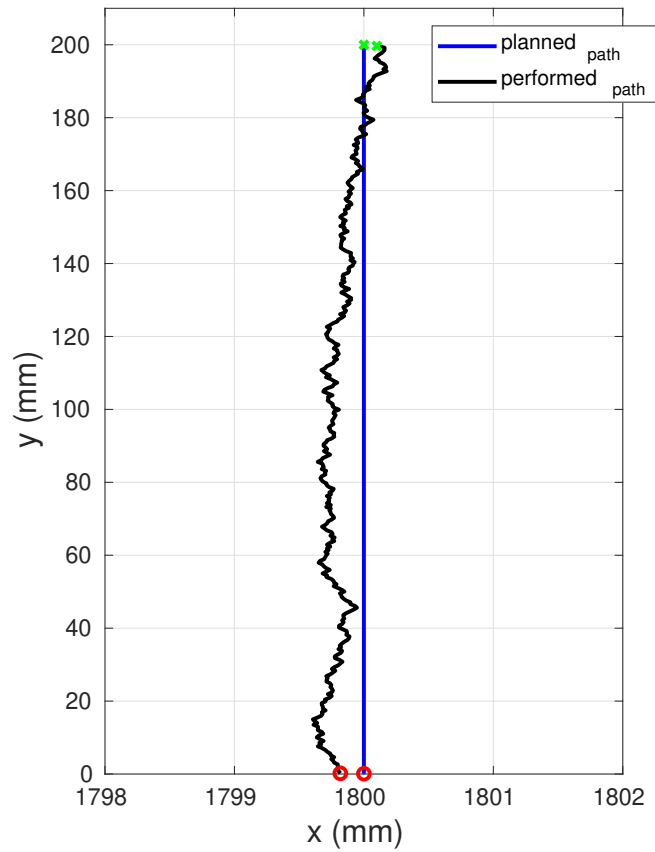


Figure 7.26: Bead planned and performed path for a varying wire feed angle. The red circle represents the trajectory start and the green x represents the trajectory end.

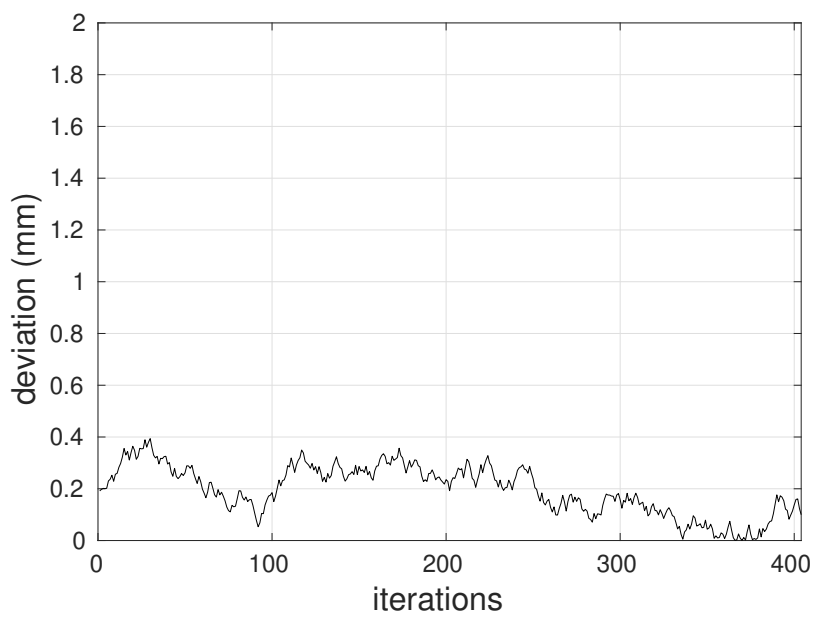
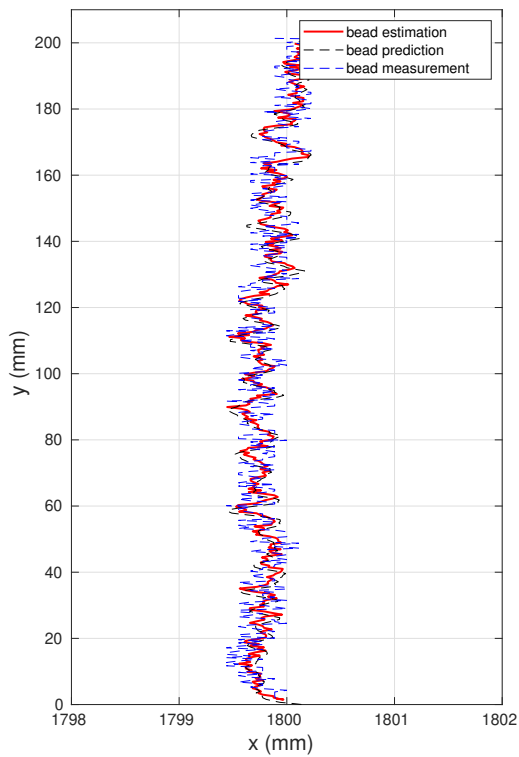
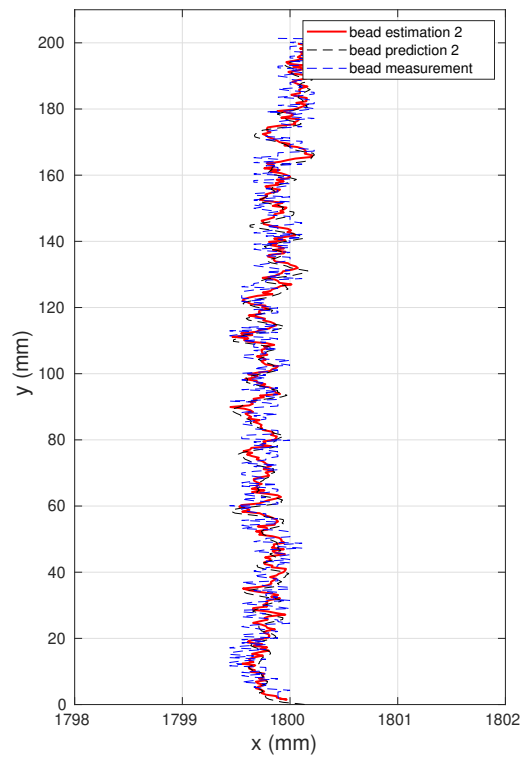


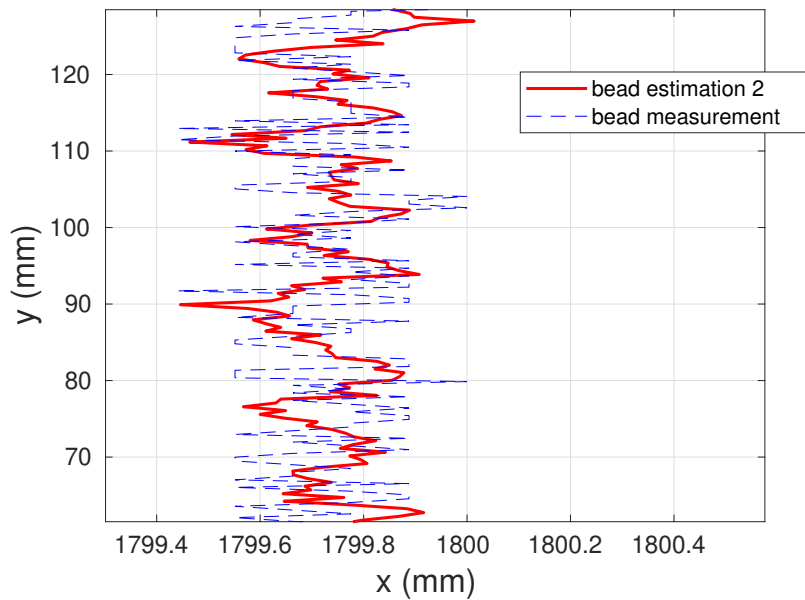
Figure 7.27: Bead deviation along the linear trajectory for a varying wire feed angle.



(a) Euler integration.

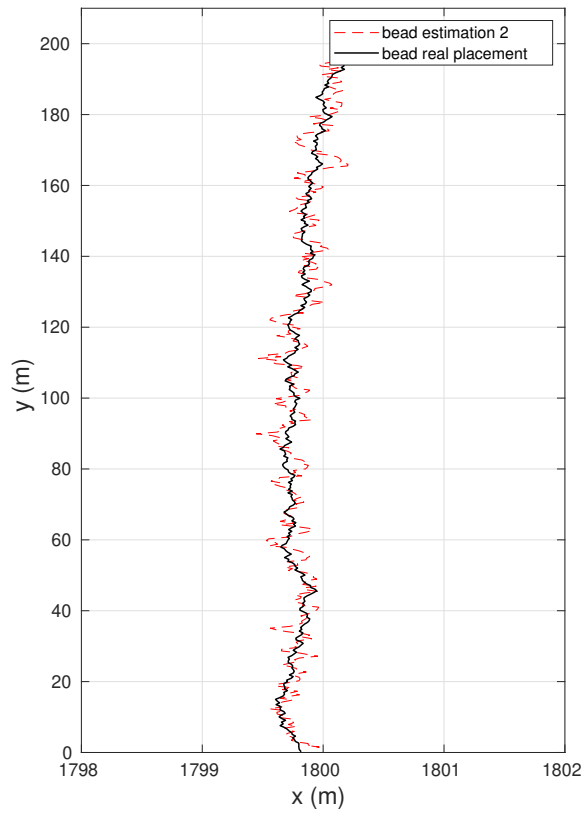


(b) Runge-Kutta integration.

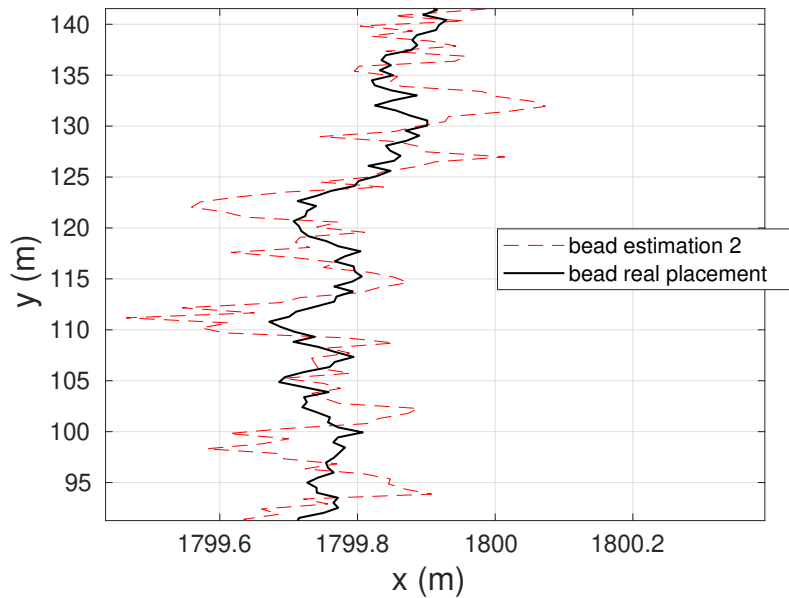


(c) Runge-Kutta estimation result zoomed.

Figure 7.28: Estimated, predicted and measured bead centerline localization along the trajectory for a varying wire feed angle.

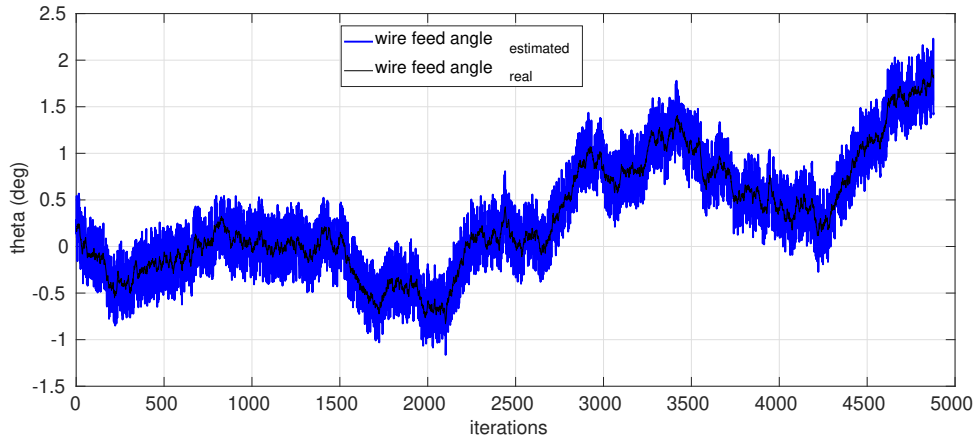


(a) Linear trajectory (estimation x real).

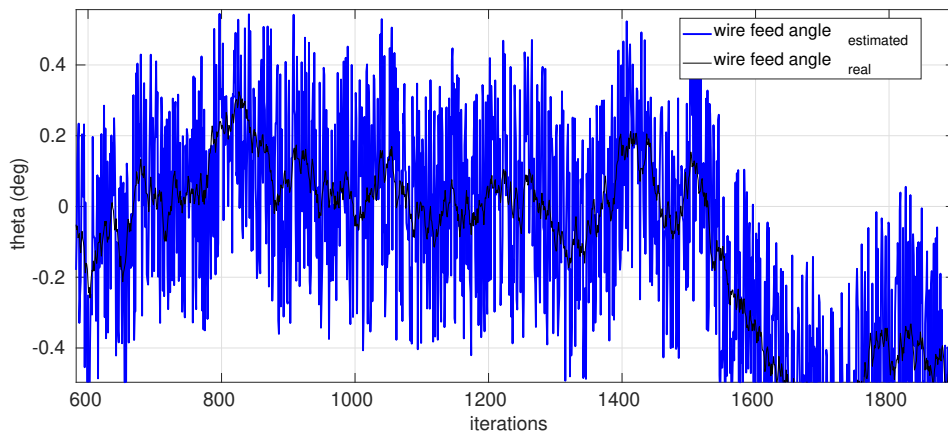


(b) Linear trajectory (estimation x real) zoomed.

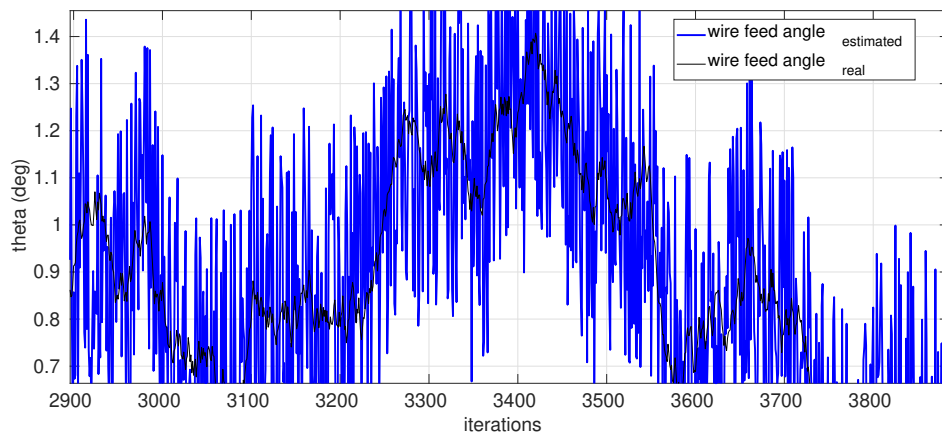
Figure 7.29: Estimated and real centerline localization of the bead along the trajectory for a varying wire feed angle.



(a)

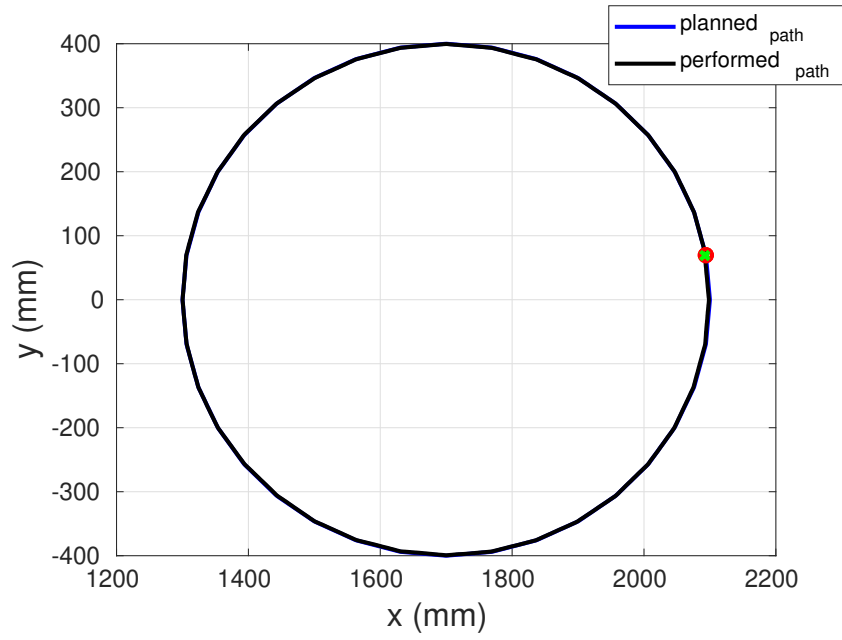


(b)

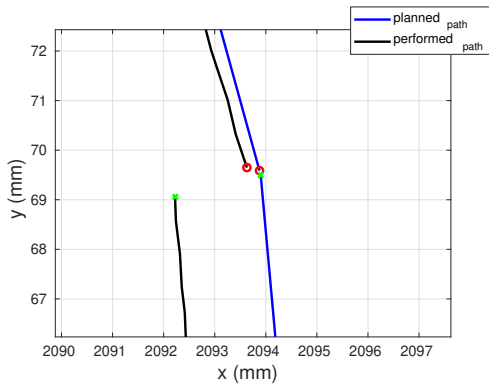


(c)

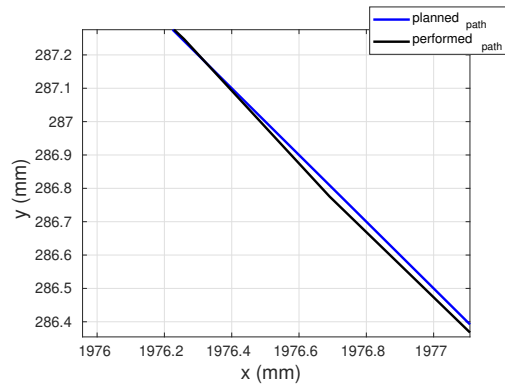
Figure 7.30: Real and estimated wire feeding angle along the deposition (a) for a varying wire angle and a circular trajectory. (b) and (c) are zoomed areas of the original angle estimation chart.



(a) Planned and performed trajectory



(b) The trajectory start and end zoomed.



(c) A trajectory segment zoomed.

Figure 7.31: Bead planned and performed path for a varying wire feed angle and a circular trajectory. The red circle represents the trajectory start and the green x represents the trajectory end.

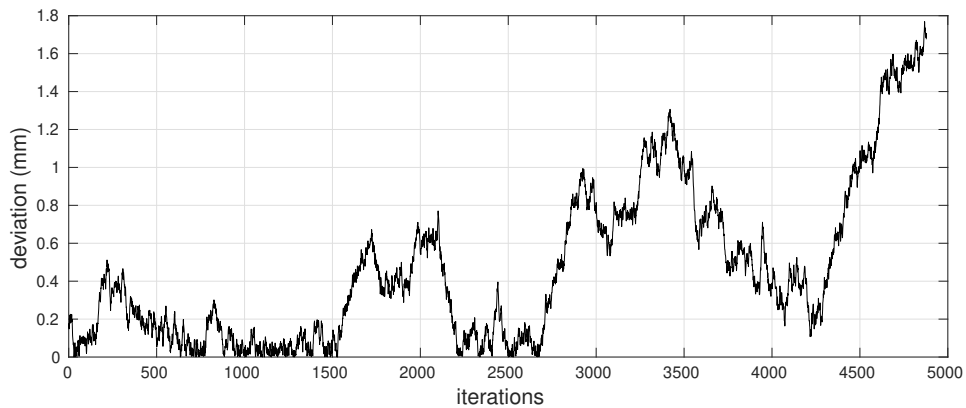
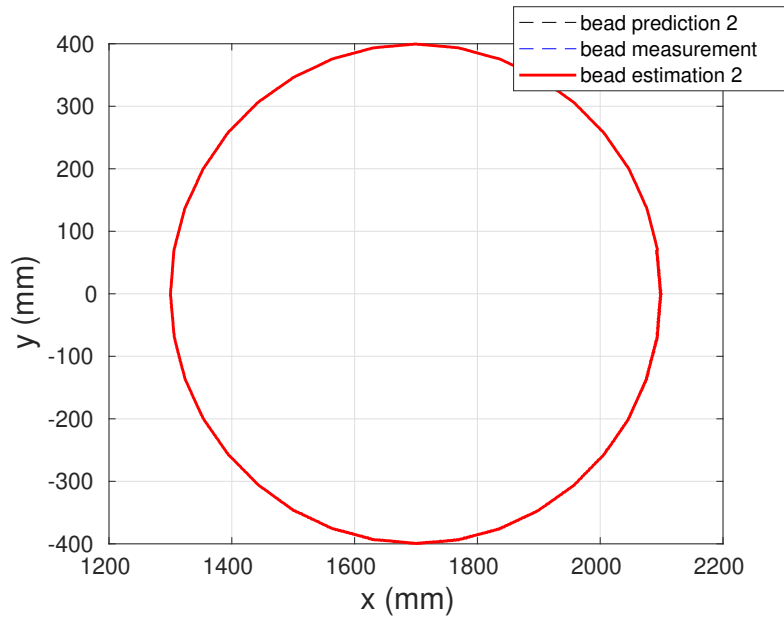
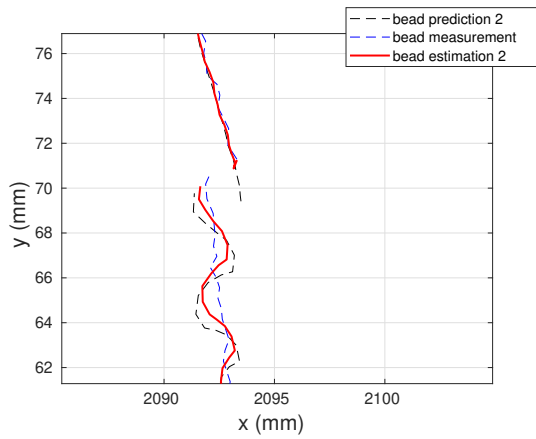


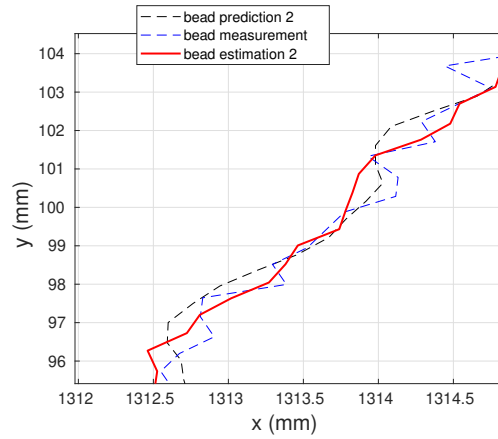
Figure 7.32: Bead deviation along the trajectory for a varying wire feed angle, and a circular trajectory.



(a) Bead placement (predicted x measured x estimated).

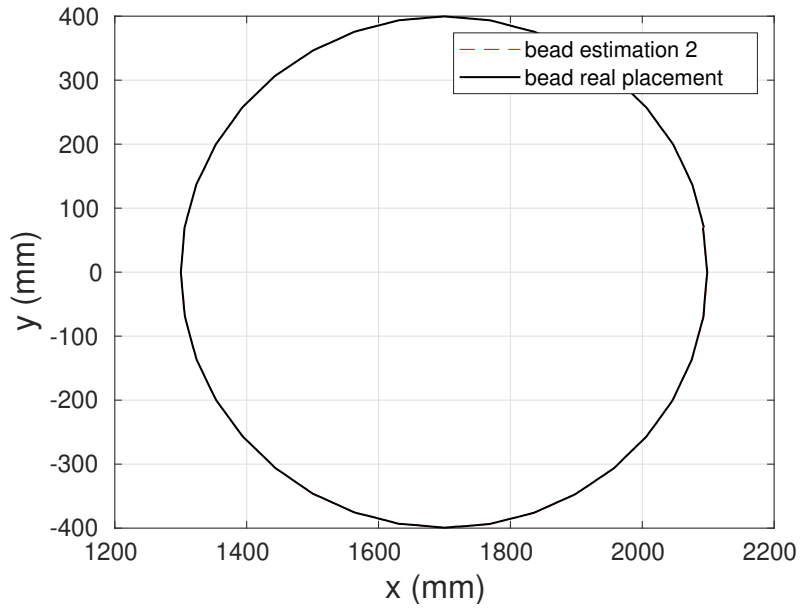


(b) The trajectory start and end zoomed.

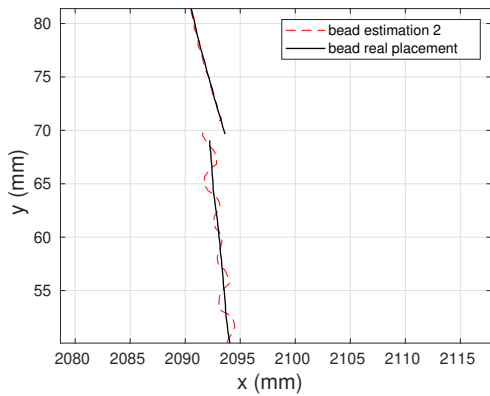


(c) A trajectory segment zoomed.

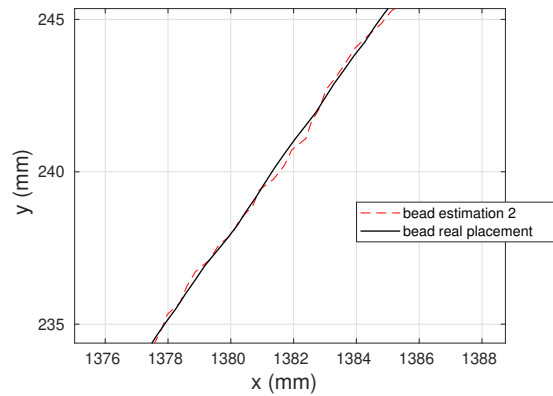
Figure 7.33: Estimated, predicted and measured bead centerline localization along the trajectory for a varying wire feed angle, and a circular trajectory.



(a) Bead placement (estimated x real).



(b) The trajectory start and end zoomed.



(c) A trajectory segment zoomed.

Figure 7.34: Estimated and real centerline localization of the bead along the trajectory for a varying wire feed angle, and a circular trajectory.

Chapter 8

Conclusion

This work addresses the online extraction of the bead geometry's characteristics (width and centerline) of deposited beads with monocular cameras. The implemented vision-based algorithm proved to be a reliable option for developing and implementing of a monitoring system for WAAM, making possible corrections during the printing.

The width monitoring is performed satisfactorily even under a noisy process. However to achieve this result it is necessary to filter the features, the measurement, and also use previous states of the process to allow the outlier rejection. The measurement performed by the algorithm for scenarios with constant and varying bead width is also satisfactorily achieved, as it perceives and measures the width variations as proposed. In the case of a layer (multi-bead), it is also possible to measure the desired characteristics of the beads, despite the slight variations expected from the beads deposited after the first one (single-bead).

For the multi-bead proposition, the bead width estimation results obtained in the third experiment with the HDR camera shown similar results when compared with the ones presented at the second experiment. Where after the first bead (single-bead) the width estimated tends to decrease and the width estimation also present a lower variance after the second deposited bead width. The Infra-red camera width estimation recording is performed under the stable part of the chart, where it present a lower variance from each bead when compared to the HDR camera. However, the IR camera present a high noise at the beginning and end of the deposition due to some characteristics of the equipment (e.g. image ghost). Another aspect observed is the similar accuracy from NIT and Xiris in the third experiment, since NIT pixel size is bigger than Xiris HDR camera a lower accuracy in the estimation was expected.

The placement estimation performed presented high variance, however the result obtained are relevant for the bead placement estimation. The development of an alternative filtering solution shows necessary which could improved the accuracy of the measurement while monitoring the bead placement in real-time.

8.1 Passive vision monitoring system

The monitor system is developed with ROS framework as a set of nodes with specific functions, these are coded using python and opencv library. It is possible to conclude that, as showed in the present work, monocular passive cameras are capable of extracting important information of the process. With a proper computer vision algorithm, the real-time estimation of the bead geometry characteristics are achieved constantly for varying scenarios and distinct deposition parameters.

The width monitoring is performed successfully, even under a noisy process. In particular the short circuit characteristic generates a lot of problems for the image acquired, saturating and also decreases the light intensity rate between pixels, which presented to be a problematic characteristic for the edge detection and segmentation algorithms. However, with the use of the Buffer filter and an adaptive parameter threshold for the segmentation it was possible to monitor and record the necessary state to perform properly the outlier rejection and feature comparison for a set of selected frames.

8.2 Simulated bead placement estimation

The bead centerline placement proposal using the EFK with two simulated camera shown an improvement in the bead placement estimation, where the estimated state presented a lower variance when compared to the predicted and measured states. A 5cm wire stick-out is considered to simulate the orthogonal deviation from the path planned along the deposition, which would impact in the quality of the part being produced. Therefore, the bead centerline estimated shows to be an improvement, because as presented in the section 7.4 of the current work, the bead centerline placement is noisy and the information should be reliable and have a low variance to enable a feedback control. Where it must be achieved to to keep the wire-tip and the bead above the trajectory performed.

8.3 Future work

In this section it is specified a proposal for future works based on the developments, criticality, the and results presented at the current work.

(i) Improve the quality of the bead centerline estimation through the development of an alternative filtering solution to attenuate the noise observed during the monitoring. And also consider neural network system to improve the estimation and reliability.

(ii) Perform a deposition in a WAAM system with independent wire feeding

system using two cameras as proposed in section 6.4 of the current work, then test the performance of the algorithm developed and make the possible improvements to achieve a better accuracy for the real-time bead centerline placement estimation. It is important to highlight that the algorithm to monitor and extract the wire deviation must be developed and tested previously.

(iii) Develop a sensor fusion algorithm based on Kalman filter with two passive cameras at the same configuration capturing the same deposition characteristics. Since the amount of noise in the process is high and varies for every print process, it is relevant to improve the accuracy of the estimated state. Which also improve the chance of success of a feedback control algorithm to be developed.

(iv) The bead placement estimation developed opens the possibility to attenuate the deviations caused by a wire of low quality. Reducing the necessity of developing and qualify wire suppliers specifically for this application, which will also increase the scalability of the technology enabling its usage with lesser restrictions around the world.

The usage of a feed back control with the bead centerline and wire angle estimation. It would be possible to guarantee lesser material being deposited outside the desired path by the control of the robot arms pose automatically during the print, which will result in lower dependence of the wire quality and improve the build quality.

An simple schematic of the proposal is presented at Figure 8.1, which used the robot arm higher DOF when compared to the DOF that the task required to control the wire tip position above the path despite its lateral deviations.

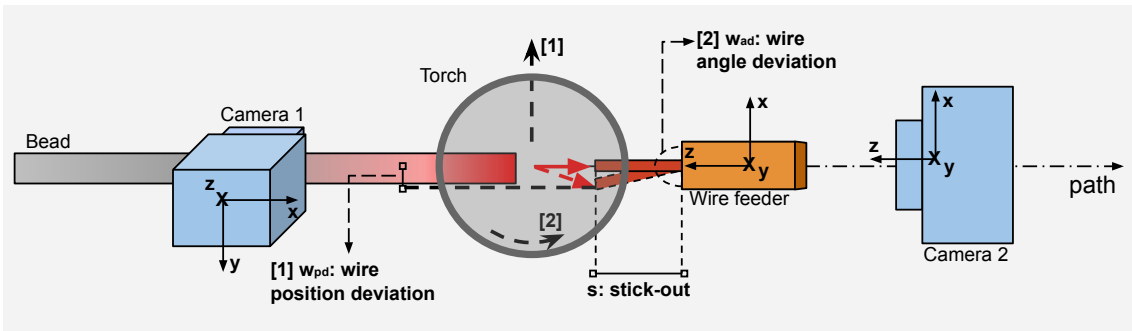


Figure 8.1: Topside view of the system with the deviation caused by a low quality wire.

Since the camera 1 estimate the position of the bead centerline in real time, and camera 2 estimate the angle deviation of the wire being fed. Therefore, two control options arises, and is exemplified [1] and [2] characteristic and actions at Figure 8.1 with a zoomed view at Figure 8.1, about the control proposals: (i) The wire lateral deviation from path are corrected through the movement of the end-effector on the

opposite direction; (ii) The wire feeding angle deviation is corrected rotating the last end-effector joint without changing the electric arc position through the path.

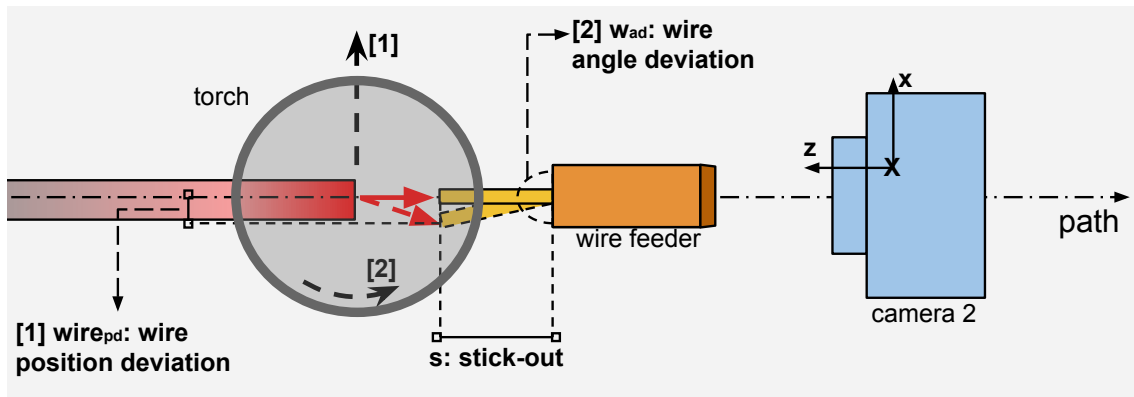


Figure 8.2: Topside view zoomed of the control proposal for the bead placement and wire feeding while printing.

Also a deposition experiment with the same objective must be performed to prove the reliability of the algorithm when applied in a real life application.

References

- [1] AIYITI, W., ZHAO, W., LU, B., et al., 2006, “Investigation of the Overlapping Parameters of MPAW-Based Rapid Prototyping”, *Rapid Prototyping Journal*, v. 12, n. 3, pp. 165–172.
- [2] BANDARI, Y. K., CHARRETT, T. O., MICHEL, F., et al., 2016, “Compensation Strategies for Robotic Motion Errors for Additive Manufacturing (AM)”. In: *Proceedings of 27th Annual International Solid Freeform Fabrication Symposium*, n. August, pp. 8–10. International Solid Freeform Fabrication Symposium.
- [3] BERTOLDI, M., YARDIMCI, M. A., PISTOR, C. M., et al., 1998, “Domain Decomposition and Space Filling Curves in Toolpath Planning and Generation”, *Proceeding of the 1998 Solid Fabrication Symposium*, pp. 267–274.
- [4] CANNY, J., 1986, “A Computational Approach to Edge Detection”, *IEEE Transactions on Pattern Analysis and Machine Intelligence*, v. PAMI-8, n. 6, pp. 679–698.
- [5] CAO, Y., ZHU, S., LIANG, X., et al., 2011, “Overlapping Model of Beads and Curve Fitting of Bead Section for Rapid Manufacturing by Robotic MAG Welding Process”, *Robotics and Computer-Integrated Manufacturing*, v. 27, n. 3, pp. 641–645.
- [6] CHAN, B., PACEY, J., BIBBY, M., 1999, “Modelling Gas Metal Arc Weld Geometry Using Artificial Neural Network Technology”, *Canadian Metallurgical Quarterly*, v. 38, n. 1, pp. 43–51.
- [7] CHARLES, P., 2012, *Digital Video and HD*. Elsevier.
- [8] CHEN, B., WANG, J., CHEN, S., 2010, “A study on application of multi-sensor information fusion in pulsed GTAW”, *Industrial Robot: An International Journal*, v. 37, n. 2 (mar), pp. 168–176.

- [9] CHEN, S., WU, J., 2009, *Intelligentized Methodology for Arc Welding Dynamical Processes*, v. 29, *Lecture Notes in Electrical Engineering*. Springer.
- [10] CHEN, S., QIU, T., LIN, T., et al., 2004, “Intelligent Technologies for Robotic Welding”. In: *Robotic Welding, Intelligence and Automation*, Springer, pp. 123–143, may.
- [11] CHEN, S., ZHAO, D., LOU, Y., et al., 2004, “Computer Vision Sensing and Intelligent Control of Welding Pool Dynamics”. In: *Robotic Welding, Intelligence and Automation*, Springer, pp. 25–55, Berlin, Heidelberg, may.
- [12] CHEN, X. Z., CHEN, S. B., LIN, T., 2007, “Recognition of Macroscopic Seam for Complex Robotic Welding Environment”. In: *Robotic Welding, Intelligence and Automation*, v. 362, Springer, pp. 171–178.
- [13] CHU, H.-H., WANG, Z.-Y., 2016, “A Vision-Based System for Post-Welding Quality Measurement and Defect Detection”, *The International Journal of Advanced Manufacturing Technology*, v. 86, n. 9-12 (oct), pp. 3007–3014.
- [14] COLEGROVE, P. A., COULES, H. E., FAIRMAN, J., et al., 2013, “Microstructure and residual stress improvement in wire and arc additively manufactured parts through high-pressure rolling”, *Journal of Materials Processing Technology*, v. 213, n. 10 (oct), pp. 1782–1791.
- [15] COOK, G., BARNETT, R., ANDERSEN, K., et al., 1995, “Automated Visual Inspection and Interpretation System for Weld Quality Evaluation”. In: *IAS '95. Conference Record of the 1995 IEEE Industry Applications Conference Thirtieth IAS Annual Meeting*, v. 2, pp. 1809–1816. IEEE.
- [16] CORKE, P., 2017, *Robotics, Vision and Control*, v. 118, *Springer Tracts in Advanced Robotics*. Cham, Springer International Publishing.
- [17] COUTO, M. O., RODRIGUES, A. G., COUTINHO, F., et al., 2022, “Mapping of Bead Geometry in Wire Arc Additive Manufacturing Systems Using Passive Vision”, *Journal of Control, Automation and Electrical Systems*.
- [18] COUTO, M. V. D. O., COSTA, R. R., PAYÃO FILHO, J. D. C., et al., 2020, “Weld Bead Width Monitoring in a Carbon Steel Wire and Arc Additive Manufacturing System”, *Rio Oil and Gas Expo and Conference*, v. 20, pp. 418–419.
- [19] CRUZ, J. G., TORRES, E. M., ABSI ALFARO, S. C., 2015, “A Methodology for Modeling and Control of Weld Bead Width in the GMAW Process”,

Journal of the Brazilian Society of Mechanical Sciences and Engineering, v. 37, pp. 1529–1541.

- [20] DANIELSEN EVJEMO, L., MOE, S., GRAVD AHL, J. T., et al., 2017, “Additive Manufacturing by Robot Manipulator: An Overview of the State-of-the-Art and Proof-of-Concept Results”. In: *2017 22nd IEEE International Conference on Emerging Technologies and Factory Automation (ETFA)*, pp. 1–8. IEEE, sep.
- [21] DING, D., PAN, Z., CUIURI, D., et al., 2014. “A Tool-Path Generation Strategy for Wire and Arc Additive Manufacturing”. .
- [22] DING, D., PAN, Z., CUIURI, D., et al., 2014. “A Multi-Bead Overlapping Model for Robotic Wire and Arc Additive Manufacturing (WAAM)”. .
- [23] DING, D., PAN, Z., CUIURI, D., et al., 2015, “A Practical Path Planning Methodology for Wire and Arc Additive Manufacturing of Thin-Walled Structures”, *Robotics and Computer-Integrated Manufacturing*, v. 34 (aug), pp. 8–19.
- [24] DING, D., PAN, Z., CUIURI, D., et al., 2015. “Wire-feed additive manufacturing of metal components: technologies, developments and future interests”. .
- [25] DING, D., PAN, Z., CUIURI, D., et al., 2015, “Wire-Feed Additive Manufacturing of Metal Components: Technologies, Developments and Future Interests”, *The International Journal of Advanced Manufacturing Technology*, v. 81, n. 1-4 (oct), pp. 465–481.
- [26] DING, D., PAN, Z., CUIURI, D., et al., 2016, “Adaptive Path Planning for Wire-Feed Additive Manufacturing Using Medial Axis Transformation”, *Journal of Cleaner Production*, v. 133 (oct), pp. 942–952.
- [27] DING, D., PAN, Z., CUIURI, D., et al., 2016, “Bead Modelling and Implementation of Adaptive MAT Path in Wire and Arc Additive Manufacturing”, *Robotics and Computer-Integrated Manufacturing*, v. 39, pp. 32–42.
- [28] DING, J., COLEGROVE, P., MEHNEN, J., et al., 2011, “Thermo-Mechanical Analysis of Wire and Arc Additive Layer Manufacturing Process on Large Multi-Layer Parts”, *Computational Materials Science*, v. 50, n. 12, pp. 3315–3322.

- [29] DOUMANIDIS, C., KWAK, Y.-M., 2002, “Multivariable adaptive control of the bead profile geometry in gas metal arc welding with thermal scanning”, *International Journal of Pressure Vessels and Piping*, v. 79, n. 4 (apr), pp. 251–262.
- [30] DUNLAVEY, M. R., 1983, “Efficient Polygon-Filling Algorithms for Raster Displays”, *ACM Transactions on Graphics (TOG)*, v. 2, n. 4, pp. 264–273.
- [31] DWIVEDI, R., KOVACEVIC, R., 2004, “Automated Torch Path Planning Using Polygon Subdivision for Solid Freeform Fabrication Based on Welding”, *Journal of Manufacturing Systems*, v. 23, n. 4, pp. 278–291.
- [32] FAROUKI, R. T., KOENIG, T., TARABANIS, K. A., et al., 1995. “Path Planning With Offset Curves for Layered Fabrication Processes”. .
- [33] FONT COMAS, T., DIAO, C., DING, J., et al., 2017, “A Passive Imaging System for Geometry Measurement for the Plasma Arc Welding Process”, *IEEE Transactions on Industrial Electronics*, v. 64, n. 9 (sep), pp. 7201–7209. ISSN: 0278-0046.
- [34] FRAGA, F. F., DE CARVALHO, G. C., DE OLIVEIRA, T. F., 2015, “Heat transfer applied to rapid prototyping by metal deposition in successive layers using 3D welding”, *Welding International*, v. 29, pp. 600–609.
- [35] GARDNER, L., KYVELOU, P., HERBERT, G., et al., 2020, “Testing and Initial Verification of the World’s First Metal 3D Printed Bridge”, *Journal of Constructional Steel Research*, v. 172.
- [36] GE, M., XU, Y., 2004, “A Novel Intelligent Monitor for Manufacturing Processes”. In: *Robotic Welding, Intelligence and Automation*, Springer, pp. 63–79, Berlin, Heidelberg.
- [37] GENG, H., LI, J., XIONG, J., et al., 2017, “Optimization of Wire Feed for GTAW Based Additive Manufacturing”, *Journal of Materials Processing Technology*, v. 243, pp. 40–47.
- [38] GIBSON, I., ROSEN, D. W., STUCKER, B., 2010, *Additive Manufacturing Technologies*. Boston, MA, Springer US.
- [39] GONZALEZ, R. C., WOODS, R. E., 2007, *Digital Image Processing (3rd Edition)*. Pearson.
- [40] HOUGH, P. V. C., 1962, “Methods and means for recognizing complex patterns”, *U.S. Patent 3 069 654*.

- [41] J., W., SB., C., 2007, “Software System Designs of Real-Time Image Processing of Weld Pool Dynamic Characteristics”. In: T.J., T., SB., C., C., Z. (Eds.), *Robotic Welding, Intelligence and Automation*, v. 362, Springer, p. 303–309.
- [42] JIN, G., LI, W., GAO, L., 2013, “An Adaptive Process Planning Approach of Rapid Prototyping and Manufacturing”, *Robotics and Computer-Integrated Manufacturing*, v. 29, n. 1 (feb), pp. 23–38.
- [43] LI, H., DONG, Z., VICKERS, G. W., 1994, “Optimal Toolpath Pattern Identification for Single Island, Sculptured Part Rough Machining Using Fuzzy Pattern Analysis”, *Computer-Aided Design*, v. 26, n. 11, pp. 787–795.
- [44] LUO, X., WANG, Z.-Y., JIA, C.-B., 2015, “A Low-Cost Vision System for Open Arc Welding Based on Multi-exposure”. In: *Lecture Notes in Electrical Engineering*, v. 88 LNEE, Springer, pp. 273–281.
- [45] MA, G. H., WANG, L., LIU, G. Q., et al., 2011, “Research on Image Process and Tracing of a Welding Robot”. In: *Robotic Welding, Intelligence and Automation*, v. 88, Springer, pp. 253–259, .
- [46] MA, G., QIN, J., JIANG, F. R., et al., 2011. “Depth Extraction by Simplified Binocular Vision”. .
- [47] MA, G., QIN, J., JIANG, F. R., et al., 2011, “Depth Extraction by Simplified Binocular Vision”. In: *Lecture Notes in Electrical Engineering*, v. 88 LNEE, Springer, pp. 179–183, .
- [48] NAIDU, D. S., OZCELIK, S., MOORE, K. L., 2003, *Modeling, Sensing and Control of Gas Metal Arc Welding*. Elsevier.
- [49] O. COUTO, M., R. COSTA, R., C. LEITE, A., et al., 2020, “Weld Bead Width Measurement in a GMAW WAAM System by using Passive Vision”. In: *Anais do Congresso Brasileiro de Automática 2020*. sbabra, dec.
- [50] PAN, Z., DING, D., WU, B., et al., 2018, “Arc Welding Processes for Additive Manufacturing: A Review”. In: *Transactions on Intelligent Welding Manufacturing*, n. 2, 1 ed., Springer, Singapore, pp. 3–24.
- [51] PARK, S., CHOI, B., 2000, “Tool-Path Planning for Direction-Parallel Area Milling”, *Computer-Aided Design*, v. 32, n. 1 (jan), pp. 17–25.

- [52] PINTO-LOPERA, J., S. T. MOTTA, J., ABSI ALFARO, S., 2016, “Real-Time Measurement of Width and Height of Weld Beads in GMAW Processes”, *Sensors*, v. 16, n. 9 (sep), pp. 1500. ISSN: 1424-8220.
- [53] RAJAN, V. T., SRINIVASAN, V., TARABANIS, K. A., 2001, “The Optimal Zigzag Direction for Filling a Two-Dimensional Region”, *Rapid Prototyping Journal*, v. 7, n. 5, pp. 231–241.
- [54] REN, F., SUN, Y., GUO, D., 2009, “Combined Reparameterization-Based Spiral Toolpath Generation for Five-Axis Sculptured Surface Machining”, *International Journal of Advanced Manufacturing Technology*, v. 40, n. 7-8, pp. 760–768.
- [55] RIOS, S., COLEGROBE, P. A., MARTINA, F., et al., 2018. “Analytical process model for wire + arc additive manufacturing”. .
- [56] SHI, F., ZHOU, L., LIN, T., et al., 2007, “Efficient Weld Seam Detection for Robotic Welding from a Single Image”. In: *Robotic Welding, Intelligence and Automation*, v. 362, Springer, pp. 289–294.
- [57] SICILIANO, B., SCIAVICCO, L., VILLANI, L., et al., 2009, *Robotics*. London, England, Springer.
- [58] SRINIVAS, M., BABU, B. S., 2017, “A Critical Review on Recent Research Methodologies in Additive Manufacturing”, *Materials Today: Proceedings*, v. 4, n. 8, pp. 9049–9059.
- [59] SURYAKUMAR, S., KARUNAKARAN, K. P., BERNARD, A., et al., 2011. “Weld Bead Modeling and Process Optimization in Hybrid Layered Manufacturing”. .
- [60] THRUN, S., BURGARD, W., DIETER, F., 2005, *Probabilistic Robotics*. Lodon, England, MIT Press.
- [61] WANG, H., JANG, P., STORI, J. A., 2005, “A Metric-Based Approach to Two-Dimensional (2D) Tool-Path Optimization for High-Speed Machining”, *Journal of Manufacturing Science and Engineering, Transactions of the ASME*, v. 127, n. 1, pp. 33–48.
- [62] WANG, J. F., ZHOU, L., CHEN, S. B., 2007, “Measurement for Three Dimensional Surface of Welding Pool in GTAW Welding”. In: *Robotic Welding, Intelligence and Automation*, v. 362, Springer, pp. 219–225.

- [63] WASSER, T., JAYAL, A. D., PISTOR, C., 1999, “Implementation and Evaluation of Novel Build Styles in Fused Deposition Modeling (FDM)”, *Solid Freeform Fabrication Proceedings, August 1999*, pp. 95–102.
- [64] WILLIAMS, S. W., MARTINA, F., ADDISON, A. C., et al., 2016, “Wire + Arc Additive Manufacturing”, *Materials Science and Technology*, v. 32, n. 7 (may), pp. 641–647.
- [65] WU, B., PAN, Z., DING, D., et al., 2018, “A Review of the Wire Arc Additive Manufacturing of Metals: Properties, Defects and Quality Improvement”, *Journal of Manufacturing Processes*, v. 35 (oct), pp. 127–139.
- [66] WU, J., CHEN, S. B., 2007, “Software System Designs of Real-Time Image Processing of Weld Pool Dynamic Characteristics”. In: *Robotic Welding, Intelligence and Automation*, v. 362, Springer, pp. 303–309.
- [67] WU, Q., LU, J., LIU, C., et al., 2017, “Obtaining Uniform Deposition With Variable Wire Feeding Direction During Wire-Feed Additive Manufacturing”, *Materials and Manufacturing Processes*, v. 32, n. 16, pp. 1881–1886.
- [68] XIONG, J., ZHANG, G., GAO, H., et al., 2013, “Modeling of Bead Section Profile and Overlapping Beads With Experimental Validation for Robotic GMAW-Based Rapid Manufacturing”, *Robotics and Computer-Integrated Manufacturing*, v. 29, pp. 417–423.
- [69] XIONG, J., ZHANG, G., QIU, Z., et al., 2013, “Vision-Sensing and Bead Width Control of a Single-Bead Multi-Layer Part: Material and Energy Savings in GMAW-Based Rapid Manufacturing”, *Journal of Cleaner Production*, v. 41 (feb), pp. 82–88.
- [70] XU, Y., FANG, G., CHEN, S., et al., 2014, “Real-time Image Processing for Vision-Based Weld Seam Tracking in Robotic GMAW”, *The International Journal of Advanced Manufacturing Technology*, v. 73, pp. 1413–1425.
- [71] XU, Y., LV, N., FANG, G., et al., 2017, “Welding Seam Tracking in Robotic Gas Metal Arc Welding”, *Journal of Materials Processing Technology*, v. 248, pp. 18–30.
- [72] XUE, L., XU, L., ZOU, Y., 2011. “A Method of Seam Tracking Based on Passive Vision”. .

- [73] YANG, Y., LOH, H. T., FUH, J. Y., et al., 2002, “Equidistant Path Generation for Improving Scanning Efficiency in Layered Manufacturing”, *Rapid Prototyping Journal*, v. 8, n. 1, pp. 30–37.
- [74] YUAN LI, YOU FU LI, QING LIN WANG, et al., 2010, “Measurement and Defect Detection of the Weld Bead Based on Online Vision Inspection”, *IEEE Transactions on Instrumentation and Measurement*, v. 59, pp. 1841–1849.
- [75] Z., X., 2011, “Research on a Trilines Laser Vision Sensor for Seam Tracking in Welding”. In: TJ., T., SB., C., C., Z. (Eds.), *Robotic Welding, Intelligence and Automation*, v. 82, Springer, p. 139–144.
- [76] ZHAN, Q., LIANG, Y., DING, J., et al., 2017, “A Wire Deflection Detection Method Based on Image Processing in Wire + Arc Additive Manufacturing”, *The International Journal of Advanced Manufacturing Technology*, v. 89, n. 1-4 (mar), pp. 755–763.
- [77] ZHANG, Y. M., CHEN, Y., LI, P., et al., 2003. “Weld Deposition-Based Rapid Prototyping: A Preliminary Study”. .
- [78] ZHONG, J., CHEN, H., CHEN, S., 2011, “Research on the Robotic Arc Welding of a Five-Port Connector”. In: *Robotic Welding, Intelligence and Automation*, v. 82, Springer, pp. 115–122.